



UNIVERSITA' DEGLI STUDI DI NAPOLI

"FEDERICO II"

Vito Pagliarulo

Electron Beam Lithography patterning of superconducting and magnetic nanostructures for novel optical and spintronic devices

A dissertation submitted to the

Dipartimento di Scienze Fisiche

In fulfilment of the requirements for the degree of

PHILOSOPHIAE DOCTOR

in

Tecnologie Innovative per Materiali, Sensori ed Imaging

(Novel Technologies for Materials, Sensors and Imaging)

XXIII cycle (2008-2010)

Summary

Introduction; 5

Chapter 1: Nanopatterning review

1.1 Immersion Lithography; 7

1.2 Extreme UltraViolet Lithography; 9

1.3 Nanoimprinting; 13

1.4 Focused Ion Beam; 14

1.5 Electron Beam Lithography; 15

1.5.1 EBL based system; 16

1.5.2 Electron gun; 16

1.5.3 SEM column; 17

1.5.4 Chamber and stage and Vacuum system; 20

1.5.5 Scan techniques in direct writing EBL; 21

1.5.6 Limitations on EBL resolution; 22

1.5.7 Electron-solid interaction and the proximity effect; 23

1.5.8 Computer control; 25

1.5.9 Equipment; 26

1.5.10 Photoresist; 27

1.5.10.1 Poly(methyl methacrylate); 26

1.5.10.2 ZEP520; 28

1.5.11 New frontier; 28

References; 29

Chapter 2: Nanopatterning for advanced physics

2.1 Superconducting nanowires for advanced optical detection; 32

2.1.1 Ultrathin superconducting nano-bridge : the working principle; 32

2.1.2 The Hot-Spot model; 34

2.1.3 Quantum Efficiency and Noise Equivalent Power; 39

2.1.4 The proximity effect; 40

2.1.5 Dissipation and fluctuations in low-dimensional superconductors; 43

2.2 Nanostructures for magnetoresistance based devices; 46

2.2.1 Microscopic exchange interaction; 46

2.2.2 Ferromagnetism in metals; 47

2.2.3 The Landau-Lifshitz-Gilbert equation; 50

2.2.3.1 Exchange energy in the continuum approximation; 51

2.2.3.2 Anisotropy energy; 52

2.2.3.3 External field energy; 53

2.2.3.4 Magnetostatic energy; 53

2.2.4 Micromagnetic equations; 54

2.2.5 Domains and domain walls; 56

2.2.6 Magnetization reversal and hysteresis; 58

2.2.7 Constrained domain walls; 59

- 2.2.8 Ordinary Magnetoresistance; 61
- 2.2.9 Anisotropic MR; 63
- 2.2.10 Giant MR; 66
- 2.2.11 Tunnel MR; 71
- 2.2.12 Colossal MR; 72
- 2.2.13 Domain Wall MR; 73
- References; 76

Chapter 3: Devices fabrication and characterization

- 3.1 Sputter deposition; 81
- 3.2 Pulsed Laser Deposition; 83
- 3.3 X-ray diffractometry; 85
- 3.4 Energy Dispersive Spectroscopy; 86
- 3.5 Atomic Force Microscopy; 87
- 3.6 Vibrating Sample Magnetometer; 88
- 3.7 Characterization: Experimental results; 88
 - 3.7.1 Niobium Nitrate; 88
 - 3.7.2 Nickel Copper Alloy; 89
 - 3.7.3 NbN/NiCu bilayers; 90
 - 3.7.4 Permalloy; 91
- 3.8 Devices micro and nano Fabrication; 91
 - 3.8.1 Standard Photolithography; 91
 - 3.8.2 Lift off technique; 92
 - 3.8.3 Ion Gun; 93
 - 3.8.4 Reactive Ion Etching; 94
- 3.9 Operative procedures; 94
 - 3.9.1 PMMA based lithography; 94
 - 3.9.2 ZEP520 based lithography; 95
- References; 96

Chapter 4: Results and discussions

- 4.1 NiCu/NbN superconducting nanostripes for optical detection; 97
 - 4.1.1 Motivation; 97
 - 4.1.2 Fabrication process; 97
 - 4.1.3 Experimental; 99
 - 4.1.4 Time-resolved photoresponse measurements; 102
- 4.2 Permalloy planar spin-valves; 104
 - 4.2.1 Motivation; 104
 - 4.2.2 Fabrication process; 105
 - 4.2.3 Experimental; 106
 - 4.2.4 MR measurements; 107
 - 4.2.5 Photo-response experiments on magnetic nanowires: preliminary results; 116
- References; 119
- Conclusions/Publications; 121

Acknowledgments

First of all I would like to express my gratitude to my supervisors, Prof. G. Pepe and Dr. E. Esposito; they really supported me with patience and understanding during this experience. I would also like to thank all the members of our research group: Prof. G. Peluso, Dr. L. Parlato, Dr. M. Valentino, Dr. C. Bonavolontà, Dr. N. Marrocco, Dr. A. Capretti and Prof. A. Barone. Thanks also to the labs colleagues, Dr. D. Stornaiuolo and Dr. M. Riaz. In the mean time also other people helped me during my work: Prof. U. Scotti, Dr. G. Ausanio, Dr. M. Lisitskiy, Prof. C. Visone, Dr. D. Davino, Dr. L. Ferrante, Prof. C. De Lisio. I cannot forget the kind hospitality and the collaboration that Prof. Myoren, Dr. Taino and all their students reserved to me during my visit at the Saitama University.

I would also like to thank my wife Monica, my parents and all my family for the support they provided me through my entire studies and last but not least my sons Flavio and Fabrizio, my best experiments!

Introduction

Most of devices and systems used in modern industry are becoming progressively smaller reaching the nanoscale dimension (1–100 nm). Nanofabrication allows to build nanoscale structures, which can be employed as components, devices, or systems, in large quantities at potentially low cost in areas across engineering and science. Bottom-up fabrication strategies involve manipulation or synthetic methods of bio-chemistry in directly assembling subnanoscale building blocks into required nanoscale patterns, for bio-medical, chemical, pharmacological, physical sensors and actuators. More promising is the work in large-scale molecular electronics and computers in which individual atomic or molecular parts work as wires and transistors.

However, performing only one atomic or molecular reaction using non-molecular machines, such as scanning probe microscopes, is quite difficult and impractical for making large quantities of a product. It appears that whether the strategy is the “manipulation”, the chemical synthesis, or more generally the self-assembly, the fabrication must occur in parallel or in arrays to self-form groups of atoms or molecules fast enough to produce useful structures on a macroscopic size. The top-down approach has basically evolved from standard lithographic techniques, where nanoscale structures (mainly for semiconductor chips) are fabricated from a bulk material by gradually removing or subtracting small parts of the material in series. An important difference with respect the bottom-up approach is that now the parts or chips are both patterned and built in place, so that no assembly step is needed. The top-down approach has been proven to be a fundamental tool for the evolution of the information technology, and of microsystem industries. Probably, the most promising strategy for the development of nanofabrication processes in large quantities will be a hybrid approach: a combination of both, i.e. bottom-up and conventional top-down, techniques, followed by an integration of biological and chemical nanoelements in future devices.

During this thesis a top-down approach has been employed to fabricate nanodevices for superconducting and magnetic advanced sensors. In order to obtain high resolution and flexibility in prototypes realization of nanostructured devices, the Electron Beam Lithography (EBL) has been used. An important advantage of EBL is that it doesn't need physical masks, and hence it use eliminates costs and time delays associated with mask production. Patterns can be optimized and changed very simply using flexible CAD software. On the lengths scales achieved in nanodevices Immersion and Extreme UltraViolet Lithography could be employed but in order to have high throughput the costs should be very high. Nanoimprinting is a low cost technique characterized by a good spatial resolution but it requires different techniques for realizing masks (and sometimes the EBL is needed to this aim!). Focused Ion Beam offers good resolution and high versatility but it presents some limitations when the patterned area is large.

As applications of EBL nanotechniques in this thesis the attention has been devoted to (i) the investigation of the possibility of engineering materials (superconducting and ferromagnetic) by means of the proximity effect in order to have larger photoresponse and faster dynamics, and (ii) fabricate magnetic nanowires using permalloy (i.e. $\text{Ni}_{80}\text{Fe}_{20}$) for studying the magnetoresistance due to the presence of domain walls and their behaviour in the presence of

an external optical perturbation. To what concerns the first type of application, the development of advanced detectors represents one of more explored fields by the scientific community in the last years. The search for novel and high performances optical detectors, based mainly on the use of NbN ($T_c=15K$) achieved a great interest due to particular characteristics in terms of response time and very thin film superconducting technology. Accordingly, the role of nanowire geometry (i.e. meander shape with several series/parallel configurations) is quite crucial for optimizing detector performances at low temperatures. To what concerns spintronics applications, the fabrication step is an important issue toward the realization of advanced devices to be used for magnetic field sensing, digital non-volatile magnetic data storage, and other applications sometimes involving fundamental physics, which are based on the Domain Wall resistance.

The outline of the thesis is the following:

In Chapter 1 we introduce a review of the most diffuse top-down technique. The basic principles of Electron Beam Lithography are discussed, as well as advantages and limitations of this technique.

In Chapter 2 some theoretical descriptions about the photoresponse mechanisms occurring in a superconducting material and the micromagnetism are briefly presented together with the working principle of a superconducting nanowire detectors and magnetoresistive effect with more attention on the role of Domain Walls (DWs).

In Chapter 3 the fabrication processes/technologies used, as well as the and the characterization methods of the films and multilayers in terms of structural, electrical and magnetic properties, are discussed.

In Chapter 4 the experimental results for both SSPD and DWs based devices are shown and discussed.

Chapter 1: Nanopatterning review

1.1 Immersion Lithography

Immersion lithography is a technique to enhance the standard photolithographic resolution replacing the usual air gap between the final lens and the wafer surface with a liquid medium that has a refractive index (n) greater than one. The increasing of resolution is by a factor equal to the refractive index of the liquid (Fig. 1.1). Immersion lithography tools use highly purified water as liquid, achieving feature sizes below 45 nm [1].

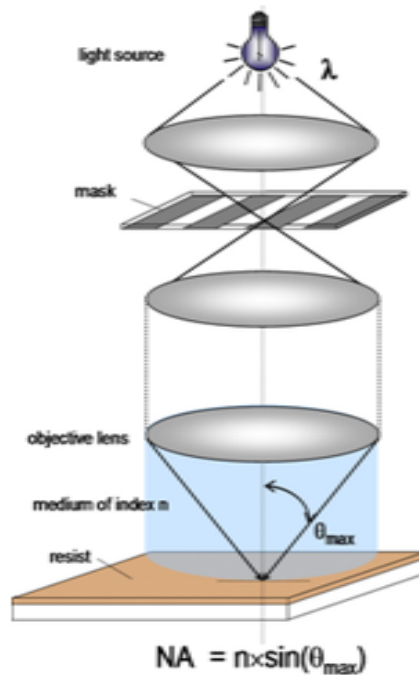


Fig. 1.1 Immersion lithography: light travels down through a system of lenses and a pool of water before reaching the photoresist on top of samples.

The lenses in the highest resolution standard photolithography scanners bend light rays through a range of angles spanning nearly 90 degrees (the numerical aperture NA is the sine of this angle). The only way to improve the resolution is by inserting an immersion medium between the lens and the wafer and it is impossible to increase resolution by further bending. The physical limit to NA for exposure systems using air as a medium between the lens and the wafer is determined by the Rayleigh equation:

$$W = \frac{k_1 \lambda}{NA} \quad (1.1)$$

where, k_1 is the resolution factor, λ is the wavelength of the exposing radiation. NA is actually determined by the acceptance angle of the lens and the index of refraction of the medium surrounding the lens and is given by:

$$NA = n \sin \alpha = \frac{d}{2f} \quad (1.2)$$

where, n is the index of refraction of the medium surrounding the lens and α is the acceptance angle of the lens (see Fig. 1.2):

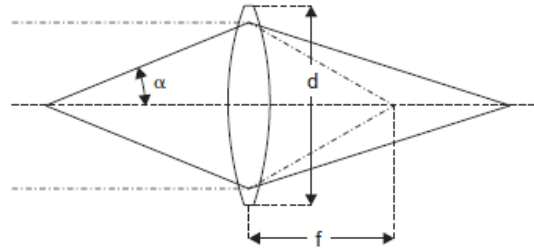


Fig. 1.2 Numerical Aperture.

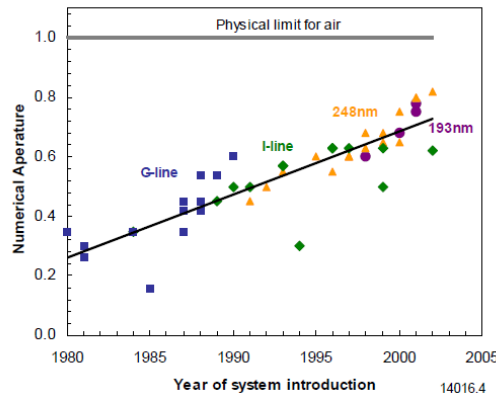


Fig. 1.3 NA trend.

The medium between the lens and the wafer being exposed needs to have an index of refraction >1 , have low optical absorption at 193 nm, be compatible with photoresist and the lens material, be uniform and non-contaminating: ultrapure water may meet all of these requirements. Water has an index of refraction $n \cong 1.47$ [2], absorption of $<5\%$ at working distances of up to 6 mm [3], is compatible with photoresist and lens and in it is ultrapure form is non-contaminating. There have been observations of significant variations in absorption between ultrapure water samples [4], but this is probably due to contaminants or dissolved gases. Replacing $n = 1.47$ into equation and that assuming $\sin \alpha$ can reach 0.93, then the resolution limit for 193nm immersion lithography is:

$$W = \frac{k_1 \lambda}{n \sin \alpha} = 35 \text{ nm} \quad (1.3)$$

The blurriness is reduced by a factor equal to the refractive index of the medium. For water immersion, using ultraviolet light at 193 nm wavelength, the index is 1.44. The resolution enhancement from immersion lithography is $\cong 30\%$ and depend also on materials used. The depth of focus, or tolerance in sample roughness, is up to double better than a corresponding "dry" tool at the same resolution. The main obstacle using immersion lithography systems has been defects and other possible sources of yield loss.

Enhancements necessary to extend the technology beyond the 32 nm node are currently being investigated including the use of higher refractive-index materials in the final lens, immersion fluid, and photoresist. Currently, the most promising high-index lens material is lutetium aluminum garnet, with a refractive index of 2.14. High-index immersion fluids are approaching refractive index values of 1.7. These new developments allow the optical resolution to approach ~30 nm. However, it is expected that at some point below 40 nm, current photoresists will limit further scaling [5]. Polarization effects due to high angles of interference in the photoresist also have to be considered as features approach 40 nm [6]. Hence, new photoresists will need to be developed for sub-40 nm applications. On the other hand, double patterning has received interest recently since it can potentially increase the half-pitch resolution by a factor of 2. This could allow the use of immersion lithography tools beyond the 32 nm node, potentially to the 16 nm node. While double patterning improves pitch resolution, it must rely on non-lithographic methods, such as trimming, to actually reduce the feature size, possibly by as much as 50%.

1.2 Extreme UltraViolet Lithography

Extreme UltraViolet Lithography is the most promising next-generation technology for LSI fabrication using EUV wavelength (currently 13.5 nm). Semiconductor industry, research institutions, equipment makers, throughout the world are trying to develop the fabricating devices by EUVL according to the latest semiconductor road map that foresees to introduce for the fabrication of LSIs the 32-nm EUVL in 2011. This technology uses reflective optical system and mirrors covered with a multilayer film and can be considered an extension of conventional ultraviolet lithography. In contrast to conventional ultraviolet lithography, which employs refractive optics, EUVL employs a reflective optical system consisting of multilayer-coated *Extreme Ultraviolet Lithography* mirrors. Fig. 1.4 illustrates the principle of extreme ultraviolet lithography. The system consists of a source, a mask, an objective lens, illumination optics with light source, and a wafer. The mask, the objective optics, and parts of the illumination optics are coated with a reflective multilayer film. Since the aberration-free area in a reflective system is limited, the exposure area is expanded by synchronously moving the mask and wafer in the optical system. The Fraunhofer diffraction determines the diffraction-limited resolution when aberration in the optical system is completely eliminated:

$$d = \frac{K_1 \lambda}{NA} \quad (1.4)$$

The depth of focus, D, is given by the Rayleigh equation:

$$D = \frac{\lambda}{NA^2} \quad (1.5)$$

where λ is the wavelength of the X-ray source and NA is the numerical aperture of the objective lens. Tab. 1 gives estimates of the resolution and depth of focus, assuming for K_1 factor 0.5 and for wavelength 13.5 nm.

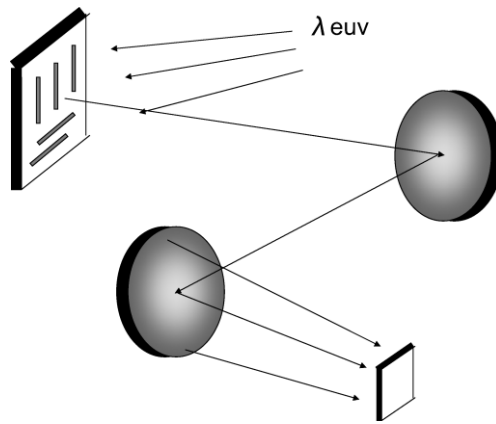


Fig. 1.4 EUVL working principle.

If a K_1 factor of 0.4 is permitted, optics with an NA of 0.25 can be used for the 22 nm-node without any narrowing of the depth of focus. This is an important advantage of EUVL. Fig. 1.5 shows the numerical aperture and X-ray wavelength for the target resolution and depth of focus. In this figure, a larger numerical aperture provides a higher resolution and a smaller depth of focus however, it is extremely difficult to design optics with a high numerical aperture (i.e. 0.4). Another way to improve the resolution is to shorten the wavelength but that reduces the reflectivity of the multilayer and narrows the bandwidth. Fig. 6 shows the reflectivity of multilayer films experimented in the world wide [7]. The shortest wavelength that can be used at normal incidence is around Tab. 1.1.

NA	0.25	0.3	0.4
d(nm)	27	22.5	17
D_f (nm)	216	150	84

Tab. 1.1 Resolution and Focus estimation.

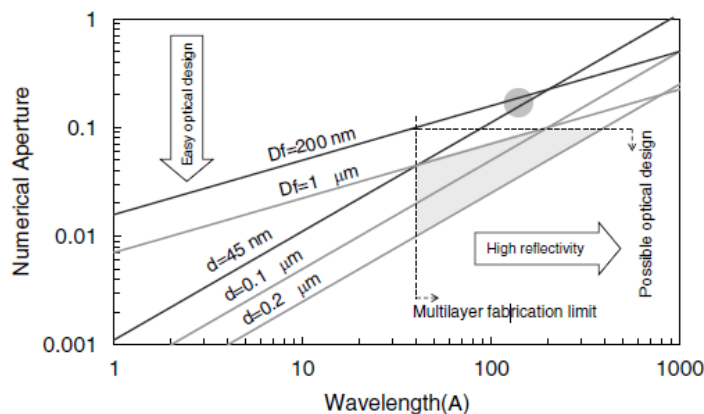


Fig. 1.5 Numerical aperture and X-ray wavelength for the target resolution and depth of focus.

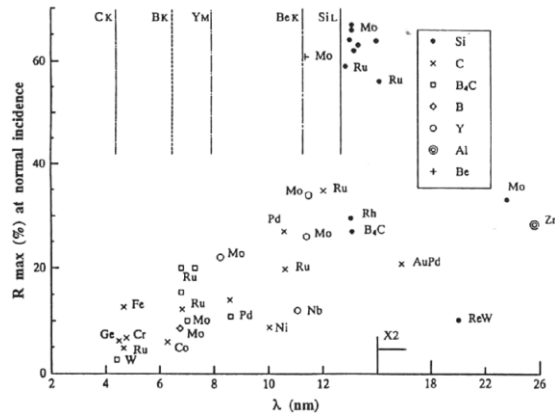


Fig. 1.6 The reflectivity of multilayer films fabricated and measured in the world wide.

Generally, the peak reflectivity is obtained at the wavelength of minimum absorption of the low index material, such as carbon, boron, beryllium or silicon for the wavelength range of 4.0–40 nm. The final selection of the wavelength will be decided on the basis of further studies on optical design for a high numerical aperture, the resist process, and the ability to deposit highly reflective multilayers. Tab. 1.2 shows the critical issues for EUVL components [8]:

Component	Issue	Goal
Optics	Design	6 mirrors
	Aspherical-mirror fabrication	0.3 nm
	Alignment accuracy of optics	0.5 nm
Source	High power	115–180 W
	Low debris	>5 st
	Large collection angle	>10 ¹¹
	Long life	
Mask	High reflectivity	>67%
	Low defect density	0.001/cm ²
Resist	High sensitivity	2-5mj/cm ²
	Low LER	1.5 nm @32 nm
Exposure system	Containment & temp. control	
	Mask & wafer handling	
	Scan stage	

Tab. 1.2 Critical issues in individual EUVL technologies.

The light source is based on Xe or Sn plasma. Power output exceeding 100 W is a requirement for sufficient throughput. While state-of-the-art 193 nm excimer lasers offer an output of 200 W/cm² [9] lasers for producing EUV-generating plasmas need to be more intense, about 10¹¹ W/cm². This indicates the enormous energy cost imposed by switching from generating 193 nm light (laser output approaching 100 W) to generating EUV light (required laser or equivalent power source output exceeding 10 kW). The EUV mask is one of the key technologies for establishing EUV lithography, with the production of defect-free substrates and phase defect measurements being critical issues.

An EUV mask (Fig. 1.7)[8] consists of an Low Thermal Expansion glass substrate, a multilayer, a capping layer, a buffer layer, and an absorber pattern [10]. The use of LTE glass for EUV mask substrates is essential for reducing mask distortion caused by thermal loading during EUV exposure [11].

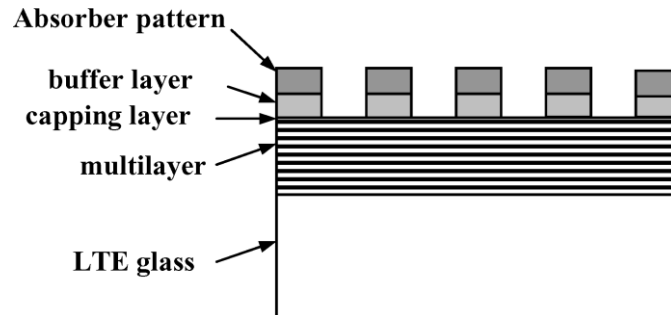


Fig. 1.7 The configuration of EUVL mask.

EUV masks can be produced without a significant drop in EUV reflectivity by optimizing the mask process and by using newly developed mask blanks. The fabrication of defect-free masks is a critical issue in EUVL. Mainly there are two types of defects (amplitude and phase) in an EUVL mask (see Fig. 1.8). Amplitude defects are either particles on the surface of the multilayer or flaws in the multilayer. They can be detected directly by measuring the intensity of Deep UV light scattered from them. Phase defects are produced when the multilayer is deposited over a bump or pit on the substrate, which results in swellings or depressions on the surface. There are two techniques for detecting a small swelling on the surface: using DUV ($\lambda = 257 \text{ nm}$) light and using EUV light at the exposure wavelength.

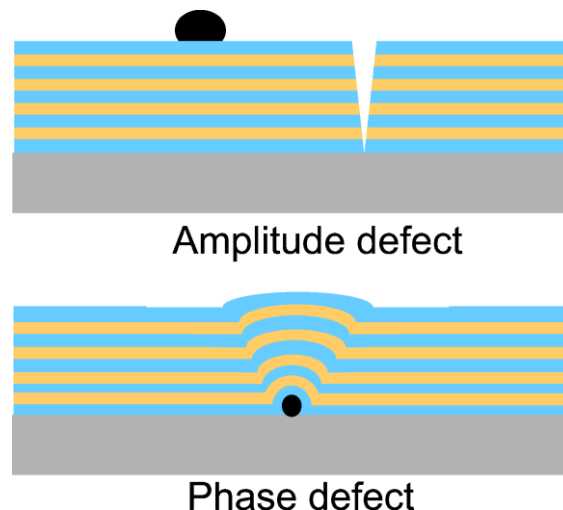


Fig. 1.8 Two types of defects in an EUVL mask.

The use of DUV light is the conventional method in optical lithography. However, it is difficult to detect defects on an EUVL mask by this method because the defects that need to be detected are much smaller than the inspection wavelength. That is, it is extremely difficult to detect defects of 50 nm or less using DUV light.

Furthermore, since the characteristics of phase defects depend on the exposure wavelength, it is necessary to observe phase defects at the same wavelength as that used for exposure [12].

1.3 Nanoimprinting

Nanoimprinting is a simple nanolithography process with low cost, high throughput and high resolution. It is commonly used to refer to both physical thermal embossing methods [13] and the more recent “step-and-flash” imprint photopolymerization techniques [14]. Both techniques have been demonstrated to possess resolutions below 25 nm. Moreover, the costs for imprinting methods could be up to an order of magnitude lower than other current lithography tool sets with comparable resolution. The principle of nanoimprint lithography is quite simple. Basically It uses the idea that if we can make a high-resolution template using a different process such as EBL and we can then use that same template as a mold to produce high-resolution features in a high-throughput process. The hard mould contains nanoscale features defined on its surface to emboss into polymer material cast on the wafer substrate under controlled temperature and pressure conditions (see Fig. 1.9) [15], thereby creating a thickness contrast in the polymer material, which can be further transferred through the resist layer using O₂ plasma based anisotropic etching process. Moreover nanoimprint lithography has the capability of patterning sub 10 nm features [16].

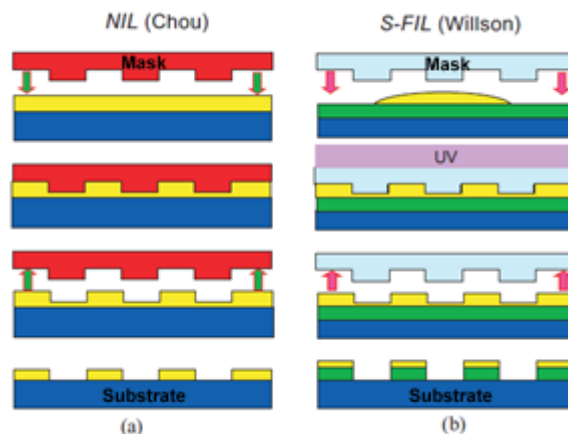


Fig. 1.9 Schematic of NIL (a) and S-FIL (b) [15].

S-FIL is another printing method [17] (Fig. 1.9(b)). In the S-FIL process, the substrate is first coated with an organic transfer layer; then a surface-treated, transparent template with surface relief patterns is brought close and aligned to the coated substrate. Once in the proximity, a drop of low viscosity, photopolymerizable organosilicon solution is introduced into the gap between the template and the substrate. The organosilicon fluid spreads out and fills the gap under capillary action. Next the template is pressed against the substrate to close the gap, and the assembly is irradiated with UV light, which cures the photopolymer to make it a solidified and a silicon-rich replica of the template. The mould in the nanoimprint technique can be considerate like the photomask in photolithography.

Both NIL and S-FIL utilize hard moulds to replicate patterns, which distinguishes them from the widely studied μ CP technique, which uses a soft and flexible poly(dimethylsiloxane) (PDMS) stamp. The hard features on NIL moulds and S-FIL templates can allow imprinting of features in polymer materials with resolutions below 10 nm, which is not possible to achieve by other similar techniques (for example by microcontact printing μ CP), using a soft stamp.

Hard moulds have mostly been made of Si or SiO₂ for nanoimprinting, while it is also possible to use a metal as the mould material. Important parameters for choosing mould materials are hardness, compatibility with traditional microfabrication processing and thermal expansion coefficient.

1.4 Focused Ion Beam

Focused Ion Beam systems operate in a similar way to a scanning electron microscope (SEM), that will be discussed in details in this chapter, except for the use of a finely focused beam of ions that can be operated for imaging or for site specific sputtering or milling. Many different ion sources can be used [18], but the most efficient is the liquid gallium (Ga) source. As shown in Fig. 1.10, the gallium (Ga⁺) primary ion beam hits the sample surface and sputters a small amount of material, which leaves the surface as either secondary ions (i⁺ or i⁻) or as neutral atoms (n⁰). The Ga self-assembles into a sharp tip (diameter \cong 2 nm) at high electric field and from this Ga⁺ ions are extracted. These ions pass through a column in which there are electrostatic lenses that focus them on the sample. The primary beam also produces secondary electrons (e⁻). As the primary beam modifies the sample surface, the signal from the sputtered ions or secondary electrons is collected to form an image in a way similar to a SEM. At low primary beam currents, very little material is sputtered and the FIB works as a microscope. At higher primary currents, a great deal of material can be removed by sputtering, allowing precision milling of the sample down to nanoscale. For very precise milling, a large number of repeated scans are made with low beam currents.

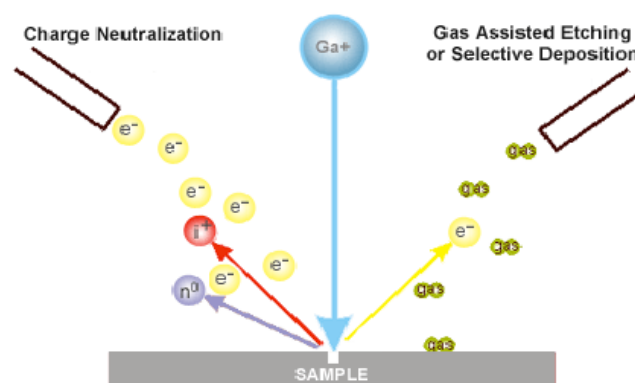


Fig. 1.10 FIB working principle.

The resolution that can be achieved in this way is nominally the imaging resolution (\sim 30 nm). This resolution is to be meant as the minimum spot size available, which is limited by chromatic aberration due to the distribution of ion energies and the Gaussian profile of the beam. This means that the thicker is the film to cut, the smaller is the actual resolution achievable.

In order to avoid charging of the specimen, the milling ions have to be neutralized after collision. In conductive samples this is simply done by providing the neutralizing charge through the stage and the sample holder. If the sample is non-conductive, a low energy electron flood gun can be used to provide charge neutralization. In this manner, by imaging with positive secondary ions using the positive primary ion beam, even highly insulating samples may be imaged and milled without a conducting surface coating, as would be required in a SEM. In contrast to other forms of lithography, FIB processing requires no masking with resist, post-FIB wet or dry etching, or resist removal. Another important advantage is the possibility offered by the FIB to operate in 3 dimensions. For the reasons above, FIBs are being increasingly used for a range of applications, including the site-specific preparation of transmission electron microscope (TEM) specimens, failure analysis in the semiconductor industry, and micromachining applications. FIB processing inevitably leads to Ga implantation. The effect of Ga⁺ implantation is particularly important in magnetic materials. Irradiating magnetic materials, even with fluencies of Ga as low as to produce topological changes smaller than 1 nm, strongly changes the magnetic properties of the irradiated material. In particular, it has been observed [19] that the coercivity reduces faster than the saturation magnetization and, when the fluence approaches a few thousand of ions per spot, the material becomes completely paramagnetic. This means that making a cut with the ion beam the film has become paramagnetic close to the cut edges over a distance given by the lateral straggling. A way to reduce this problem is to deposit a protecting metal layer on the film, assuming that the upper layer can be afterwards removed by chemical etching with a solvent that does not react with the film of interest.

1.5 Electron Beam Lithography

Electron beam lithography technology consists of the electron irradiation of a surface covered with a resist sensitive to a focused electron beam [20]. This technology uses a direct write system, in contrast with projection systems that require the use of masks to define the patterns, avoiding in that way the effect of diffraction. The employ of the narrow electron beam, the same used also for the Scanned Electron Microscope allows high resolution images (up to 1000k magnification) and in the same way high resolution patterns. The SEM is the core of the apparatus and includes: the electron source, the focusing system and the support for the sample substrate; in simple words the EBL is an electronic interface attached to the SEM in order to control the deflection, interruption and the energy of the beam plus a software to transfer the designed geometry. The energetic absorption in the resist causes chemical phenomena that define the features in the polymeric layer. This lithographic process comprises three principal steps: deposition of a thin resist layer (by spin coating), exposure of the sensitive polymeric material, development by an appropriated solvent to obtain pattern transfer. A great number of parameters, conditions and factors within the different subsystems (i.e. substrate, material, thickness of the resist, pattern dimension) are involved in the process and contribute to the EBL operation and result. The energy absorbed during the exposure process creates a latent image that comes out during chemical development. For positive resists, the development eliminates the patterned area, instead for negative resists, the inverse occurs.

1.5.1 EBL based system

The Fig. 1.11 shows the different parts that are integrated in the EBL system. The SEM provides a beam with emission stability, perfectly circular and minimal diameter. This is accomplished working at ultra high vacuum (UHV) level conditions. The control of beam deflection keeps beam integrity and, at the same time, precise enough operation to define the design exactly, dimensionally calibrated and accurately positioned on the sample. In addition to this, the beam blanking should be fast enough to avoid imprecisions and the mounting stage might allow exact positioning by a laser interferometer. All these aspects require a computer based system control that is capable of managing all subsystems, fast and simultaneously.

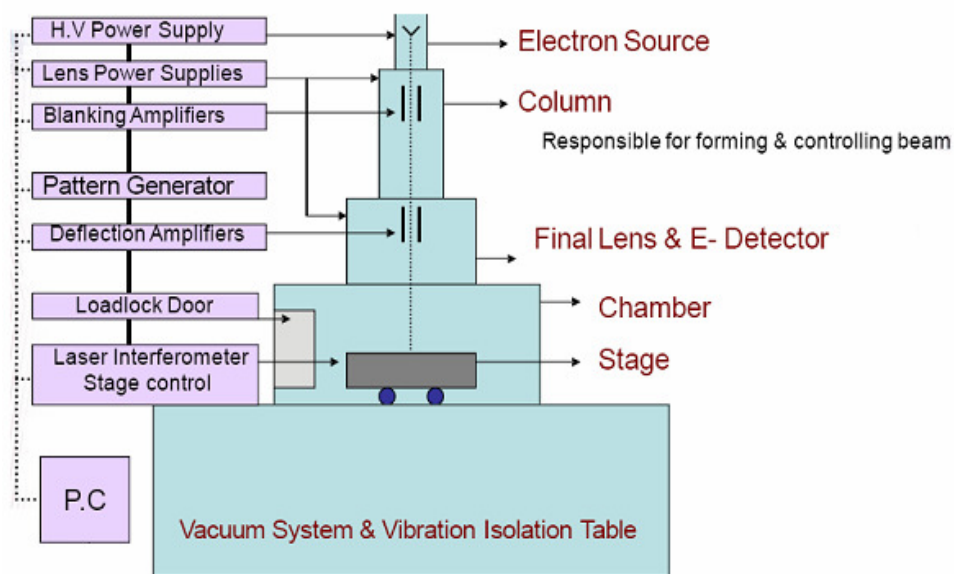


Fig. 1.11 Brief diagram of EBL system.

1.5.2 Electron gun

The electron gun (source) is a part of the electron optics of the SEM. It is composed of electrodes that extract and accelerate the electrons pulled off from the filament. For high resolution, the effective size of the source and the emission energy bandwidth must be small, which determines field emission sources (in comparison to thermionic sources) as the most convenient sources for SEM and EBL [21]. Analogous to light sources, the virtual size of the source, the brightness and energy dispersion characterize electron beam sources [22]. The virtual size of the source determines the demagnification that has to be applied by the SEM column. The smaller the virtual size is, the smaller the beam spot on the sample with a minimum number of lenses. The beam brightness is equivalent to the intensity in conventional optics. High value is desired to minimize exposure process time but high resolution lithography is accomplished only with lower beam intensities.

The energetic dispersion refers to the energy distribution of emitted electrons.

source type	Brightness (A/cm ² /sr)	source size	energy spread (eV)	vacuum requirement (Torr)
tungsten thermionic	~10 ⁵	25 μ m	2 - 3	10 ⁻⁸
LaB ₆	~10 ⁶	10 μ m	2 - 3	10 ⁻⁸
thermal (Schottky) field emitter	~10 ⁸	20 nm	0.9	10 ⁻⁹
cold field emitter	~10 ⁹	5 nm	0.22	10 ⁻¹⁰

Tab. 1.3 Comparison between source types.

The mechanism for electron extraction on field emission sources relies in the application of an electric field, high enough to enable electrons to traverse the surface potential barrier. Since the emitter works very close to the extraction electrode and at low voltage, the tip radius has to be sharp and made of a material with reduced work function. Tungsten tips provide the extremely high fields necessary for electron extraction. Intensity fluctuations in the beam current caused by tip absorption are reduced with UHV. The thermoionic field emission sources (Schottky) are the best choice due to combination of the best characteristics of field emission sources with the characteristic properties of thermic sources (see Tab. 1.3). Thermic sources emission occurs by heating of conductive material. This combination is less sensitive to environmental conditions, the source life time is increased and allows to obtain electron emission at 1800 K. In particular, one configuration of thermal field emission is composed of a tungsten needle covered by a zirconium oxide layer. The needle emits electrons, whereas the covering layer reduces work function and replenishes the material rejected from the tip.

1.5.3 SEM column

The main components of the SEM column are: the electron source (described previously), the objective lenses and the beam deflection unit (see Fig. 1.12).

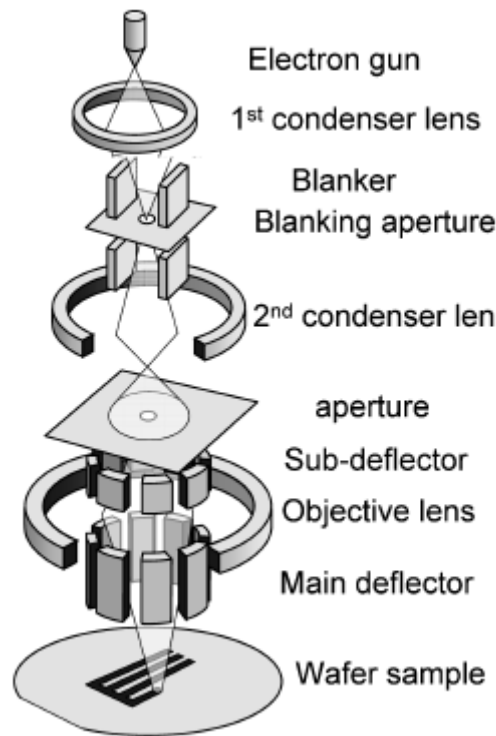


Fig. 1.12 Schematic of SEM column [23].

The electron optics is responsible of focusing and steering the beam and their operation principles can be explained using basic laws of electromagnetism. Electrons behaves as waves under determined conditions, which implies that can be focused and manipulated analogous to the classical geometric optics. At the same time, electrons maintain the characteristic properties of classical charged particles. The trajectory and speed of electrons can be controlled by electromagnetic forces (Newton's second law). The Coulomb law expresses that the force exerted by an electric field on an electron is parallel and opposite to the applied field and Lorentz law describes the force acting on an electron travelling in a magnetic field as perpendicular to the force and to the particle speed [24]. The result is the equation:

$$\mathbf{F} = q(\mathbf{E} + \mathbf{v} \times \mathbf{B}) \quad (1.6)$$

In general, both forces are not used simultaneously to steer the electron beam. Electrostatic lens force electrons to converge in some point of the optical axis. The realization is accomplished by three plates provided with a central aperture. Central plate (see Fig. 1.13b) has variable potential and the first and third plate are connected to the ground [22]. In general, electrostatic lenses are used as condenser lenses of the electron gun, since the distortions inherent to these lenses are less critical here. Electrostatic lenses usually produce higher spherical and chromatic aberrations, therefore magnetic lenses are preferred to focus the beam. In that case an electron with certain tangential velocity respect to the optical axis (the beam axis) interacts with the radial magnetic force that is created by the coil. In consequence, the electron experiences a force that leads it towards the beam axis [25]. Anyway to reduce the aberration the working distance must be reduced.

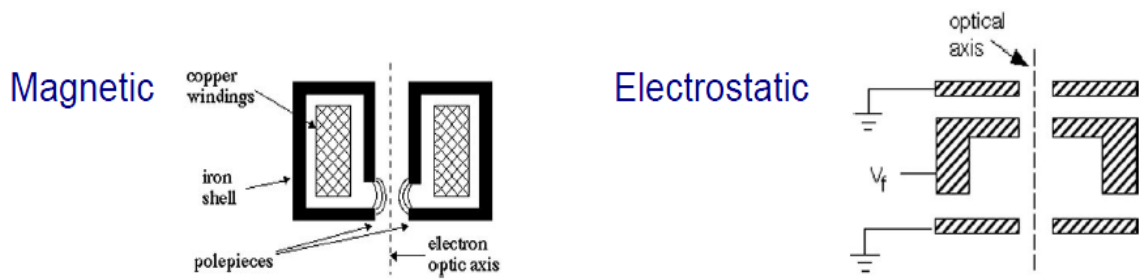


Fig. 1.13 Section of a magnetic(a) and electrostatic(b) electron lens.

Neglecting the actual aberrations that exist in the beam trajectories, electrons are focused to a certain distance, f , from the center of the lens, determined by magnetic field B_0 , the gap L_g , the ratio $e/m = \eta$ and the electron velocity (expressed by the V_0).

$$f \cong \frac{8V_0}{L_g \eta B_0^2} \quad (1.7)$$

Similarly to the focusing lenses, deflection can be realized both electrostatically or magnetically. It is implemented with coils and plates that create fields perpendicular to the optical axis. The magnetic deflection again introduces less distortions, but the electrostatic deflection has faster response. In addition, deflection unit is usually placed at the end of the column, which means that interaction with metallic conductive portions should be avoided. Shielding is used to minimize parasitic currents. The introduction of dynamic corrections, by means of the beam driving software, solves the main existing aberrations. The rest of elements that constitute the column are the apertures, astigmaters and the beam blarker. The holes that beam traverse along the column are called apertures. There are two kinds depending on their function: for limiting the beam or to interrupt it. Those used to limit the beam determine the amount of beam current and the convergence angle α (which is the angle of the beam respect to the sample surface). Due to this, apertures are very important, since they conditionate the effect of lens aberrations and, consequently, the resolution. The aperture that intercepts the deflected beam, performs the switch on and off of the beam on the sample. The beam blarker is comprised by a pair of plates connected to an amplifier with fast response. The potential applied to the beam deflects it far from the column axis until the beam passes through the aperture mentioned above. For EBL by vector scan strategy (in which the beam only scans in the areas that should be patterned), it is important that the time necessary for interrupting the beam is very short compared to the time that it takes to irradiate a pixel on the sample. In addition, it is basic that beam does not move during pixel exposure, in order to avoid distortions on the exposed design. The imperfections in fabrication and assembling of the column are the cause of astigmatism, causing that, for each sample surface position, focus conditions are slightly different. This means that the ideal circular section of the beam becomes elliptic and, consequently distorts the image. Concerning to lithography, beam shape does not correspond to the model used for calculating the exposure dose, therefore the pattern to be transferred is also distorted from the original design. The astigmator system is responsible of correcting beam shape to be circular again. It consists of four or eight poles that surround the optical axis. Adjustment is performed by the balance of electrical signal of the poles.

The imaging resolution is crucial for focusing, deflection calibration and alignment marks detection. Another important component for EBL systems is the Faraday cup that is used to measure the beam current and hence, to adjust the electron dose during the exposure.

1.5.4 Chamber and stage and Vacuum system

The lithographic process is performed in the SEM chamber where the samples can be fixed by clip holders. These provide also to get a good electric contact in conductive samples to neutralize the charge received from the beam through the stage and the sample holder (a detail in Fig. 14). The dimensions and mobility of the chamber determine the size and accessibility of the sample that can be patterned. The capabilities of the system benefit from precise and motorized controlled displacements. In addition it is equipped with a CCD (charge coupled device) camera to visualize inside the chamber and to assess the control of sample positioning. Another important aspect related to the chamber is the presence of vibrations and electromagnetic noise that can distort the beam. Support is isolated from mechanical vibrations, which is even more critical for high resolution EBL than it is for conventional lithography. At the same time, computer monitors, transformers and vacuum pumps are kept separate or controlled and shielding is used to avoid interferences [22]. It is necessary to work in high vacuum conditions inside the column because the beam performance and resolution is strongly conditioned by the performance of the vacuum system. In general, SEMs are equipped with two vacuum levels. Inside the column, UHV (in the order or lower than 10^{-9} Torr) is maintained, whereas the chamber level is less strict (lower than 10^{-6} Torr). Usually a first rotary pump is used to supply the vacuum level that allow the operation of the second pump. It is typically a turbomolecular pump that implements the chamber vacuum level. Inside the column, an ionic pump is used to reach the UHV required for the beam operation. The SEM includes a valve that isolates the column when chamber is vented to load samples.

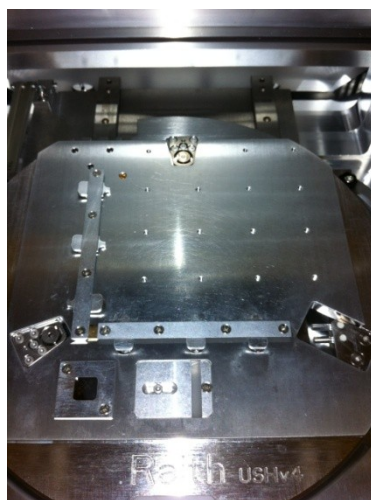


Fig. 1.14 Load Lock and clip holders of Raith 150.

1.5.5 Scan techniques in direct writing EBL

The lithography is performed by scanning the designed pattern, cell by cell, with the electron beam of circular section. In general, the design features are fragmented into rectangles or parallelograms and beam irradiation is executed with control over deflection and switch on and off of the beam (Fig. 1.15).

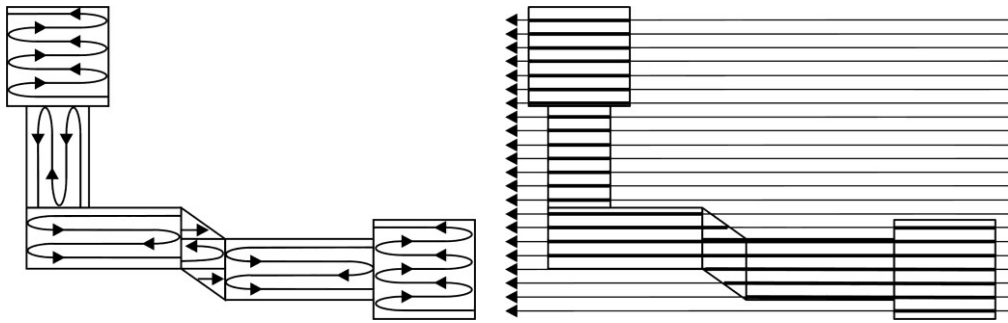


Fig. 1.15 vector scan mode (a) raster scan mode (b).

Vector scan mode is time efficient, since the beam only is scanned in the areas that should be patterned. On the contrary, for raster scan mode the beam is driven all over the working area and shape is controlled switching on and off the beam. Both methods are serial and, therefore, compared to conventional lithography fabrication time is higher and the working area is smaller. Another characteristic of this method is the flexibility to access, control or adjust most of process parameters. The way to steer the beam takes advantage of the possibility to determine the coils performance, which are used by SEM to scan the sample surface during imaging. Analogic control of the potentials deflects the beam from the beam axis (where potential/current is zero) until maximal deflection angle (measure of working area). It is implemented by using a PC with a card for digital to analogic conversion (DAC) and connection to the deflection system of the SEM. With DAC of 16 bits for each axis, accessible area is defined by 65536 x 65536 positions, that constitute the field. The field is the maximal area that can be exposed with the beam deflection. The Gaussian vector scan mode is the evolution of the method presented above. The original design is fragmented in subelements that will be continuously exposed by the beam of Gaussian intensity profile (see Fig. 1.16).

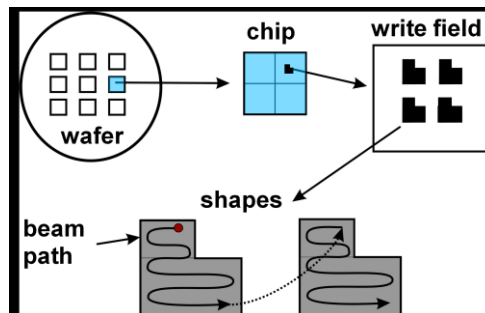


Fig. 1.16 Representation of fragmentation and scan direction of the designs [26].

For each subelement the beam is switched off and it is directly driven to the next portion. In order to operate with this strategy, two DACs are used: one to conduct the deflector that locates the beam in the corner of each subelement and the second to drive the beam within the subelement. If the area of the design is bigger than the field size, a second fragmentation of the design has to be done. Due to this, motorized support and positioning system by laser interferometric stage is convenient, to optimize the stitching precision. The operation of beam exposure is completed with the determination of beam speed that depends on the amount of charge per unit area that the resist must receive (Dose). The exact value to fully expose the whole resist thickness and to precisely define its shape and dimensions is specific for each resist and its intrinsic characteristics. During irradiation, dose is adjusted by determining the time that beam remains in each pixel (called area dwell time). It's automatically calculated by Raith's software, see Fig. 1.17, once known the beam current (measured using the Faraday cap) and chosen the area dose that depends and the resist parameters and the dimension of the pattern.

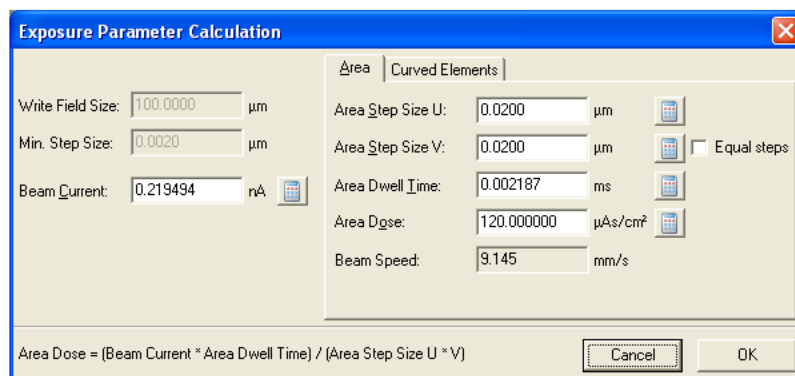


Fig. 1.17 Detail of the software in which is possible to set the exposure parameters.

1.5.6 Limitations on EBL resolution

Some limitations are present due to the intrinsic configuration of the EBL system: the maximal area of the writing field, the numerical aperture and the resolution are restricted from the diameter and shape of the beam in the focus point. The electron source has determined characteristics of brightness, emission, uniformity, stability and life time. Principally the limitations of the electron optics, which determines beam resolution. Different from conventional optical lenses, electromagnetic lenses are only converging. In reference to aberrations, their quality is so poorer that field size and convergence angle (numerical aperture) are limited. From electron source specifications, the beam diameter as a function of virtual source and column reduction is determined. The distortions caused by the column arise as spherical aberrations (astigmatism) and they are originated in both the lenses and the deflectors. Chromatic aberrations appear when electrons present a certain energetic spectra. From quantum mechanics, the resolution limit caused by diffraction can be determined by:

$$\lambda_{e^-} = \frac{1.226}{\sqrt{V_{e^-}}} (nm) \quad (1.8)$$

It is significantly lower to the one of the light used for photolithography because of the wavelength attributed to energetic electrons.

In general, the theoretical effective beam can be expressed as the quadratic sum of each contribution and optimal point is a compromise between all involved factors. For high resolution, the use of high magnification and beam energy is combined with low energetic dispersion and short focal distance. In consequence, write field is smaller and beam current should be reduced, what means that exposure process is slower, throughput is limited, and flexibility is constrained. In Tab. 1.4 are summarized the principal limitation on EBL resolution:

<i>Theoretical beam size</i>	$d = \sqrt{d_g^2 + d_s^2 + d_c^2 + d_d^2}$
<i>Virtual source size (beam diameter)</i>	$d_g = d_v \frac{1}{M}$
<i>Spherical aberrations</i>	$d_s = \frac{1}{2} C_s a^3$
<i>Chromatic aberrations</i>	$d_c = C_c a D \frac{V}{V_b}$
<i>Diffraction limit</i>	$d_d = 0.6 \frac{\lambda}{a}$

Tab. 1.4 Limitation on EBL resolution.

where M is the magnification and a is the beam convergence angle.

1.5.7 Electron-solid interaction and the proximity effect

Another phenomena that strongly conditions the final resolution of EBL is the beam-resist interaction and the polymer characteristics. As the electrons penetrate the resist, they suffer many small angle scatter events very inelastic (called *forward scattering*), which effect is to broaden the beam diameter (see Fig. 1.18). It's possible to minimize this effect by using thinnest possible resist and highest values of acceleration voltage. When the angle scattering of the electrons is large, mainly elastic, we talk about *backscattering*. In this case the electrons may return back through the resist at a significant distance from the incident beam, causing additional resist exposure.

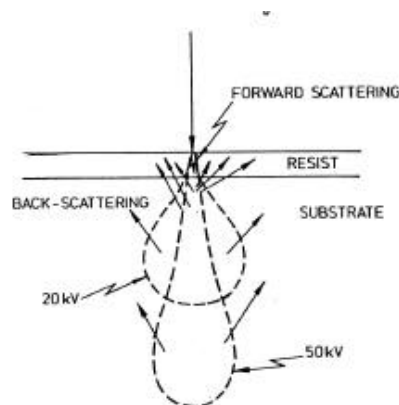


Fig. 1.18 Scheme of electron solid interactions.

Thus the electron-solid interactions may cause that absorbed dose is not confined to the zone where beam has been driven. This fact, called “*proximity effects*”, causes dimensional mismatch and design distortions (see Fig. 1.19).

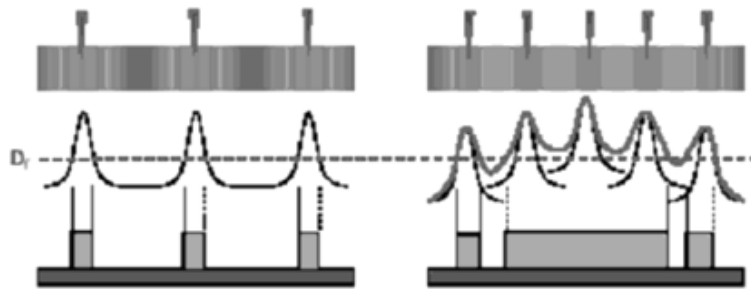


Fig. 1.19 Representation of electron dose absorbed in the case of isolated (left) or areal (right) features.

The effective exposure in a point depends on the position of the others exposed point. The electrons at the resist-substrate interface suffer a back-scattering and contribute to give a small dose to the near points. The choice of system configuration or exposure conditions can minimize it, for example, the use of very thin layers or beam energy selection and also the design program can allow to correct the proximity effect. Moreover there are mainly two correction methods (assisted by the Raith software) to prevent the proximity effect: “dose scaling” that changes the incident exposure dose in each shape and eventually cuts with different dose scaling in parts of structure, and “pattern biasing” (shape correction) that reduces of structure dimension or adds structures at underexposed areas. An example of the application of these correction methods is shown in Fig 1.20.

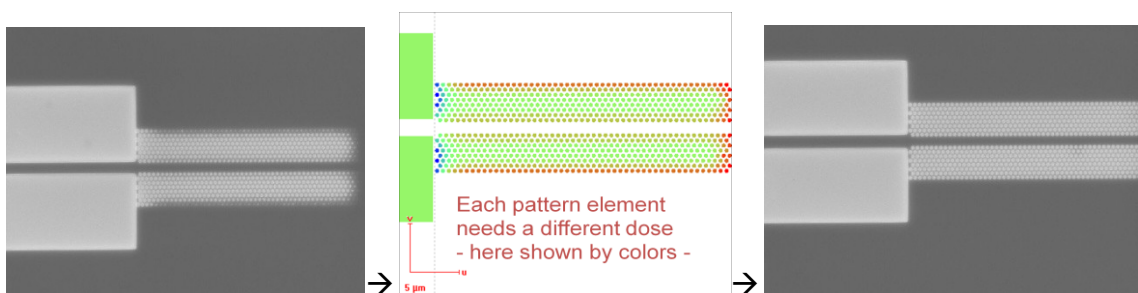


Fig. 1.20 Correction methods for proximity effect.

It’s also possible to estimate the proximity effect by a MonteCarlo simulation of forward scattered and back scattered electrons (see Fig. 1.21).

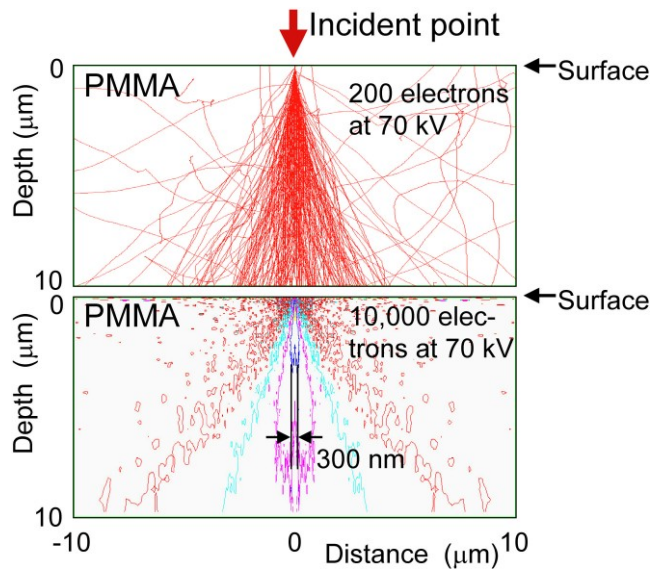


Fig. 1.21 Electron trajectories (up) and distribution of energy deposited in PMMA resist (down), obtained by Monte Carlo simulation [23].

1.5.8 Computer control

The operation of direct write EBL relies on the delivery of the electron dose: the resist, sensitive to electrons, is exposed sequentially according to the design elements [27]. The offline data processor determines the order, geometry and size of irradiation. Computer based control is responsible of design, exposure rhythm (beam deflection speed), adjustment of exposure field (size and compensation of position, rotation and orthogonality) and stage positioning. The lithography is performed by scanning the designed pattern, cell by cell, with the electron beam of circular section. In general, the design features are fragmented into rectangles or parallelograms and beam irradiation is executed with control over deflection and switch on and off of the beam (Fig. 1.16). The design files are organized by jerarquic structures in databases of extended GDSII format that included the information of exposure parameters (i.e. area dose, aperture size, pattern design). In addition, it is CAD file compatible with GDSII, DXF and CIF formats, or ASCII database. In any cases, the use of external files is based on the conversion to the internal GDSII. The visualization and edition is completely graphic and it allows flexible and fast data manipulation. In particular, the program allows to draw as basic structures, rectangles, polygons, circles, ellipsoids, lines, dots, etc in separated layers for multilevel exposure. An image of the software is shown in Fig. 1.22.

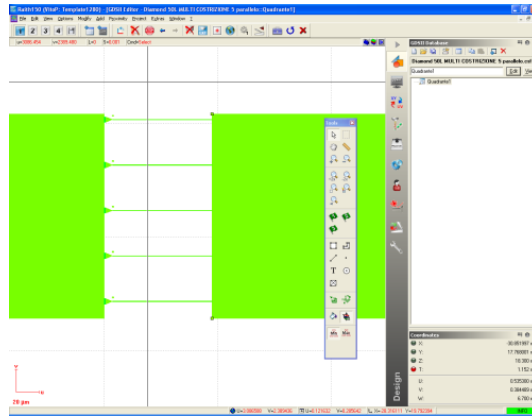


Fig. 1.22 Sample image of CAD software.

Text can be included, together with practical information for documentation (date and time of exposure). It includes a generator of mathematical functions to create curves matrices or many actions to modify the basic structures: translation, scaling, iteration, deleting, merging, etc.

1.5.9 Equipment

The Nanofabrication Laboratory at the ICIB-CNR is equipped with Raith 150. It is based on a Thermal field emitter ZrO/W filament. The microscope nominal resolution is 1 nm, beam energy range is from 0.2 to 30 keV, beam size is 1,6 nm at 20 kV and beam current range is 5 pA-5 nA (drift <0.5%/hr). Magnification varies from 24x to 1000kx, six apertures are available, 7.5, 10, 20, 30, 60, 120 μm in diameter, two detectors (Inlens, for backward scattered electrons and SE2 for secondary electrons) are used, 8" wafers can be introduced in the chamber and stage movements are motorized in XYZ and rotation. The beam is Gaussian type and the scan technique is fast vector scan including the possibility to expose Single Pixel Line, dots and Fixed Beam Moving Stage to expose lines longer than write-field area without stitching. EBL system has been operated in Clean Room conditions, Class 1000, where temperature is 24°C and relative humidity ranges, typically, from 30 to 50 %.



Fig. 1.23 EBL system at the Nanofabrication Laboratory in the ICIB-CNR.

1.5.10 Photoresist

1.5.10.1 Poly(methyl methacrylate)

The resist mainly utilized in this thesis is Poly(methyl methacrylate) (PMMA) was the first polymer tested as a resist for EBL [28] and still continues to be the most widely used. It performs as a positive tone resist under EBL, X-rays and Deep UV radiation. The exposure induces the scission of the chain of methacrylic monomers that constitute the resist material [29]. It is generally accepted that the main process consist of the break of the main chain, but other scission possibilities may also occur (Fig. 1.24).

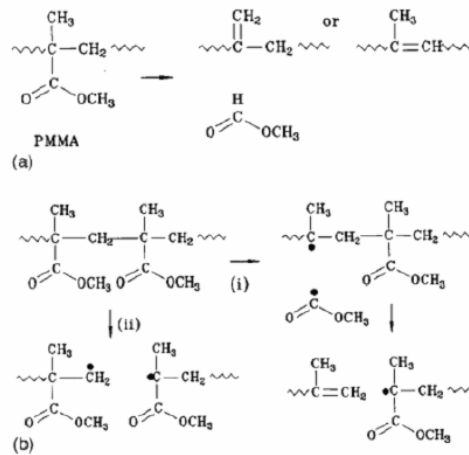


Fig. 1.24 Schematic diagrams for the generic reaction paths caused by EBL on PMMA, from [29].

PMMA demonstrates good properties that make it a convenient choice for a great number of applications due to its high resolution (less than 20 nm) minimal swelling during wet development. Glass transition temperature is moderate, 114 °C. PMMA can be used as a mask for acid, base and ion etching, but its performance in plasma is poorer.

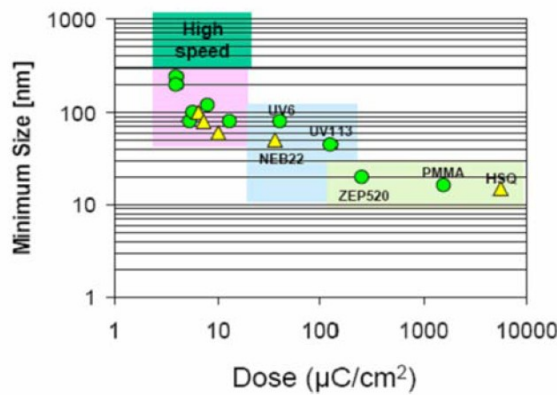


Fig. 1.25 Comparison of performance for different positive and negative electron beam resists [28] exposed at 100 keV. Representation of sensitivity in function of resolution. PMMA has high resolution, but requires higher doses than ZEP520.

In Fig. 1.25, PMMA is compared to other existing resists in function of dose and resolution. As can be seen, fast resists (low clearing dose) present low resolution, whereas the highest resolution tends to medium-low sensitivity. PMMA is commercialized in solution to be deposited as thin layers (down to 50 nm) by spin coating. Casting solvents are chlorobenzene or (safer) anisole and the control of the deposited thickness layer is achieved by the solution viscosity and the spin speed. There are different types of PMMA depending on the average weight of the molecular chains. The most used are 950k MW and 495k MW, but others exist, specially used for imprinting (PMMA 50k or 35k MW). It is considered that resolution scales proportionally with molecular weight, so higher molecular weights will allow higher resolution. This is due to the smaller size of the chain scission products in high MW polymers and, in consequence, higher resolution in the resist removal after development. On the other hand, sensitivity, and contrast, is inversely proportional to the molecular weight. This is attributed to a lower solubility in the developer for increasing relative molecular mass [30].

1.5.10.2 ZEP520

ZEP520 (Nippon Zeon Co.) is a positive-tone electron- beam resist with comparable resolution to (PMMA). Chemical structure of this resist is alternating a-copolymer of α -chloromethacrylate and α -methylstyrene (see Fig. 1.26) [31]. This resist has a better sensitivity (requires less dose) and resistance to etching processing (RIE) compared with PMMA (see Fig. 1.25) but is need to be completely shielded from sun light.

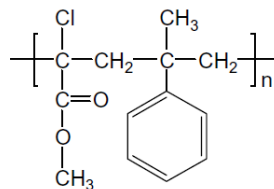


Fig. 1.26 Chemical structures of ZEP.

1.5.11 New frontier

The technological evolution in nanotechnology is really fast, driven by industry and research. Sub 5 nm half pitch lithography was presented by MIT (see Fig. 1.27). Raith et al. MIT optimized the chemistry and resist development process of HSQ. Final exposures were made using a RAITH150-TWO electron beam lithography system at Raith application labs.

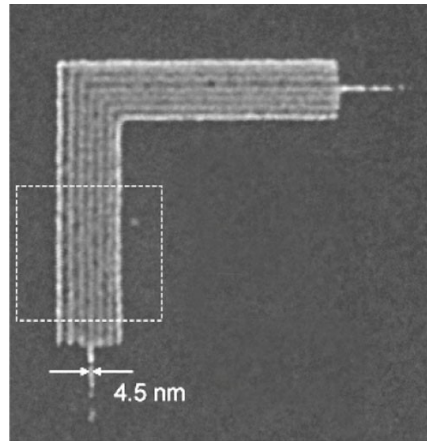


Fig. 1.27 Sub 5nm half pitch lithography by Raith.

The way is that of an hybrid approach. In fact this result can be useful also for fabrication of imprint master fabrication and pattern transfer processes or guided self assembly of pattern by sparse template and varying motifs [32].

References

- [1] DailyTech - IDF09 Intel Demonstrates First 22nm Chips Discusses Die Shrink Roadmap (2008).
- [2] E.D. Palik, Academic Press, Boston, Vol. 2 (1991).
- [3] M. Switkes, M. Rothschild, R.R. Kunz, S-Y. Baek, D. Coles and M. Yeung, "Immersion lithography: Beyond the 65nm node with optics," *Microolithography World*, p.4, May (2003).
- [4] M. Switkes *et al.*, *J. Vac. Sci. & Tech. B* vol. **21**, pp. 2794-2799 (2003).
- [5] U. Okoroanyanwu and J. H. Lammers, *Future Fab International*, Issue 17 (2004).
- [6] C. Wagner *et al.*, *Proc. SPIE* vol. 4000, pp. 344-357 (2000).
- [7] M. Yamamoto. *Soft X-ray Multilater*, *NEW GLASS*, **10**(2), 43 (1995).
- [8] H. Kinoshita *Nanofabrication Fundamentals and Applications*, (2008) Tseng.
- [9] R. Paetzel *et al.*, *Proc. SPIE*, Vol. 5040, 1665 (2003).
- [10] Andrew m. Hawryluk, Natale M. Ceglio and David P. Gaines, Reflection mask technology for x-ray projection lithography, *J. Vac. Sci. Technol.*, **B7**(6), 1702–1704 (1989).
- [11] S. Gianoulakis and A. Ray-Chaudhuri, Thermal-mechanical performance of extreme

ultraviolet lithography reticles, *J. Vac. Sci. Technol.*, **B16**(6), 3440–3443 (1998).

[12] T. Terasawa, Y. Tezuka, M. Ito and T. Tomie, High-speed actinic EUV mask blank inspection with dark-field imaging, *Proc. SPIE*, **5446**, 804 (2004).

[13] Resnick D J *et al* 2003 *J. Vac. Sci. Technol. B* **21** 2624.

[14] Taniguchi J, Tokano Y, Miyamoto I, Komuro M, Hiroshima H, Kobayashi K, Miyazaki T and Ohya H (2000) *Japan. J. Appl. Phys. Part 1—Regular Papers Short Notes Rev. Papers* **39** 7070.

[15] L Jay Guo *J. Phys. D: Appl. Phys.* **37** (2004) R123–R141.

[16] Chou S Y, Krauss P R, Zhang W, Guo L J and Zhuang L 1997 *J. Vac. Sci. Technol. B* **15** 2897.

[17] Colburn M *et al* 1999 *Proc. SPIE* **3676** 379–89.

[18] J. Melngailis, *J. Vac. Sci. Technol. B* **5**, 469 (1987).

[19] C. Chappert, H. Bernas, J. Ferré, V. Kottler, J.-P. Jamet, Y. Chen, E. Cambril, T. Devolder, F. Rousseaux, V. Mathet, H. Launois, *Science* **280**, 1919 (1998).

[20] A. A. Tseng, K. Chen, C. D. Chen, and K. J. Ma *Electron beam lithography in nanoscale fabrication: recent development* IEEE Transactions on Electronics Packaging Manufacturing, 141-149 26 (2003)

[21] T. H. P. Chang, M. G. R. Thomson, M. L. Yu, E. Kratschmer, H. S. Kim, K. Y. Lee, S. A. Rishton, and S. Zolgharnain *Electron beam technology - SEM to microcolumn*

[22] D.J. Grant *Electron Beam Lithography: From Past to Present* University of Waterloo (2003)

[23] A. Tseng *Nanofabrication: Fundamentals and Application* World Scientific, 2008

[24] P.W. Hawkes *Electron optics and electron microscopy* Taylor & Francis, London (1972)

[25] Herriot and Brewer *Electron beam technology in microelectronic fabrication* Academic Press NY (1980)

[26] R. Bojko EBFM manual Cornell University

[27] M.A. McCord *Handbook of Microlithography, micromachining and microfabrication*. SPIE (1999)

[28] I. Haller, M. Hatzakis, and Srinivas.R *High-Resolution Positive Resists for Electron-Beam Exposure* IBM Journal of Research and Development (3), 251 (1968)

[29] E. Reichmanis and A. E. Novembre *Lithographic Resist Materials Chemistry* Annual Review of Materials Science 23 , 11-43 (1993)

[30] V. M. Bermudez *Low-energy electron-beam effects on poly(methyl methacrylate) resist films* Journal of Vacuum Science & Technology B (6), 2512-2518 (1999)

[31] Hiromi IKEURA-SEKIGUCHI et. al *Ionic degradation products of ZEP520 resist film* Materials Science 27A/2004G127

[32] Raith - New products, functionality and better specifications (2010)

Chapter 2: Nanopatterning for advanced physics

2.1 Superconducting nanowires for advanced optical detection

Among superconducting electronics applications, the development of advanced detectors represents one of the field more explored by the scientific community in the last years. Recently, the search for novel and high performances optical detectors achieved a great interest due to particular characteristics which are proper of the superconducting state. In fact, when the optical wavelengths to be detected is confined up to the near-infrared, the superconducting technology offers the better answers in terms of response time, wavelength responsivity, quantum efficiency, and minimum detectable power. Superconducting devices are very attractive as radiation sensors because of their quantum nature and low-noise cryogenic operation environment. Moreover, the superconducting energy gap 2Δ is two to three orders of magnitude lower than the energy gap in semiconductors; thus, each absorbed optical photon (energy $\sim eV$) is able to generate a large number of secondary excited carriers after its absorption, in the superconducting matter [33]. Submicron-width NbN superconducting nanostructures [34] demonstrated to be high efficiency superconducting single-photon detectors (SSPDs) due to their ultrafast timing, high sensitivity to both visible and NIR photons, and very low dark counts [35]. These devices have already found some practical applications in non-contact debugging of CMOS very-large scale integrated circuits [36], and recently their uses is going on toward practical Quantum Communication (QC) systems. Moreover fast SSPD's are also of great interest for other single photonics applications, such as single-molecule fluorescence, high-resolution astronomy, and quantum metrology.

2.1.1 Ultrathin superconducting nano-bridge: the working principle

After the absorption of a light quantum $h\nu$ in a superconductor, a highly excited electron is created [37]. Due to the large physical size (ξ coherence length) of a Cooper pair, only one electron absorbs a photon, while the second one becomes a low-energy quasiparticle (QP). This excited electron rapidly loses its energy via electron-electron ($e-e$) scattering (on a femtosecond time scale) and creation of secondary electrons. The $e-e$ process continues until the average energy of excited electrons becomes approximately the Debye energy: at this time the most efficient mechanism for redistribution of energy is the emission of Debye phonons by electrons ($e-ph$ process). The mean free path of these phonons is very small and they break additional Cooper pairs. As the average energy of electrons in the avalanche decreases down to values close to the energy gap, their number increases, reaching ideally $h\nu/2\Delta$. The effective electron temperature T_e increases locally during this energy cascade, resulting in local suppression of superconductivity, and a formation of a region called "hotspot". The time evolution of the hotspot depends on the QP and phonon relaxation processes, which are highly nonlinear. In fact, phonons emitted during the energy cascade can have enough energy to break other pairs, leading to the so-called "phonon bottleneck", limited by the phonon escape time from the superconductor.

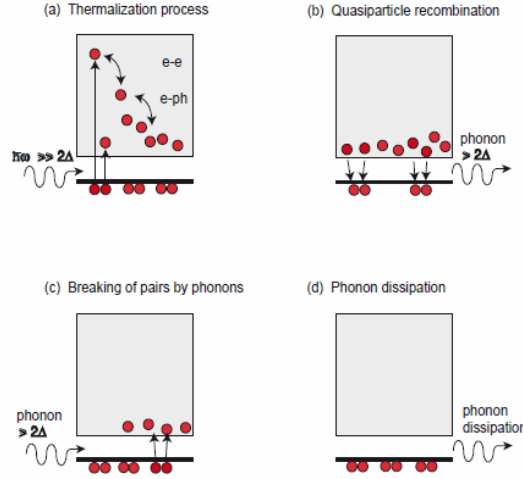


Fig. 2.1.1 Illustration of the superconducting carrier dynamics when illuminated with light radiation. (a) The photon energy is absorbed and breaks a Cooper pair, a large number of quasiparticles is generated through electron-electron and electron-phonon interactions. (b) The quasiparticle starts to recombine back to form Cooper pairs and emit phonons in the process. (c) If the energy of the phonon is sufficient it can break more Cooper pairs. (d) Eventually all the energy escapes out to the substrate via phonon coupling [37].

Fig. 2.1.1 shows the various processes occurring after a photon absorption process in a superconductor, and the subsequent nonequilibrium generation and relaxation of QP's. A single 800-nm-wavelength photon is able to produce, in an ultrathin superconducting NbN film, a cascade consisting of >300 QP's on a time scale (phonon escape) of less than 30 ps [38]. In SSPD's the QP avalanche results in an electrical pulse and it allows for a precise detection of the photon arrival, while the picosecond QP relaxation ensures up to GHz repetition rates for superconducting NbN photon counters.

The carrier relaxation dynamics was mathematically modeled by Rothwarf and Taylor [39], who proposed two coupled kinetic equations that describe the interplay between the 2Δ phonons and the quasiparticles, valid especially for devices that work at a temperature well below the critical temperature:

$$\begin{cases} \frac{\partial N_{qp}}{\partial t} = I_{qp} + 2\tau_B^{-1} N_{qp} - RN_{qp}^2 \\ \frac{\partial N_{ph}}{\partial t} = I_{ph} - \tau_B^{-1} N_{ph} + \frac{R}{2} N_{qp}^2 - \tau_{es}^{-1} [N_{ph} - N_{phT}] \end{cases} \quad (2.1.1)$$

where N_{qp} , N_{ph} , and N_{phT} are the numbers per unit volume of quasiparticles, 2Δ phonons, and thermal equilibrium phonons respectively. I_{qp} (I_{ph}) is the external generation rate for the quasiparticles (phonons), and R is the recombination rate for the quasiparticles into Cooper pairs. Under weak perturbation, the RT equations can be linearized and the quasiparticle recombination time τ_R can be introduced as:

$$\tau_R^{-1} = RN_{qp} \quad (2.1.2)$$

The number of excited quasiparticles is an important parameter for explaining superconducting detectors' performances, i.e. the kinetic inductance mode (KI). When photons with energy typically much larger than 2Δ are absorbed by a superconducting film at $T \ll T_C$, they produce a time-dependent population $\Delta n_q(t)$ of non-equilibrium quasiparticles, bringing to a temporary decrease in the superconducting fraction of electrons expressed as: $f_{SC} = (n_0 - n_{qp})/n_0$ (obtained solving RT equations), where $n_{qp} = n_{qp}(0) + \Delta n_{qp}(t)$ is the instant concentration of the quasiparticles, $n_{qp}(0)$ is their equilibrium concentration and n_0 is the total concentration of electrons. Because the pairs are characterized by nonzero inertia, this process can be modeled as time-varying kinetic inductance [40,41]:

$$L_{KIN}(t) = \frac{L_{KIN}(0)}{f_{SC}} \quad (2.1.3)$$

where $L_{KIN}(0) = \mu_0(\lambda_L)^2/d$ is the equilibrium value per unit area of the film, λ_L is the magnetic penetration depth and d is the film thickness. Hegmann and Preston introduced a detailed kinetic-inductive photoresponse model for YBCO thin films [42]. According to this model, the kinetic inductance L_{kin} in the superconductor sensor of length l , width w , and thickness d can be expressed as:

$$L_{KIN} = \frac{m}{n_{SC}e^2} \left[\frac{l}{wd} \right] = \mu_0 \lambda_L^2 \left[\frac{l}{wd} \right] = \frac{1}{\epsilon_0 \omega_p^2} \left[\frac{1}{f_{SC}} \right] \left[\frac{l}{wd} \right] \quad (2.1.4)$$

where m is the effective mass of the superconducting carriers, n_{SC} is the density of superconducting carriers in a two fluid model, μ_0 is the permeability of free space, ϵ_0 is the permittivity of free space, λ_L is the temperature-dependent London penetration depth, ω_p is the plasma frequency and f_{SC} is the superfluid fraction equal to n_{SC}/n where n is the total density of carriers. A laser pulse absorbed in the superconductor will break Cooper pairs and reduce f_{SC} from its initial value f_{SC0} , thus increasing L_{kin} . If a constant current bias I_B was applied to the superconductor sensor, a voltage will develop across the sensor due to an acceleration of the superconducting carriers from the change in L_{kin} . The transient voltage that develops is proportional to the bias current and the rate of change of the kinetic inductance, and it is expressed as follows:

$$V_{KIN}(t) = I_B \frac{dL_{KIN}}{dt} \quad (2.1.5)$$

This equation predicts a positive voltage while the superfluid fraction is decreasing followed by a negative voltage as the superfluid density recovers to its starting value.

2.1.2 The Hot-Spot model

A SSPD prototype consists of a submicrometer superconducting stripe, comparable in dimension (width of stripe) with the QP diffusion length and the hotspot size, whose radius is about the electron thermalization length λ_T [37].

The device is maintained at a temperature lower than the critical temperature T_c and it is biased at a current I close to the critical current I_c . The photoresponse mechanism can be schematized as in Fig. 2.1.2.

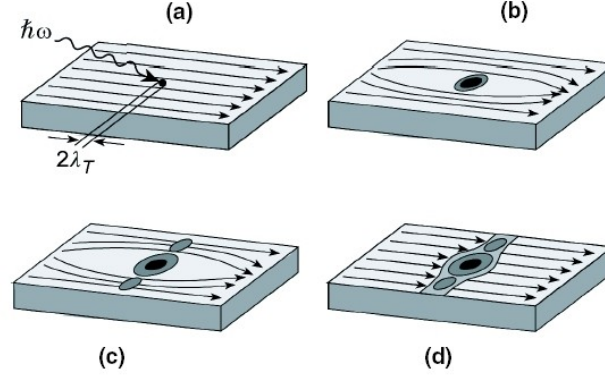


Fig. 2.1.2 Schematics of the hotspot generation and supercurrent-assisted formation of a resistive barrier in an ultrathin and sub-micron width superconducting stripe kept at temperature far below T_c . Arrows indicate flow direction of biasing supercurrent [37].

After photon absorption, a localized hotspot region, with suppressed or even destroyed superconductivity, is formed within the initial hotspot [Fig. 2.1.2(a)]. The initial hotspot size is determined by the $h\nu/2\Delta$ ratio, as well as the QP thermalization time and its diffusivity. During the $e-ph$ thermalization, the hotspot grows [Fig. 2.1.2(b)] as hot electrons diffuse out of the hotspot core. The supercurrent, which biases the device, is expelled from the resistive hotspot volume and is concentrated in the "sidewalks" near the edges of the film [Fig. 2.1.2(c)]. If the current density after this redistribution exceeds the critical value outside the hotspot a resistive barrier is established across the entire width of the device [Fig. 2.1.2(d)]. This resistive barrier gives a rise to a voltage signal with the amplitude proportional to the applied current. After this growth phase, the hotspot starts to decrease due to the relaxation and out-diffusion of excited QP's. Thus, in ultra-thin NbN, after ~ 30 ps of relaxation time, the hotspot collapses, superconductivity is restored (zero voltage state) and the detector is ready to detect another photon [43]. To study in deep the hot spot creation it considers a thin film of normal resistivity ρ holding a current density J , in the situation where a hot spot has formed (Fig. 2.1.3a). The Joule power generated, ρJ^2 per unit volume, is shared between the heat flux to the substrate, $C\tau^{-1}(T - T_b)$ per unit area, (C =specific heat per unit volume) and a longitudinal component which can be equated $-k(\partial^2 T/\partial x^2)$ per unit cross section of the film. Here, $T(x, t)$ is the position and time-dependent temperature of the film and k is the bulk coefficient of thermal conductivity of the superconductor, related to D , the diffusivity of heat, by $k=C\cdot D$. All parameters are assumed to be temperature independent, and identical (except ρ) in the normal and superconducting part of the system. In the normal state, the heat rate equations are verified:

$$C \frac{\partial T}{\partial t} = k \frac{\partial^2 T}{\partial x^2} - \frac{C}{\tau} (T - T_b) + \rho J^2 \quad (2.1.6)$$

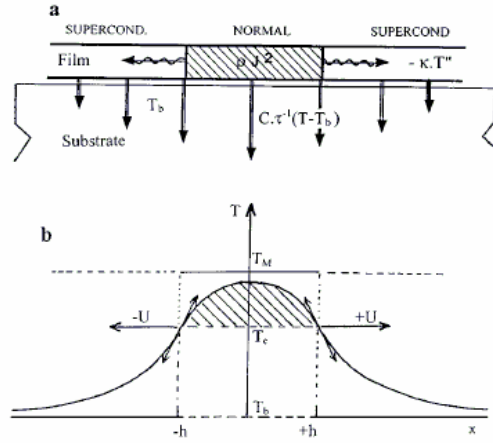


Fig. 2.1.3 (a) Thermal transfers into and out of a hot spot: dissipation ρJ^2 above T_c , heat conduction along the film – $\kappa T''$, and escape to the substrate, proportional to $(T - T_b)$. (b) Hot spot temperature profile at instant t . T_b : bath temperature; T_M : asymptotic temperature. U is the HotSpot wall velocity [44].

and a similar equation (excluding the term ρJ^2) in the superconducting regions. At the superconducting/normal interface, the two temperatures equal T_c and the first space derivatives ($\partial T/\partial x$) must be equal. A progressive solution of this coupled set can be found, with an interface velocity U given by:

$$U = \frac{y^2 - 2}{\sqrt{y^2 - 1}} \sqrt{\frac{D}{\tau}} \quad (2.1.7)$$

Here y is the ratio I/I_1 , with $I_1 = \text{Volume} \cdot (C(T - T_b)/\tau\rho)^{1/2}$: Eq. (2.1.7) predicts not only the positive values of U but also an interval $I_1 < I < I_h$, where U is defined and negative. Then, the situation is that of a receding hot spot with a central temperature $T > T_c$. A plausible temperature profile at a fixed instant is drawn in Fig. 2.1.3b. It is constrained between the limits T_b and T_M such that

$$\rho J^2 = C \cdot \tau^{-1} (T_M - T_b) \quad (2.1.8)$$

In 2001 Gol'tsman et al. [11] experimentally demonstrated the supercurrent-assisted, hotspot-detection mechanism for single optical (790 nm wavelength) photons. Fig. 2.1.4 shows a current–voltage ($I - V$) characteristics of a NbN microbridge (see Fig. 2.1.5) operated at 4.2 K and voltage biased. The characteristics is typical of a long superconducting constriction [45] and show that the bridge can be operated in either of the two distinct modes: the superconducting and the resistive state. The hotspot plateau under dc conditions corresponds to the growing normal-state region, as the voltage across the device is increased, eventually reaching the bridge normal-state resistance.

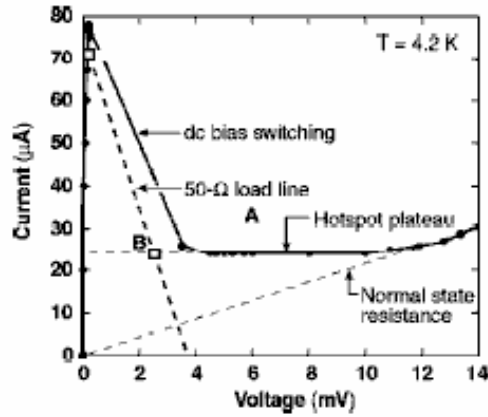


Fig. 2.1.4 I–V characteristics of a 0.2 mm wide and 1.2 mm long NbN superconducting microbridge are shown. Point A denotes the initial detector bias level in the superconducting state and point B corresponds to the switched state upon absorbing a photon, leading a voltage pulse generation, before relaxing back to point A [46].

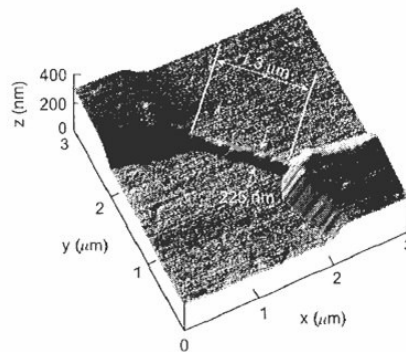


Fig. 21..5 AFM image of a 1.3 μm x 0.23 μm microbridge device [46].

For a device biased near, but below I_c (point A in Fig. 2.1.4), photon absorption triggers the supercurrent-assisted hotspot formation leading to a temporary switching from the superconducting state to the hotspot resistive state (point B in Fig. 2.1.4). As a result, an output voltage is generated with a magnitude corresponding to the voltage level at point B, which is independent on the actual photon energy, as long as the photon energy is sufficient to form a hotspot large enough to trigger the supercurrent redistribution effect. The response time of the voltage pulses followed the formation of the resistive state induced by the photon absorption [47]. (see Fig. 2.1.6)

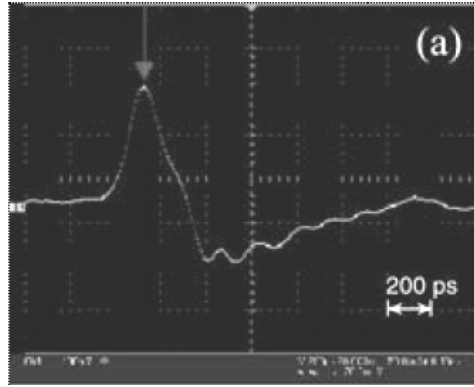


Fig. 2.1.6 Example of output pulse for a SNSPD microbridge [47].

The probability $P(n)$ of absorbing n photons from a given pulse is proportional to:

$$P(n) = \frac{e^{-m} m^n}{n!} \quad (2.1.9)$$

where m is mean number of photons per pulse. When $m \ll 1$:

$$P(n) = \frac{m^n}{n!} \quad (2.1.10)$$

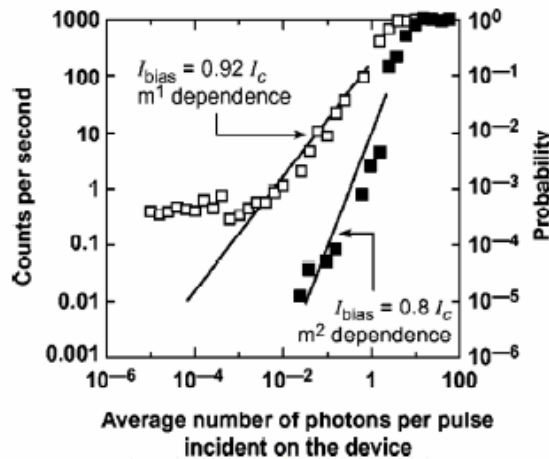


Fig. 2.1.7 Count rates and the corresponding counting probability for an NbN quantum detector as a function of the radiation intensity. Depending on bias current, the detector can count single-photon (open squares) or two-photon (solid squares) events [47].

Fig. 2.1.7 shows the probability of the detector producing an output voltage pulse as a function of the number of photons per pulse incident on the device area, at two different values of the bias current. The left vertical axis indicates the mean number of detector counts per second. The right vertical axis corresponds to the probability of detecting an optical pulse. Open squares correspond to the bias current $0.92 I_C$. When an high incident photon fluxes hit the SSPD there is a saturation effect, while for smaller fluxes, as predicted by Eq. (2.1.10), the experimental data show the linear decrease of detection probability with the average number of incident photons over four orders of magnitude, clearly demonstrating the single-photon detection.

At very low number of incident photons, experimental data points saturate at the level of 0.4 s^{-1} counts (probability 4×10^{-4}) since the experiment was performed in an optically unshielded environment. This level is regarded as the laboratory photon background. The solid squares in Fig. 2.1.7 correspond to the same device, operated under the same conditions as those for the open-square data, but biased with $0.8I_c$. Experimental data points now follow a quadratic dependence of detection probability, showing the two-photon detection.

2.1.3 Quantum Efficiency and Noise Equivalent Power

The detection mechanism in SSPD, as explained before, is based on the overcoming of the density of I_c in the superconductive path around the hotspot created by the absorbed photon. The hotspot extension depend on the energy of the incident photon, so in order to have a good sensibility to very low energy photons (i.e. NIR photons) a narrow nanowire is needed. Typical nanowires have a width of the order of $\sim 100\text{-}200 \text{ nm}$. On the other hand a so narrow detector has a very low active area for detection, so the hard goal is to have a large but sensitive. In order to increase the active area a meander structure is used (Fig. 2.1.8).

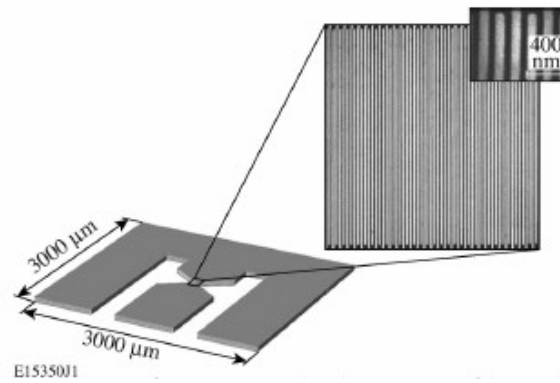


Fig.2.1.8 Topology of SNSPD contact pads and an SEM image of the meander (NbN is black) [47]. The contact pads allow connection to a 50- coplanar transmission line.

The efficiency of radiation detector is usually measured by the *Quantum Efficiency* (QE) parameter, defined by the ratio of the number of detected photon N_{REG} and of the number of incident photons N_{INC} , for a given time interval per the device area [48]:

$$QE = \frac{N_{REG}}{N_{INC}} \quad (2.1.11)$$

In continuous wave measurements, the value was determined from the power incident on the device nominal active area measured by a power meter. In experiments with pulsed sources, experimental QE is simply the probability of photon counting, measured at the one photon-per-pulse level, incident upon the SSPD nominal area and expressed in percent. Even when the SNSPD is in a complete dark condition, the device produces spontaneous voltage pulses similar to the photoresponse pulses.

These pulses are called dark counts and their rate is defined as their mean number occurring during a defined time. Fig. 2.1.9 shows an example of the dark-count rate R versus I_B . The curve follows a typical activation law dependence (with a and b constant):

$$R = a \cdot \exp\left(b \frac{I_B}{I_C}\right) \quad (2.1.12)$$

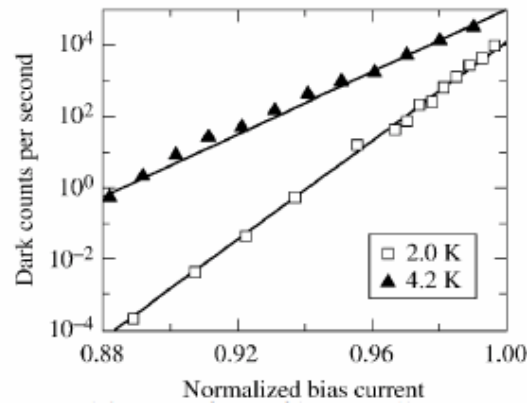


Fig. 2.1.9 SSPD dark counts versus normalized bias current at temp. of 4.2K and 2.0K [9].

An optimal operation regime of the SSPD is a trade-off between QE and R . The maximum value of QE corresponds to rather high (for example 1000/s). Quantitatively an good operational regime stays between QE and R ; it can be presented in terms of the noise equivalent power (NEP) [48], which can be defined for quantum detectors as:

$$NEP = \frac{h\nu}{QE} \sqrt{2R} \quad (2.1.13)$$

where $h\nu$ is photon energy.

2.1.4 The proximity effect

Recently it has been experimentally demonstrated [49] that the coupling between a superconductor and ferromagnet brings to a hybrid structure, which characteristics may be useful in the contest of SSPD. Generally when a superconducting layer (S) is put in contact with a non-superconducting film, that is normal metal (N) or ferromagnetic material (F), some physical properties of the former are transferred to the second within a certain spatial region. This phenomenon, named *proximity effect*, The interest in these hybrid structures is motivated by the fact that the two materials that form the bilayer S / N, we influence each other on a spatial scale order of the coherence length of the two layer (ξ_S e ξ_N). In particular, layer N may have an effect induced superconductivity, due to the penetration of Cooper pairs. In experiments based on superconducting tunnel junctions, proximitized bilayers, type Al / Nb, Ta / Nb and Al / Ta, were investigated by both experimental and theoretical point of view. A. Golubov et. al. [50] developed a proximity model, in which in the bilayer there is a spatial dependence of order parameter. This model is referred to S_1 / S_2 bilayers and was formulated starting from different studies on the effect of trapping in the particle detectors based on superconducting junctions.

To illustrate this model we consider a superconductor S_1 with a thickness d_1 , mean free path l_1 , coherence length $\xi_{S1,2}$, energy gap $\Delta_{1,2}$ and a second superconductor S_2 with a thickness d_2 , mean free path l_2 , coherence length $\xi_{S1,2}$, energy gap $\Delta_{1,2}$. Let's consider a bilayer formed by S_1 and S_2 and assuming for simplicity $\Delta_1 > \Delta_2$, in this case we will have a value of the energy gap $\Delta(x)$ at the interface between Δ_1 and Δ_2 with x perpendicular to the interface. Assuming that for the superconductors $l_{S1,2} \ll \xi_{S1,2}$ it is possible to characterize the proximity effect through two parameters:

$$\gamma = \frac{\rho_{S1} \xi_{S1}}{\rho_{S2} \xi_{S2}^*} \quad \gamma_B = \frac{R_B}{\rho_{S1} \xi_{S2}^*} \quad (2.1.14)$$

where $\rho_{S1,2}$ is the resistivity of the two materials in the normal state, R_B is the product of the interface $S_1 - S_2$ resistance to its area and $\xi_{S2}^* = \xi_{S2} \sqrt{\frac{T_{C2}}{T_{C1}}}$. The parameter γ quantifies the relationship between the density of quasiparticles at the interface of two superconductors while γ_B is a measure of transparency of the barrier between two superconductors. If $\gamma_B \ll 1$, then the potential barrier at the interface tends to zero, i.e. the two superconductors are in good electrical contact, while in the opposite case the two superconductors are weakly coupled. The Fig. 2.1.10 shows an example of change in the former parameters as a function of position for two proximitized superconductors:

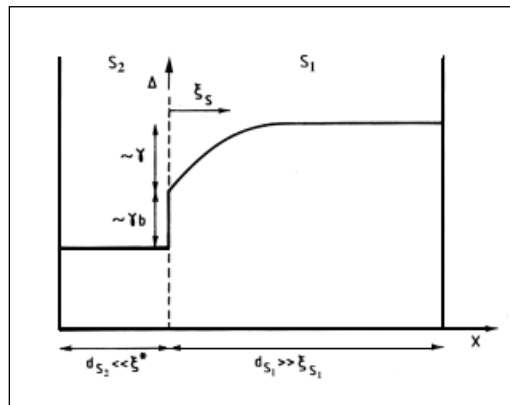


Fig. 2.1.10 Parameters of the proximity effect vs position.

When the N layer consists of weakly ferromagnetic material the situation is different. In these hybrid structures the superconducting order parameter decays over a distance of a few nm and it's modulated with the thickness of the ferromagnet. The resulting properties are "mediated": in an appropriately sized structure the characteristics of a superconductor can be joined to the electronic characteristics of a ferromagnet.

In fact, in the case of a bilayer S/F should be taken into account the asymmetric distribution of spin in the ferromagnet: in the S layer at low temperatures there is the formation of C_p , thus the total spin zero achieved through the combination (\mathbf{k}, \uparrow) and $(-\mathbf{k}, \downarrow)$, while in the F magnetic layer order prevails in the presence of a band of spin. To explain the transition of an electron from one state to another a quantum mechanism known as Andreev reflection [51] must be invoked.

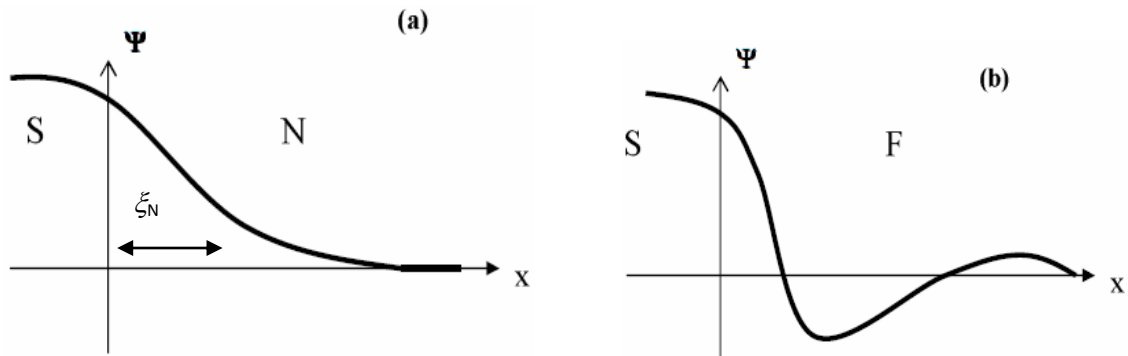


Fig. 2.1.11 Development of order parameter in S/N and S/F.

Thus while in the case S/N, the order parameter decays monotonically at the interface, in S/F it shows a damped oscillatory behavior as shown in Fig. 2.1.11. To obtain explicit ξ_f must distinguish two cases:

1) $\xi_0 \ll l$ where the ξ_0 is the coherence length of pure material and l is the mean free path of electrons, in this case results:

$$\xi_S = \frac{\hbar v_{FS}}{2\pi k_B T_c} \quad \xi_F = \frac{\hbar v_{FF}}{2\pi k_B T_{cS}} \quad (2.1.15)$$

where v_f is the Fermi velocity.

2) $\xi_0 \gg l$:

$$\xi_S = \sqrt{\frac{\hbar D_S}{2\pi k_B T_c}} \quad \xi_F^* = \sqrt{\frac{\hbar D_F}{2\pi k_B T_{cS}}} \quad (2.1.16)$$

where $D_{S(F)}$ is the diffusion constant. Assuming that $\frac{\gamma}{\gamma_B} \ll \min\left(\frac{d_S}{\xi_S}, \frac{\xi_S}{d_S}\right)$ we can obtain γ_B

from the equation [52]:

$$T_C = T_{cS} \left(1 - \frac{\pi^2 \gamma \xi_S}{4\gamma_B d_S} \right) \quad (2.1.17)$$

Once note γ_B and γ it's possible to get the transparency at the interface T [53]:

$$\gamma_B = \frac{2}{3} \cdot \frac{l_F}{\xi_F} \frac{1-T}{T} \quad (2.1.18)$$

The damped oscillatory behavior of the order parameter in the F layer depends on the thickness of the layer itself and the model predicts a non-monotonic dependence of T_c and the density of states (DOS). It can be created a structure of this type by diluting a conventional ferromagnet with another paramagnetic material such as in the case of nickel-copper alloy (NiCu).

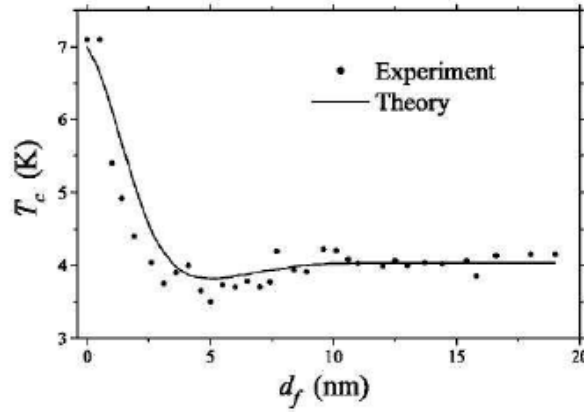


Fig. 2.1.12 T_c vs. d_f of Nb/NiCu.

Fig. 2.1.12 shows the behavior of T_c vs. d_f for a Nb/NiCu bilayers [52].

2.1.5 Dissipation and fluctuations in low-dimensional superconductors

Low dimensional nanostructures as fabricated in this thesis can be described in a two-dimensional (2D) limit. when one of the transverse dimensions is smaller than the Ginzburg-Landau (GL) coherence length ξ . A structure is (2D) when both transverse dimensions are smaller than ξ , it is considered to be one-dimensional (1D). It must be noted that, since 2D and 1D superconductors do not behave in the same way as bulk superconductors, different role of fluctuations are expected. The superconducting order parameter is described by a complex wave function [54]:

$$\psi(r) = |\psi(r)| e^{i\phi(r)} \quad (2.1.19)$$

which has the modulus corresponding to the local density of Cooper pairs:

$$|\psi(r)|^2 = n_s(r) \quad (2.1.20)$$

where r is the spatial coordinate, φ is the position-dependent phase. When we consider the superconducting transition, in 2D and 1D superconductors, the transition region is wider than that in the bulk materials. This is shown schematically in Fig. 2.1.13 [55].

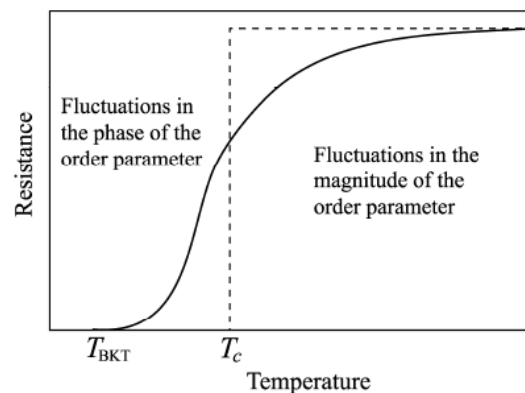


Fig. 2.1.13 Resistive transition in low-dimensional superconductors. Above T_c , the magnitude of the superconducting order parameter fluctuates, while below T_c , the phase of the order parameter fluctuates until a second transition temperature is reached [55].

The transition at T_c is dominated by fluctuations in the magnitude of the superconducting order parameter: this evidences in an increased conductivity before the transition [56]. At T_c , the magnitude of the order parameter becomes well defined, but the resistivity does not reach the zero sharply. The expansion of the transition is due to fluctuations in the phase of the order parameter, and when such phenomenology happens the phase “slips” by 2π . In 2D systems, destruction of the long-range order creates “topological” defects in the order parameter. This phenomenon was first investigated by Kosterlitz and Thouless [57], and independently by Berezinskii [58] (we’ll refer as BKT model). These studies brought to BKT model. The BKT model is applicable to phase transitions in a variety of 2D systems, such as planar spin systems, superfluid helium films, etc [59]. In 2D superconducting films, the topological defects are excitations due to thermal fluctuations, and they come in the form of vortex-antivortex pairs (VAPs). In fact, it can be observed (see Fig. 2.1.13) a second transition below T_c , called BKT transition T_{BKT} , below which the resistance goes to zero. In a temperature range between T_c and T_{BKT} both bound and unbound vortex pairs can exist. A vortex has the polarity of 2π (while an antivortex has polarity of -2π), and their movements produce dissipation (between T_c and T_{BKT}). Below the BKT transition vortices with opposite polarities combine into pairs, consequently the resistance goes to zero [59]. An applied current exerts a Lorentz force which reduces the VAP binding energy, and thermal fluctuations can subsequently break the VAPs [60]. These can manifest in a spontaneous transient resistive state. The VAPs are always present due to their finite excitation energies (of the order of $k_B T$), similarly to electron-hole excitations in semiconductors [61]. Nevertheless the application of BKT model to a superconducting film, requires some adjustments: a true BKT phase transition can occur only if the energy of a bound VAP depends logarithmically on separation r , and in superconductors this happens only when $r \ll 2\lambda_L^2/d$, where λ_L is the bulk London penetration depth [62].

If $r > 2\lambda_L^2/d$ the binding energy becomes proportional to r^{-2} , so the binding energy is strongly reduced, unbound vortices exist at all temperatures, and there is no true BKT transition. Then, to observe a BKT transition, one must be in the logarithmic regime, which limits the width of the film to $w \ll 2\lambda_L^2/d$. For dirty superconductors, this condition is easily satisfied as λ_L can be quite large. Moreover, the condition $w > 4.4\xi$ (Likharev's limit [63]) can be used to predict VAPs propagation. Below T_c , in the framework of the BKT model, the resistance due to free vortices is directly proportional to the free vortex density n_f , and is given by [62]:

$$R_{VAP}(T) = 2\pi R_N \xi^2(T) n_f(T) \quad (2.1.21)$$

where R_N is the normal-state resistance. At temperatures $T_{BKT} < T < T_c$, the resistance is given by Halperin and Nelson formula [62] as follows:

$$R_{HN} = 10.8b R_N \exp \left[-2 \left(\frac{T_c - T_{BKT}}{T - T_{BKT}} \right)^{1/2} \right] \quad (2.1.22)$$

where b is a non-universal constant of the order unity. This temperature dependence may be difficult to observe in samples with R_s less than 1 kOhm, as the transition region $\Delta T = T_c - T_{BKT}$ is quite small in such devices. The ratio T_{BKT}/T_c is given by [60]:

$$\frac{T_{BKT}}{T_c} = \left[1 + \frac{0.173 R_s e^2}{\hbar} \right]^{-1} \quad (2.1.23)$$

where ε is a renormalization factor on the order of unity to take into account VAPs with smaller separation interacting with VAPs with larger separation. Below T_{BKT} , and in the limit of zero current, the dissipation (free vortices) is due to finite-size effects. Then Eq. 2.1.21, in the limit of large length scale, can be rewritten as [59]:

$$R_{VAP}(T) = 2\pi R_N \left[\frac{T - T_{BKT}}{T_c - T_{BKT}} - 2 \right] \left(\frac{\xi(T)}{w} \right)^{\frac{T - 2T_{BKT}}{T_c - T_{BKT}}} \quad (2.1.24)$$

In order to achieve current-induced unbinding of VAPs, where the Lorentz force has to exceed the attraction force of the pair, a threshold current I_{th} must be overcome. This I_{th} increases with decreasing temperature, according to [59]:

$$I_{th}(T) = 2eK(l_m) \frac{kT}{\hbar} \quad (2.1.25)$$

where $K(l_m)$ is the stiffness constant from the Kosterlitz recursion equations, bounded by the width of the film, and is given by $K(l_m) = 2/\pi + 1/\pi \ln(w/\xi)$. Then, I_{th} can be rewritten as [64]:

$$I_{th}(T) \approx \left(1 + 2 \frac{T_c - T}{T_c - T_{BKT}} \right) \frac{2ekT}{\pi\hbar} \quad (2.1.26)$$

In this regime, the resistance due to unbinding of VAPs is predicted to be [64]:

$$R_{VAP}(T) \approx 4R_N \frac{T_c - T}{T_c - T_{BKT}} \left(\frac{I}{I_{sc}} \right)^{-2 \frac{T - T_c}{T_c - T_{BKT}}} \quad (2.1.27)$$

where $I_{sc} = wekT_{BKT} / \hbar \xi(T)$ is the scaling current.

2.2 Nanostructures for magnetoresistance based devices

The change of resistance, of a material after the application of an external magnetic field H is defined *magnetoresistance* (MR). The magnetoresistive effect depends classically both from the intensity of the applied magnetic field, and its relative direction with respect the driven current. It cannot be modeled by describing the transport properties simply by considering the idealized gas of free electrons and spherical Fermi surfaces. In fact the magnetoresistance effect is more evident in system characterized by more carrying charges, whose behaviors at sufficiently large fields is strongly dependent on the topology of the Fermi surface, derived by symmetry of the crystalline lattice and the electronic energy band occupation. In this chapter the physical properties of the MR effect will be reviewed with particularly emphasis to aspects directly involved in the work presented in this thesis. Moreover the theory of micromagnetism is reviewed and used to calculate width and energy of constrained domain walls (DWs) that are an important tool to driven the MR in nanostructured devices.

2.2.1 Microscopic exchange interaction

Ferromagnetism is a collective quantum mechanical phenomenon that supports parallel alignment of individual magnetic moments. It brings to a spontaneous magnetic moment even if no external magnetic field is applied. In the Heisenberg model, the effective Hamiltonian, which describes the interaction of N spins \mathbf{S}_i , can be write as [65]:

$$\mathcal{H}_{eff} = -\sum_{i,j=1}^N J_{i,j} \mathbf{S}_i \cdot \mathbf{S}_j = -2 \sum_{i>j}^N J_{i,j} \mathbf{S}_i \cdot \mathbf{S}_j \quad (2.2.1)$$

The “-” sign is used so that $J_{i,j}>0$, and corresponds to a ferromagnetic coupling. The Coulomb interaction, due to the overlap of the wavefunctions ϕ_i and ϕ_j , is written in terms of the *exchange integral*:

$$J_{i,j} = 2 \int \phi_i^*(\mathbf{r}_1) \phi_j^*(\mathbf{r}_2) \frac{e^2}{|\mathbf{r}_1 - \mathbf{r}_2|} \phi_i(\mathbf{r}_2) \phi_j(\mathbf{r}_1) d\mathbf{r}_1 d\mathbf{r}_2 \quad (2.2.2)$$

The *exchange interaction* has an electrostatic origin but the explanation involves quantum mechanics. In the case of interacting atoms (functions ϕ not orthogonal), a rough estimation of the exchange integral J always leads to a negative value. If one considers simple systems, such as the H_2 molecule, the negative exchange is easy to understand: the two electrons would prefer (due to the Coulomb term) to be near to both nuclei. Pauli exclusion forbids parallel spins occupying the same space; therefore the anti-parallel state is lower in energy. A simple physical argument can be given to understand the positive exchange integral in some systems: as a consequence of the Pauli exclusion principle, it can be energetically convenient for two electrons to have separate orbits and thus a reduced Coulomb interaction. Yet, a first principle calculation using Eq. (2.2.2) is usually misleading. Even for reasonable assumptions about the functions ϕ the computation leads always to negative exchange integral. As an example from experiments, ferromagnetism is found in the $3d$ transition metals (Cobalt, Nichel and Iron), and thus the exchange integral must be positive. Ferromagnetism in metals is easier to explain by the *Stoner criterion*, which ignores the first principle calculations and assumes $J_{i,j}>0$ to give a phenomenological justification for the appearance of ferromagnetism. It must also be added

that Eq. (2.2.2) refers to the so-called “direct” exchange interaction and it is not suitable to explain ferromagnetism in more complex materials like manganites where “double” exchange interaction is the dominant mechanism.

2.2.2 Ferromagnetism in metals

In metallic solid-state materials, electrons can move themselves freely through the lattice, so well-defined electronic states are spread into dispersive bands. Firstly consider a simplified density of states (DOS):

$$N(E) = 4\pi \left[\frac{2m_e}{h^2} \right]^{3/2} \sqrt{E} \quad (2.2.3)$$

with m_e the electron mass, h Planck's constant, and E the electron energy. The total of electrons per unit of volume n , is obtained by integrating $N(E)$ over energy, up to the *Fermi level* (E_F), the maximum occupied energy at temperature $T = 0$ is:

$$n = \int_0^{E_F} N(E) dE = \frac{8\pi}{3} \left[\frac{2m_e}{h^2} \right]^{3/2} E_F^{3/2} \quad (2.2.4)$$

Therefore the DOS can be write as:

$$N(E) = \frac{3n}{2E_F^{3/2}} \sqrt{E} \quad (2.2.5)$$

which at the Fermi level is:

$$N(E_F) = \frac{3n}{2E_F} \quad (2.2.6)$$

For the Pauli exclusion principle, at each energy level there are two electrons, each with a different spin quantum number. The spin degeneracy has already been taken into account in Eq. (2.2.3), so the DOS per unit of energy for each spin channel is simply half of the full DOS (Fig. 2.2.1a):

$$N_{\uparrow\downarrow}(E) = 2\pi \left[\frac{2m_e}{h^2} \right]^{3/2} \sqrt{E} \quad (2.2.7)$$

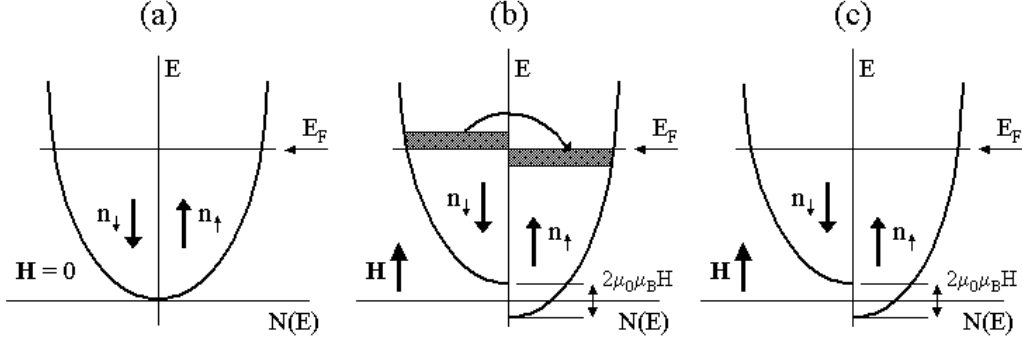


Fig. 2.2.1(a) Spin resolved density of states is balanced in zero magnetic field. **(b)** Application of a field shifts the sub-bands by the Zeeman energy **(c)** Redistribution up to the Fermi level results in an unequal population of spin states.

$$N_{\uparrow\downarrow}(E) = 2\pi \left[\frac{2m_e}{h^2} \right]^{3/2} \sqrt{E} \quad (2.2.8)$$

When a magnetic field H is applied (Fig. 2.2.1b), the additional energy (*Zeeman energy*) will shift the spin-up and spin-down band with an amount $\mu\mu_0 H$, with μ the projection of the electron magnetic moment along the H axis, corresponding to $\pm \mu_B$, with μ_B the *Bohr magneton*. On a very short time scale, the electrons with spin-down (those with magnetic moment opposite to the field) will flip their spin to be accommodated in the spin-up band. This will continue until, at equilibrium, both bands are again filled up to the Fermi level (Fig. 2.2.1c). In this new situation, we can evaluate the number of spin-up and spin-down electrons occupying both sub-bands as:

$$2n_{\uparrow} = \int_{-\mu_0\mu_B H}^{E_F} N(E + \mu_0\mu_B H) dE = \int_0^{E_F + \mu_0\mu_B H} N(E) dE \quad (2.2.9a)$$

$$2n_{\downarrow} = \int_{+\mu_0\mu_B H}^{E_F} N(E - \mu_0\mu_B H) dE = \int_0^{E_F - \mu_0\mu_B H} N(E) dE \quad (2.2.9b)$$

The magnetization of the conduction electrons can be obtained as the population difference (per unit of volume) multiplied by the electron magnetic moment:

$$M = (n_{\uparrow} - n_{\downarrow}) \mu_B \quad (2.2.10)$$

Using Eqs. 2.2.9a-b this can be written as:

$$\frac{2M}{\mu_B} = \int_0^{E_F + \mu_B H} N(E) dE - \int_0^{E_F - \mu_B H} N(E) dE = \int_{E_F - \mu_B H}^{E_F + \mu_B H} N(E) dE \quad (2.2.11)$$

with N as defined by Eq. (2.2.4). When the Zeeman energy is much smaller than the Fermi energy, $\mu_0\mu_B H \ll E_F$, we can take the integrand out of the integral in the above equation. In other words, we approximate the shaded area in Fig. 2.2.1b by $\pm N(E_F) \mu_0\mu_B H$, as if the DOS were constant for the small applied field. Hence:

$$M = \mu_0\mu_B^2 N(E_F) H = \chi H \quad (2.2.12)$$

and the *Pauli susceptibility* χ reads:

$$\chi = \mu_0 \mu_B^2 N(E_F) = \frac{3\mu_0 \mu_B^2 n}{2E_F} \quad (2.2.13)$$

In hypothesis that $N(E)$ does not vary rapidly with energy as compared to $k_B T$, it's possible to demonstrate that:

$$\chi = \mu_0 \mu_B^2 N(E_F) \left[1 - \frac{\pi^2}{12} \left(\frac{k_B T}{E_F} \right)^2 \right] \quad (2.2.14)$$

In magnetic metals, the interaction between magnetic moments can be approximated by an *average, molecular or exchange field*, which is assumed to be proportional to the macroscopic magnetization M . This implies we are neglecting all details of the interaction (e.g., the fluctuation interactions in space on atomic level), which is, similar to other fields in physics, referred as a *mean-field approximation*. We can simply write:

$$\mathbf{H}_{ex} = -\lambda \mathbf{M} \quad (2.2.15)$$

with λ the *Weiss or molecular-field constant*. This field can be seen as the field in Eqs. 2.2.9a-b that produces the band shift (Fig. 2.2.2).

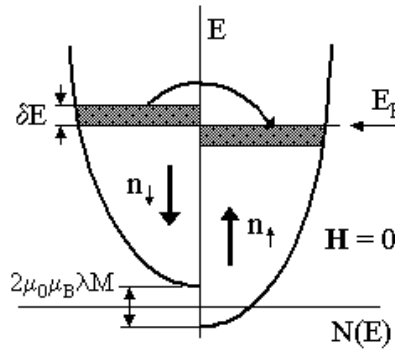


Fig. 2.2.2 The exchange field splits the up- and down band of conduction electrons, by which ferromagnetism can be stabilized.

The magnetic energy density:

$$u = \frac{\mu_0}{2} \mathbf{M} \cdot \mathbf{H}_{ex} = -\frac{\mu_0}{2} \mu_B (n_\uparrow - n_\downarrow) \lambda \mu_B (n_\uparrow - n_\downarrow) = -U (n_\uparrow - n_\downarrow)^2 \quad (2.2.16)$$

where $U = (1/2) \mu_0 \mu_B^2 \lambda$ is a parameter governing the strength of the magnetic interaction. Moreover we can define the *normalized excess of spin up electrons* R as:

$$R = \frac{n_\uparrow - n_\downarrow}{n} \quad (2.2.17)$$

a number that can range between -1 and +1. Notice that R do not necessarily coincide with the so-called *electron polarization*, which defines the excess of spin up electrons at the Fermi level:

$$P = \frac{N_\uparrow(E_F) - N_\downarrow(E_F)}{N_\uparrow(E_F) + N_\downarrow(E_F)} \quad (2.2.18)$$

Substituting eq. 2.2.16 in eq. 2.2.17:

$$u = -Un^2R^2 \quad (2.2.19)$$

If this were the only energy involved, a non-zero magnetization, i.e. $R \neq 0$, would always lead to a stable ferromagnetic state ($u < 0$). However, a second energy contribution has to be taken into account, which is the energy needed to transfer electrons from the down- to the up band, as shown in Fig. 2.2.2. The amount of energy (per unit volume) needed to transform spin down electrons within the energy δE to the spin-up band equals:

$$u = \frac{n_{\uparrow} - n_{\downarrow}}{2} \delta E = \frac{nR}{2} \delta E \quad (2.2.20)$$

Therefore, the total energy required to set up a ferromagnetic magnetization is given by the sum of Eqs. 2.2.19 and 2.2.20, yielding:

$$u = \frac{n^2}{2N(E_F)} R^2 [1 - 2UN(E_F)] \quad (2.2.21)$$

Here we used the approximation: $nR = n_{\uparrow} - n_{\downarrow} = N(E_F)\delta E$ the number of states per energy times the energy interval at the Fermi level. The equation tells us that to sustain spontaneous ferromagnetic order ($R \neq 0$) it is necessary that:

$$1 - 2UN(E_F) < 0 \quad (2.2.22)$$

or

$$2UN(E_F) > 1 \quad (2.2.23)$$

which is known as the *Stoner criterion* for ferromagnetism. The magnetization of metallic materials, $M = \mu_B(n_{\uparrow} - n_{\downarrow})$ can be written as $M = nR\mu_B$ with the help of Eq. 2.2.17. Then Eq. 2.2.21 transforms into:

$$u = \frac{M^2}{2\mu_B^2 N(E_F)} [1 - 2UN(E_F)] - \mu_0 MH \quad (2.2.24)$$

where an additional Zeeman term has been added. Minimizing this energy ($\partial u / \partial M = 0$) leads to:

$$\chi = \frac{\mu_0 \mu_B^2 N(E_F)}{1 - 2UN(E_F)} = \frac{\chi_0}{1 - 2UN(E_F)} \quad (2.2.25)$$

with χ_0 the Pauli-susceptibility as earlier given in eq. (2.2.13). This suggest the susceptibility is larger by a factor determined by the interaction strength and density of states, which is often referred as the *Stoner enhancement*. This is the reason why metals with unfilled d -band show generally higher susceptibility when they have large $N(E_F)$.

2.2.3 The Landau-Lifshitz-Gilbert equation

In the presence of magnetic domains the spins in each domain are still parallel, but the magnetization directions of neighboring domains are different from each other. The presence of a large number of competing energies other than the exchange energy causes this phenomenon.

The goal of micromagnetics is to find the magnetization $\mathbf{M}(\mathbf{r})$ as a function of the position \mathbf{r} inside the sample, assuming that $\mathbf{M}(\mathbf{r})$ has a constant module M_s in each small volume dV : $\mathbf{M}(\mathbf{r}) = M_s \mathbf{m}(\mathbf{r})$ with $\mathbf{m}(\mathbf{r})$ magnetization unit vector field or normalized magnetization. The total free energy is given by:

$$G(\mathbf{M}; \mathbf{H}_a) = \int_V g_{tot}(\mathbf{M}(\mathbf{r}); \mathbf{H}_a) dV = \int_V (e_{ex} + e_{an} + e_{ms} + e_h) dV \quad (2.2.26)$$

where $g_{tot}(\mathbf{M}(\mathbf{r}); \mathbf{H}_a)$ is the total energy density given by the sum of exchange, anisotropy, magnetostatic and external field energies and \mathbf{H}_a is an applied external field. In the following we introduce the various energy terms involved in Eq. 2.2.26.

2.2.3.1 Exchange energy in the continuum approximation

In the case of a cubic lattice of spins, with interaction energy given by Eq. (2.2.1) and assume that the sum is extended to the nearest neighbors only and that the forces between spins are sufficiently strong to keep the neighbor spins almost parallel. If \mathbf{m}_i (\mathbf{m}_j) is the unit-vector in the direction \mathbf{S}_i (\mathbf{S}_j), such that \mathbf{S}_i (\mathbf{S}_j) = $S\mathbf{m}_i$ ($S\mathbf{m}_j$) (S is the spin magnitude), and if θ_{ij} is the small angle between the directions \mathbf{m}_i and \mathbf{m}_j , we can rewrite Eq. 2.2.1 as:

$$\mathcal{H} = -2JS^2 \sum \cos\theta_{i,j} \approx -2JS^2 \sum \left(1 - \frac{1}{2}\theta_{i,j}^2\right) = C + JS^2 \sum \theta_{i,j}^2 \approx C + JS^2 \sum (\mathbf{m}_j - \mathbf{m}_i)^2 \quad (2.2.27)$$

since for small θ_{ij} , $|\theta_{ij}| = |\mathbf{m}_j - \mathbf{m}_i|$. We now assume that the displacement vector $\mathbf{m}_j - \mathbf{m}_i$ can be written in terms of a continuous function \mathbf{m} such that:

$$\mathbf{m}_j - \mathbf{m}_i = (\Delta\mathbf{r}_j \cdot \nabla) \mathbf{m} \quad (2.2.28)$$

where $\Delta\mathbf{r}_j = \mathbf{r}_j - \mathbf{r}_i$ is the position vector of neighbor j with respect to site i . Then, if $\mathbf{m} = m_x\mathbf{e}_x + m_y\mathbf{e}_y + m_z\mathbf{e}_z$,

$$\mathcal{H} = C + JS^2 \sum [(\Delta\mathbf{r}_j \cdot \nabla) \mathbf{m}]^2 = C + JS^2 \sum \left[\left((\Delta\mathbf{r}_j \cdot \nabla) m_x \right)^2 + \left((\Delta\mathbf{r}_j \cdot \nabla) m_y \right)^2 + \left((\Delta\mathbf{r}_j \cdot \nabla) m_z \right)^2 \right] \quad (2.2.29)$$

We can sum over j and multiply by the number of spins per unit volume n in order to obtain the energy per unit volume e_{ex} . It is important to notice that, if $\Delta\mathbf{r}_j = x_j\mathbf{e}_x + y_j\mathbf{e}_y + z_j\mathbf{e}_z$, due to the cubic symmetry it happens that $\sum_j x_j y_j = 0$ and $\sum_j x_j^2 = 1/3 \sum_j \Delta\mathbf{r}_j^2$. By using these properties and neglecting the constant term, one ends up with:

$$e_{ex}(\mathbf{m}(\mathbf{r})) = A \left[(\nabla m_x)^2 + (\nabla m_y)^2 + (\nabla m_z)^2 \right] \quad (2.2.30)$$

A is the exchange constant, $A = \frac{1}{6} n JS^2 \sum \mathbf{r}_{i,j}^2 = \frac{JS^2}{a} c$ with a edge of the unit cell and $c = 1, 2$ and 4 for a simple cubic, bcc and fcc cell, respectively. In case of hcp structure $c = 2^{1/2}$ with a distance between nearest neighbors.

Typical values of A are in the order of 10^{11} J/m. The exchange energy is an isotropic quantity because it depends only on the angle between neighbor magnetic moments and not on their relative orientation. Although the form of exchange interaction expressed by Eq. (2.2.30) has been derived for the case of direct exchange, it can be used for any types of interaction that tend to align spins parallel to each other, for instance the DE interaction, by defining an appropriate *effective* exchange stiffness.

2.2.3.2 Anisotropy energy

In magnetic materials the magnetization is induced to lie along specific directions called easy axes. The *spin-orbit interaction* couples the electron spins, responsible for the magnetism, to the anisotropic orbitals in a crystalline structure. The ions of the crystal create an electric potential that couples the spins to the lattice. The *anisotropy energy* is proportional to the product $\mathbf{L} \cdot \mathbf{S}$ between the orbital momentum \mathbf{L} and the spin momentum \mathbf{S} . Therefore, in absence of magnetic field, the energetic minimum is obtained for \mathbf{S} parallel to \mathbf{L} . A higher order source of anisotropy can be the stress, either tensile or compressive, applied to a crystal lattice. The stress changes the distance between neighbor ions so that the electric potential, the electronic orbitals and the spin-orbit coupling are modified. The spin-orbit coupling creates both the *magnetocrystalline anisotropy* and the *stress induced anisotropy*. For a cubic crystal, the anisotropy energy is often expressed [66] as:

$$e_c(\mathbf{m}(\mathbf{r})) = K_0 + K_1(\cos^2\theta_1\cos^2\theta_2 + \cos^2\theta_2\cos^2\theta_3 + \cos^2\theta_1\cos^2\theta_3) + K_2\cos^2\theta_1\cos^2\theta_2\cos^2\theta_3 + \dots \quad (2.2.31)$$

where K_0, K_1, K_2, \dots are constants and $\theta_1, \theta_2,$ and θ_3 are the angles between the magnetization direction and the three crystal axes, respectively. K_0 is independent of angle and can be ignored since it is the difference in energy between different crystal orientations that is of interest. The anisotropy constants K_1 and K_2 depend on the temperature and can be obtained experimentally. In many cases, terms involving K_2 are small and can also be neglected. If $K_1 > 0$, e_c is minimum in the $\langle 100 \rangle$ directions; hence, these directions are the easy axes. Conversely, if $K_1 < 0$, the easy axes correspond to the $\langle 111 \rangle$ directions. The difference in magnetocrystalline energy between the $[111]$ direction and the $[100]$ direction $\Delta K_{[111]-[100]}$ is equal to $K_1/3$. Similarly, the difference between the $[110]$ direction and the $[100]$ direction $\Delta K_{[110]-[100]}$ is equal to $K_1/4$. The magnetocrystalline anisotropy energy associated with a hexagonal close-packed crystal can be expressed as [67]:

$$e_u(\mathbf{m}(\mathbf{r})) = K_0 + K_1\sin^2\theta + K_2\sin^4\theta + \dots \quad (2.2.32)$$

where K_0, K_1, K_2, \dots are constants and θ is the angle between the c -axis and the magnetization. As described above, K_0 is independent from angle. For most cases in which K_2 can be neglected, if $K_1 > 0$, the energy is smallest when $\theta = 0$, i.e. along the c -axis, so that this axis is the easy axis. If $K_1 < 0$, the basal plane is the easy axis.

As a result of the symmetry of the hexagonal close-packed lattice, the magnetocrystalline anisotropy is a uniaxial anisotropy. Eqs. 2.2.31 and 2.2.32 are volume energy densities. At the surface the breaking of symmetry generates an additional term of anisotropy [68] given by:

$$e_s(\mathbf{m}(\mathbf{r})) = \frac{1}{2}K_s(\mathbf{n} \cdot \mathbf{m}(\mathbf{r}))^2 \quad (2.2.33)$$

where \mathbf{n} is a unitary vector perpendicular to the surface and the constant K_s can be taken from the experiments. Note that e_s , called *surface anisotropy energy*, can favor both an in-plane or an out-of-plane magnetization and therefore the sign of K_s can be positive or negative. This surface contribution has been neglected in Eq. 2.2.26 on purpose because of no relevance in the present work. It has been here introduced for the sake of completeness and must be taken into account in the case of thin films that spontaneously tend to align their magnetization out of the plane (*perpendicular magnetic anisotropy*).

2.2.3.3 External field energy

The Zeeman energy, i.e., the energy of the magnetization in an externally applied magnetic field \mathbf{H}_a can be written as:

$$e_h(\mathbf{m}(\mathbf{r})) = -\mu_0 \mathbf{M} \cdot \mathbf{H}_a = -\mu_0 M_S \cdot \mathbf{H}_a \cdot \mathbf{m}(\mathbf{r}) \quad (2.2.34)$$

2.2.3.4 Magnetostatic energy

The magnetization $\mathbf{M}(\mathbf{r})$ can interact also with the magnetic field generated by the body itself. In this case the energy density is:

$$e_{ms}(\mathbf{m}(\mathbf{r})) = -\frac{1}{2}\mu_0 M_S \cdot \mathbf{H}_d \cdot \mathbf{m}(\mathbf{r}) \quad (2.2.35)$$

where the *demagnetizing* or *stray field* \mathbf{H}_d is generated by the sample itself. The factor 1/2 is introduced in order to avoid counting twice the interaction between couples of magnetic moments. It is important to notice that the magnetostatic field at a given location depends on the contributions from the whole magnetization vector field. This makes the free energy of the system being a functional. In order to calculate the magnetostatic energy we first need to evaluate \mathbf{H}_d . At this point we have to introduce some fundamental relations for magnetized media based on the equations of Maxwell. In absence of conduction currents the following relation is valid:

$$\nabla \times \mathbf{H}_d = 0 \quad (2.2.36)$$

In analogy with electrostatics, we can define the magnetic scalar potential ϕ that is linked to \mathbf{H}_d :

$$\mathbf{H}_d = -\nabla\phi \quad (2.2.37)$$

Since $\nabla \cdot \mathbf{B} = 0$, it is $\nabla \cdot \mathbf{H}_d = -\nabla \cdot \mathbf{M}$, the magnetic potential ϕ is solution of the Poisson's equation:

$$\nabla^2\phi = -\nabla \cdot \mathbf{M} \quad (2.2.38)$$

Considering the boundaries at the surface of the ferromagnet we obtain:

$$\phi(\mathbf{r}) = - \int_V \frac{\nabla \cdot \mathbf{M}(\mathbf{r}')}{|\mathbf{r} - \mathbf{r}'|} d^3r' + \int_S \frac{\mathbf{n} \cdot \mathbf{M}(\mathbf{r}')}{|\mathbf{r} - \mathbf{r}'|} dS' \quad (2.2.39)$$

The first term is a volume integral over the body of volume V and the second is a surface integral extended to the surface S of the body. The form of Eq. 2.2.39 is analogous to the electrostatic potential. In fact, the first integral can be interpreted as the potential due to a spatial distribution of a volume charge with density $\rho/\epsilon_0 = \nabla \cdot \mathbf{M}$; the second as the potential due to a surface charge with density $\sigma/\epsilon_0 = \mathbf{n} \cdot \mathbf{M}$. If we consider the case of a uniformly magnetized body $\nabla \cdot \mathbf{M} = 0$ the first integral in Eq. 2.2.39 vanishes. Moreover, \mathbf{M} can be taken out of the surface integral and the potential depends only on the shape. In particular, if the geometry is of ellipsoidal shape, the demagnetizing field \mathbf{H}_d has the same direction as \mathbf{M} :

$$\mathbf{H}_d = -\mathcal{N}\mathbf{M} \quad (2.2.40)$$

where \mathcal{N} is a tensor. If \mathbf{M} is parallel to one of the principal axis of the ellipsoid, \mathcal{N} is a number and it is called *demagnetizing factor*. In the case of the infinite film Eq. 2.2.35 can be written as:

$$e_{ms} = \frac{1}{2}\mu_0 M_z^2 = \frac{1}{2}\mu_0 M_S^2 \cos^2\theta \quad (2.2.41)$$

where θ is the angle of the magnetization vector with respect to the z axis. Eq. 2.2.41 is characteristic of systems with uniaxial anisotropy and is called *shape anisotropy*.

2.2.4 Micromagnetic equations

The magnetization configuration can be determined by minimizing the free energy in the Eq. 2.2.26. We have to notice that micromagnetism ignores the atomic nature of matter and the material is considered as continuous, i.e. the magnetization vector is taken as a continuous function of space. This is really the most important limit of the micromagnetism: it is not possible to use it when the system approaches atomic size. The set of local minima is found by means of variational calculus. In fact, because of the presence of the magnetostatic energy, the free energy is a functional, as already discussed. The solution of the variational problem takes the form of a stability condition to be fulfilled at equilibrium [69]. In each point of the magnetic body is defined an *effective field* \mathbf{H}_{eff} given by:

$$\mathbf{H}_{eff} = - \frac{\partial G(\mathbf{m}; \mathbf{H}_a)}{\partial \mathbf{m}} = \frac{2A}{\mu_0 M_S} (\nabla \mathbf{m})^2 + \mathbf{H}_{an} + \mathbf{H}_d + \mathbf{H}_a \quad (2.2.42)$$

where \mathbf{H}_{an} denotes the anisotropy field defined as:

$$\mathbf{H}_{an} = - \frac{1}{\mu_0 M_S} \frac{\partial e_{an}}{\partial \mathbf{m}} \quad (2.2.43)$$

The effective field creates a torque on the magnetization that must be zero at equilibrium. Therefore the stability condition to be fulfilled in each point of the magnetic body is:

$$\mathbf{m} \times \mathbf{H}_{eff} = 0 \quad (2.2.44)$$

Eq. (2.2.44) is known as Brown's equation and it is completed by the boundary condition:

$$\mathbf{m} \times \left(2A \frac{\partial \mathbf{m}}{\partial \mathbf{n}} + \frac{\partial e_s}{\partial \mathbf{m}} \right) = 0 \quad (2.2.45)$$

where \mathbf{n} is the unity vector normal to the surface. In absence of surface anisotropy, Eq. (2.2.45) becomes:

$$\frac{\partial \mathbf{m}}{\partial \mathbf{n}} = 0 \quad (2.2.46)$$

If the system is out of equilibrium equation (44) is not fulfilled and the vector \mathbf{m} precesses around the field \mathbf{H}_{eff} . The time dependence of the magnetization can be obtained directly from the quantum-mechanical expression for a precession of the magnetization in a magnetic field (momentum theorem), by considering the effective field to be the acting field, in SI units:

$$\frac{\partial \mathbf{m}}{\partial t} = -\gamma_0 \mathbf{m} \times \mathbf{H}_{eff} \quad (2.2.47)$$

where t is the time and $\gamma_0 = \mu_0 \gamma = \mu_0 (g |e|) / (2m_e c) = g \mu_0 |\mu_B| / (h/2\pi)$ is called *gyromagnetic ratio*. The boundary conditions are the same as in the static case. This equation represents an undamped precession that decays in a finite time (from experimental results) [70]. The damping cannot be derived theoretically from basic principles, and is just added as a phenomenological term. Thus we can write the Landau-Lifshits-Gilbert (LLG) equation:

$$\frac{\partial \mathbf{m}}{\partial t} = -\gamma_0 \mathbf{m} \times \left(\mathbf{H}_{eff} - \frac{\partial \mathbf{m}}{\partial t} \frac{\alpha}{\gamma_0} \right) = -\gamma_0 \mathbf{m} \times \mathbf{H}_{eff} + \alpha \mathbf{m} \times \frac{\partial \mathbf{m}}{\partial t} \quad (2.2.48)$$

where α is a phenomenological damping parameter. If $\alpha \rightarrow 0$ the damping vanishes and the precession continues forever. If $\alpha \rightarrow \infty$ the precession is negligible compared with the damping term. Finally, if $\partial \mathbf{m} / \partial t = 0$ the Eq. 2.2.44 is recovered. A geometrical interpretation of LLG is possible and it's shown in Fig. 2.2.3.

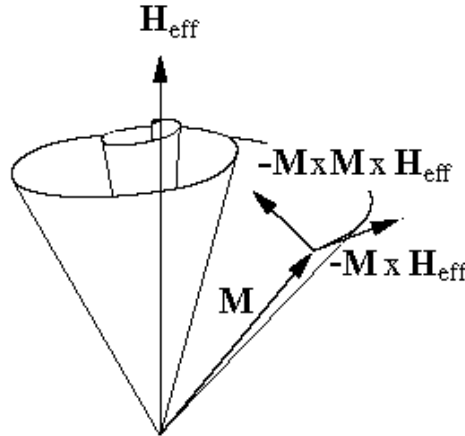


Fig. 2.2.3 Geometrical interpretation of the Landau-Lifshitz-Gilbert equation.

2.2.5 Domains and domain walls

A direct consequence of energy minimization is the formation of *domains* [71]. If the magnetization were homogenous across the sample, there would be a high cost of magnetostatic energies due to the formation of free poles. This could be avoided dividing the magnetization into regimes known as “domains” and arranging it in a way to minimize the stray field energy (see Fig. 2.2.4). In this process, boundaries are formed between adjacent domains having different magnetization directions. Abrupt transitions, however, are not favorable due to the strong exchange interaction in the ferromagnets. Such boundaries spread out into a region of finite thickness known as *domain walls* (DWs), in which the magnetization directions twist and form relatively smooth transitions between two domains. Fig. 2.2.5(a) shows a *Bloch domain wall* [72] containing smoothly rotating moments, which minimizes the energy cost due to the exchange interaction. For the case of thin films (that do not show significant surface anisotropy), the ‘magnetic charges’ formed by the Bloch wall moments rotating out of plane would cost a high magnetostatic energy, hence it is more favorable for the moments to rotate in the plane of the film. A *Néel wall* [73] (Fig. 2.2.5(b)) is formed in preference to a Bloch wall in this way. The width of the domain wall is strongly dependent on the material and its anisotropies, but is typically of the order of tens to 100 nm. The width and the energy of a wall can be calculated (in absence of an external applied magnetic field) by minimizing the total energy of the system.

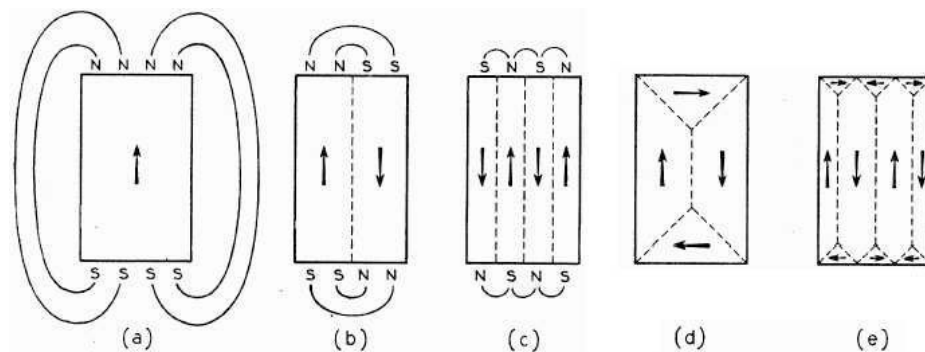


Fig. 2.2.4 Origin of domains [71].

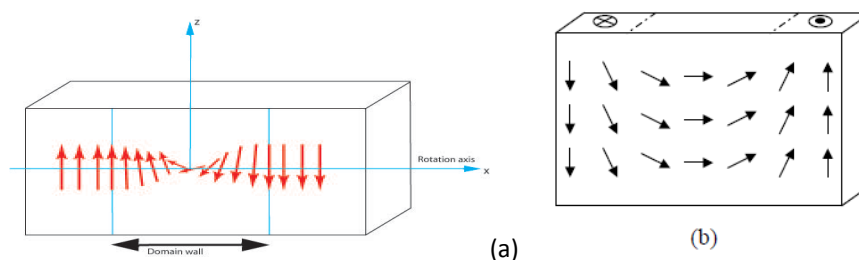


Fig. 2.2.5 Schematic diagrams showing (a) a Bloch wall and (b) a Néel wall.

Now we consider a Bloch wall and assume that Ox is the axis perpendicular to the DW. The moments make an angle ϕ with the Oz axis and $\Delta\phi$ is the angle between two successive moments along the x -axis. The total energy of the wall (with unit surface area) can be write as:

$$E(\theta) = \int_{-\infty}^{+\infty} \left[A \left(\frac{d\theta}{dx} \right)^2 + e_{an}(\theta) \right] dx \quad (2.2.49)$$

where A is the exchange stiffness and $e_{an}(\theta)$ is the anisotropy energy density, which will be assumed to be zero along the easy directions of magnetization. To minimize the integral $\theta(x)$ must suitably take. Thus, if at each point x , $\theta(x)$ varies by a small amount $\delta\theta(x)$, the modification in configuration of the spins does not provoke, to first order, any variation δE , so Eq. 2.2.49 begins:

$$\delta E(\theta) = \int_{-\infty}^{+\infty} \left[2A \left(\frac{d\theta}{dx} \right) \left(\frac{d\delta\theta}{dx} \right) + \frac{de_{an}(\theta)}{d\theta} \right] dx = 0 \quad (2.2.50)$$

It's possible to write Eq. 2.2.50 as:

$$\int_{-\infty}^{+\infty} \left[\frac{\partial e_{an}(\theta)}{\partial \theta} - 2A \left(\frac{\delta^2 \theta}{\delta^2 x} \right) \right] \delta\theta dx = 0 \quad (2.2.51)$$

The relation must remain true whatever the variation $\delta\theta(x)$ chosen. This implies that:

$$\frac{\partial e_{an}(\theta)}{\partial \theta} - 2A \left(\frac{\delta^2 \theta}{\delta^2 x} \right) = 0 \quad (2.2.52)$$

This is the *Euler's equation* of variational calculus. On multiplying by $\frac{\delta\theta}{\delta x}$ and integrating over x , one obtains:

$$e_{an}(\theta) = A \left(\frac{\delta\theta}{\delta x} \right)^2 + const \quad (2.2.53)$$

but, when $x = \pm\infty$ (within the domain), $e_{an}(\theta) = 0$ and $\frac{\delta\theta}{\delta x} = 0$, indicating that *const* is zero. Hence

$$e_{an}(\theta) = A \left(\frac{\delta\theta}{\delta x} \right)^2 \quad (2.2.54)$$

which reads: at all point of the domain wall the cost in anisotropy energy and in exchange energy balance each other. In other words, inside the domain wall, where the anisotropy energy is most costly, the angle between adjacent spin is greater, and vice versa. The domain wall energy is:

$$E(\theta) = 2 \int_{-\infty}^{+\infty} e_{an}(\theta) dx \quad (2.2.55)$$

Extracting dx from Eq.2.2. 54 we can write the general energy expression for a Bloch wall:

$$E(\theta) = 2\sqrt{A} \int_{-\theta_i}^{\theta_f} \sqrt{e_{an}(\theta)} d\theta \quad (2.2.56)$$

For a 180° wall ($\theta_i = -\pi/2$ and $\theta_f = \pi/2$) and assuming a uniaxial anisotropy ($e_{an}(\theta) = K \cos^2 \theta$):

$$E(\theta) = 4\sqrt{AK} \quad (2.2.57)$$

DW's width w can be expressed as:

$$w = \pi \left(\frac{\delta x}{\delta \theta} \right)_{x=0} = \pi \sqrt{\frac{A}{K}} \quad (2.2.58)$$

where $\theta_f - \theta_i = \pi$ and assuming the angular deviation constant and equal to the value at the center of the wall. In particular for a bulk film of Permalloy $w \sim 200$ nm [74]. In the case of a Néel wall, energy minimization will vary the angle θ from -90 to 90 by changing the magnetization parallel to the surface in order to restrict the demagnetization effects created by the proximity of the planes. The characteristic length of a Néel wall can be calculated to be:

$$w = \pi \sqrt{\frac{A}{K_d}} \quad (2.2.59)$$

where K_d is the out-of-plane shape anisotropy constant. It is worth mentioning that, while reducing the thickness of a film, the transition from Bloch wall to Néel wall is not sharp. In a certain region of film thicknesses, a third type of wall is observed that is named *cross-tie wall* [75]. In particular for Permalloy it appends in the thickness range (30-40) nm (see Fig. 2.2.6) while under 30 nm domains configuration is Néel type [76]

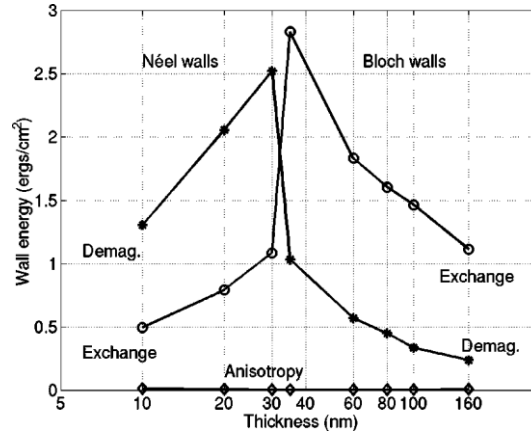


Fig. 2.2.6 Wall energy components (exchange, anisotropy, and demagnetization) as a function of film thickness.

2.2.6 Magnetization reversal and hysteresis

The domain theory has permitted the understanding of the reversal of magnetization within ferromagnets under the influence of an external magnetic field. The process can be described qualitatively by domain nucleation, domain wall motion and magnetization rotation [66], with the aid of a hysteresis loop ($M(H)$ loop) (Fig. 2.2.7). Starting from a saturation field (point A in the figure), reversible magnetization rotation occurs as the field decreases (section A-B), returning the magnetization back to its anisotropy axes. As the field continues to decrease (section B-C), new domains are nucleated within the existing ones. The Zeeman energy associated with individual domains favours the 'growth' of domains with magnetization vectors along (or with a component along) the field direction, which takes place by domain wall motion. This process continues until the unfavourable domains are eliminated. The final stage of the reversal process (section C-D) involves the rotation of remaining domains from their anisotropy axes towards the field direction, finishing half of the reversal cycle.

The above descriptions are highly simplified from the actual situation, and deviations are likely to happen locally due to inhomogeneities. Typical among the magnetization measurements of different ferromagnetic materials is the phenomenon of hysteresis: the magnetization of the sample does not vanish when the field sweeps towards zero. There is some lapse of field before the total magnetization comes to zero.

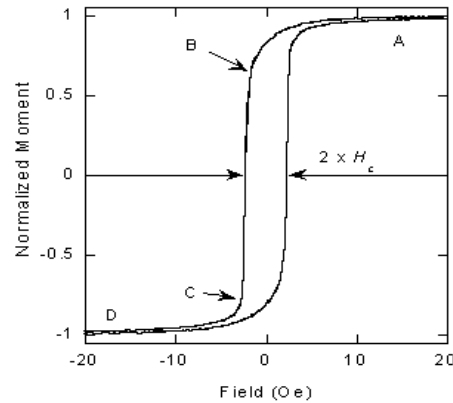


Fig. 2.2.7 A typical magnetic hysteresis loop of a single layer of magnetic film. H_c is the coercivity of the film.

Such a lapse, in the special case in which the sample was previously brought to saturation before the reverse field cycle commences, is called the coercivity of the sample (H_c). The size of coercivity is important in determining the potential applications of particular materials, and is the consequence of a number of intrinsic and extrinsic factors, for example the anisotropy and the defects.

2.2.7 Constrained domain walls

The improvement in the nanotechnologies and the possibility to get smaller structures allows to study and investigate more deeply the electrical transport properties of the DW controlled by geometrical parameters. Since the electrical resistance of a DW is determined by $d\phi/dx$, a more appropriate definition of the DW width is [77]:

$$w = 4 \left[\int_{-\infty}^{+\infty} \left(\frac{d\theta}{dx} \right)^2 dx \right]^{-1} = 4 \left[\int_{-\pi/2}^{+\pi/2} \frac{d\theta}{dx} d\theta \right]^{-1} \quad (2.2.60)$$

where the prefactor is chosen so that the definition yields $w_0 = 2 (A/K)^{1/2}$ for an unconstrained Bloch wall in the context of an uniaxial anisotropy. Using the coordinate system introduced previously, three models can be represented:

1. $S(x) = S_0$ for $|x| \leq d$
 $= S_1 > S_0$ for $|x| > d$
2. $S(x) = S_0 (1 + x^2/d^2)$
3. $S(x) = S_0 \cosh(x/d)$

where $S(x)$ is the cross section and d is a measure of the length of the constriction.

For this calculation three assumptions are made: (i) the wall is plane, (ii) the magnetization remains in the yz plane as in a Bloch wall, (iii) the dipolar interaction is neglected. With these assumptions the total energy of the wall is easily written by introducing the cross section in Eq. 2.2.49:

$$E(\theta) = \int_{-\infty}^{+\infty} \left[A \left(\frac{d\theta}{dx} \right)^2 + e_{an}(\theta) \right] S(x) dx \quad (2.2.61)$$

The corresponding Euler's equation becomes:

$$\left(\frac{\partial^2 \theta}{\partial x^2} \right) + \frac{1}{S} \left(\frac{\partial \theta}{\partial x} \right) \left(\frac{\partial S}{\partial x} \right) - \frac{1}{2A} \frac{\partial e_{an}(\theta)}{\partial \theta} = 0 \quad (2.2.62)$$

A first case in which the term $\frac{\partial e_{an}}{\partial x}$ is neglected is considered. The solutions in this case are indicated by a star and take the general form [74]:

$$\theta^*(x) = \pi \left[\frac{\int_{-\infty}^x S^{-1}(x') dx'}{\int_{-\infty}^{+\infty} S^{-1}(x') dx'} - \frac{1}{2} \right] \quad (2.2.63)$$

$$w^* = \frac{4 \left[\int_{-\infty}^{+\infty} S^{-1}(x) dx \right]^2}{\pi^2 \int_{-\infty}^{+\infty} S^{-2}(x) dx} \quad (2.2.64)$$

$$E^* = \frac{A\pi^2}{\int_{-\infty}^{+\infty} S^{-1}(x) dx} \quad (2.2.65)$$

The term $\frac{\partial e_{an}}{\partial x}$ is negligible if $w^* \ll w_0$. The usefulness of this approximation depends on whether (x) is integrable or not. The former case is valid for model I with $S_1 = \infty$ and for model II and III. The latter for model I with S_1 finite [77]. The result is that, for the integrable case, d can be chosen so that $w^* \ll w_0$ and w depends only on d . Actually, from an experimental point of view, the most interesting case is just the not integrable one (model 1 with S_1 finite). So we will focus on this case in the following. For simplicity considering an uniaxial anisotropy, the Euler's equation is:

$$\left(\frac{\partial^2 \theta}{\partial x^2} \right) + \frac{1}{S} \left(\frac{\partial \theta}{\partial x} \right) \left(\frac{\partial S}{\partial x} \right) + \frac{\sin \theta \cos \theta}{L^2} = 0 \quad (2.2.66)$$

where $L = \sqrt{A/K}$. In order to make the equation easily soluble, the following approximation can be made [74]:

$$\cos^2 \theta \approx \alpha (\pi - 2|\theta|) \quad (2.2.67)$$

which implies:

$$\sin \theta \cos \theta \approx \alpha \operatorname{sgn}(\theta) \quad (2.2.68)$$

for $|\theta| \leq \pi/2$, and where α is determined variationally by minimizing the energy with respect to ϕ for the case of unconstrained wall. That yields $\alpha = 0.298$. Analytical solution can be found in [77]. We will give below only approximate expressions valid in a restricted range of parameters, from which the physical meaning appears more clearly. If $d \ll w_0$, most of the magnetization rotation takes place in a region of width $2d$.

Thus, the constrained wall can be much narrower than an unconstrained Bloch wall. Three regimes can be distinguished. If $w_0/d \leq 1$, the energy and the width of the wall are approximately equal to those of the unconstrained wall. This is reasonable since in this case a Bloch wall can be completely confined in the constrain and is therefore not influenced by it. If $1 \leq w_0/d \leq S_1/S_0$ the wall width and energy are the same (with the approximation Eq. 2.2.67) as obtained for $S1 = \infty$, which means the DW width depends only on the geometry of unconstrained wall. The larger is S_1/S_0 , the wider is the range of values w_0/d in which the regime is achieved. Finally, if $w_0/d \geq S_1/S_0$, the wall is again determined primarily by the competition between exchange and anisotropy energy. It remains to verify the assumption made on the dipolar interaction, which was neglected. Assuming the dipolar energy to be given by $\frac{1}{2}\mu_0 M_S^2$ the dipolar energy is obtained by multiplying by the wall volume: $E_d \approx \frac{1}{2}\mu_0 M_S^2 S_0 w$ For the case of practical interest ($1 \leq w_0/d \leq S_1/S_0$), one finds that dipolar interaction can be neglected if $d \ll l_{ex}$, where $l_{ex} = \sqrt{\frac{2A}{\mu_0 M_S^2}}$ is the *ferromagnetic exchange length*. Typical values of l_{ex} are 2.2, 4, 11.5 nm, for Fe, Co and Ni, respectively, so the condition $d \ll l_{ex}$ should be valid only for point contact systems. Yet, this result has been demonstrated [78] to be valid under less restrictive hypotheses, for instance in case of negligibility of surface anisotropy and in case of Néel wall. Moreover, the wall can have Néel-type configuration for constrictions much narrower than the normal wall width, although being Bloch-type in the unconstrained case. In conclusion, in a narrow constriction the structure of a wall becomes almost independent of the material parameters (magnetization, exchange stiffness, anisotropy constant) and is determined mostly by the geometry of the constriction. It follows that, if the constriction is smaller than a few tens of nanometers, the width of the geometrically constrained domain wall is similar in size to the constriction.

2.2.8 Ordinary Magnetoresistance

The current density \mathbf{J} in a material, is proportional to the electric field \mathbf{E} through the conductivity σ , *i.e.* $\mathbf{J}=\sigma\mathbf{E}$. This relationship of proportionality can be expressed in terms of a tensor to take in account anisotropies: in fact, the electric field and current flow are not always collinear, and the conductivity (or resistivity) is a function of the direction, as in a crystalline material with low symmetry. In the absence of a magnetic field, the tensor resistivity (or conductivity) is symmetrical ($\rho_{ij}=\rho_{ji}$), and it can be diagonalized. The relationships between the components of the conductivity and resistivity tensor are reported in the follows [79]:

$$\rho_{ii} = \frac{(\sigma_{jj}\sigma_{kk}-\sigma_{kj}\sigma_{jk})}{\Delta(\sigma)} \quad \rho_{ij} = \frac{(\sigma_{ik}\sigma_{kj}-\sigma_{ij}\sigma_{kk})}{\Delta(\sigma)} \quad (2.2.69)$$

$$\sigma_{ii} = \frac{(\rho_{jj}\rho_{kk}-\rho_{kj}\rho_{jk})}{\Delta(\rho)} \quad \sigma_{ij} = \frac{(\rho_{ik}\rho_{kj}-\rho_{ij}\rho_{kk})}{\Delta(\rho)}$$

with $\Delta(\sigma)$ and $\Delta(\rho)$ the determinants of matrices whose elements consist of σ_{ij} and ρ_{ij} , respectively. For example, for a material with cubic crystal symmetry $\rho_{ji}=\rho_{kk}=\rho_{ij}$ and the

components of the tensor ρ_{ij} are isotropic, whatever the direction of \mathbf{E} , with the result that \mathbf{J} and \mathbf{E} are parallel. In the presence of an applied magnetic field the resistivity tensor is generally not symmetrical, thus requiring the nine coefficients. However, the coupling between longitudinal and transverse effects are negligible. Finally, resistivity tensor in the presence of an applied magnetic field in the z direction for a cubic system can be expressed in the following form:

$$\rho_{ij} = \begin{bmatrix} \rho_{\perp}(B) & -\rho_H(B) & 0 \\ \rho_H(B) & \rho_{\perp}(B) & 0 \\ 0 & 0 & \rho_{\parallel}(B) \end{bmatrix} \quad (2.2.70)$$

In the past, the strong interest in the MR phenomena was related mainly to the manner in which the components of the conductivity (or resistivity) were related to the shape of the Fermi surface and the variation on it the electronic mean free path. For non-magnetic metals, as long as the resistivity is governed by scattering processes that depend on the speed of an electron and its direction of motion, the magnetoresistive effect at low fields exhibit very low values: the change of resistivity is positive for both directions of the applied field, parallel and transverse to the current direction, with $\rho_{\perp} > \rho_{\parallel}$ and its due to the effect of the Lorentz force on the electrons trajectory when a magnetic field B is applied along the direction z perpendicular to the electric field \mathbf{E} direction x i.e. $\mathbf{F} = -e\mathbf{v} \times \mathbf{B}$ (see Fig. 2.2.8). The relative increase $\Delta\rho/\rho_0 = [\rho(B) - \rho(0)]/\rho(0)$, called MR ratio, is greater when the initial resistivity at zero field $\rho(0)$ has the lowest value, and at low temperature. It is possible to identify three distinct cases for the ordinary magnetoresistance, in relation to the structure of electron orbitals at the Fermi surface:

- in metals with closed Fermi surfaces, the electrons are bound to their orbits in space \mathbf{k} and the effect of magnetic field is to increase the electron cyclotron frequency in its closed orbit; metals that exhibit similar behaviors include In and Al.
- Metals that contain Fermi surfaces with open orbits in certain crystallographic directions exhibit large values of magnetoresistance for fields applied in those directions, while the resistance will saturate in other directions where the orbits are closed, this behavior was found for example in Cu, Ag and Au
- for metals with an equal number of electrons and holes, the magnetoresistance increases with the applied field and is independent of the orientation crystallographic, examples of such behavior are Sb and W.

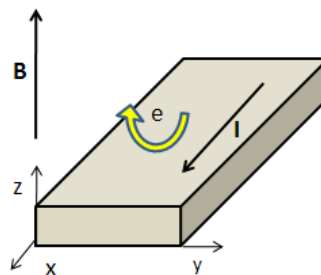


Fig. 2.2.8 Effect of the Lorentz force on the electrons trajectory.

2.2.9 Anisotropic MR

In ferromagnetic metals and alloys, magnetoresistive effects at room temperature reach MR ratio values of over 2% at $H < 0.1$ T (see for example Permalloy). In contrast to what observed in the case of ordinary magnetoresistance, now the effect is anisotropic, with a strong dependence on the direction of the spontaneous magnetization \mathbf{M} , while the ordinary MR only depend on the direction and magnitude of the applied magnetic field compared to the current. For ferromagnetic materials, the origin of this anisotropy is related to the spin-orbit interaction and its influence on the scattering of electrons between the levels s and d , as shown in Fig. 2.2.9. The conduction electrons in magnetic 3d metals (Fe, Co, Ni) are the electrons of the s level, while the d electrons, because of their lower speed at the Fermi level due to the high values of the effective mass, give little contribution to the conductivity. The low level of mobility of the d electrons can therefore consider them localized close the atom: they give the main contribution to the strong magnetic moment observed in these metals. The interaction between the electrons s and d causes the anisotropic magnetoresistance. Orbitals of electrons placed in the level d (a spatially very narrow band) are those most affected by the orienting effect of the magnetization, and hence present a larger scattering cross section with respect of conduction electrons precisely when they are moving along the direction parallel to the magnetization. The scattering which the electrons s are subject to in 3d metals, depends both on the energy of d the states and the relative orientation between the current, \mathbf{J} , and \mathbf{M} . Quantum mechanics predicts a higher probability of scattering when \mathbf{J} is parallel to \mathbf{M} . In addition, the energy level depends on the orientation of the spin axis of the crystallographic material, because the action on the spin of the crystal field through the spin-orbit interaction (magnetocrystalline anisotropy). The crystallographic axes determine the direction of the angular momentum \mathbf{L} , while the magnetization determines the direction of the spin angular momentum \mathbf{S} , so that the mixing of states induced by the applied external field leads to an anisotropic scattering.

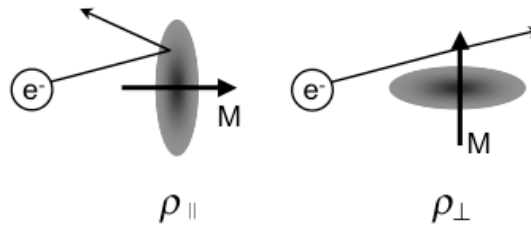


Fig. 2.2.9 Picture of the spin-orbit coupling. The external magnetic field stretches the orbital along the field direction increasing or reducing the scattering cross-section.

In the case of a crystalline sample of single domain, the resistivity along the current direction will depend on the direction cosines α_i and β_j relative to the direction of the crystallographic axes of the sample with respect to the magnetization \mathbf{M} and \mathbf{J} , respectively, resulting in [80]:

$$\rho(\hat{\alpha}, \hat{\beta}) = \frac{\mathbf{J} \cdot \mathbf{E}}{|\mathbf{J}|^2} = \frac{J_i \rho_{ij} J_j}{J_i J_i} = \beta_i \beta_j \rho_{ij}^s \quad (2.2.71)$$

where ρ_{ij}^s is the symmetric part of the resistivity tensor, dependent only even functions of α_i , while the asymmetric part is such that $\beta_i \rho_{ij}^a \beta_j = 0$.

We can thus define two important quantities $\rho_{||}$, the longitudinal resistivity, and ρ_{\perp} , transverse resistivity, depending on whether \mathbf{J} is parallel or perpendicular to \mathbf{M} . For arbitrary orientation of \mathbf{J} with respect to the value of \mathbf{M} , ρ measured in the direction of \mathbf{J} is:

$$E_{||J} = (J \sin \theta \rho_{\perp}) \sin \theta + (J \cos \theta \rho_{||}) \cos \theta = J(\rho_{\perp} \sin^2 \theta + \rho_{||} \cos^2 \theta) \quad (2.2.72)$$

obtaining:

$$\rho_{||J} = \frac{E_{||J}}{J} = (\rho_{\perp} \sin^2 \theta + \rho_{||} \cos^2 \theta) = \rho_{\perp} + \Delta \rho \cos^2 \theta \quad (2.2.73)$$

In order to quantify the anisotropic magnetoresistive effect, is often used in literature the quantity $\Delta \rho / \rho_{\text{demag}}$ called anisotropic magnetoresistive ratio; ρ_{demag} is the resistivity of the demagnetized state, heavily dependent on the sign of the first magnetocrystalline anisotropy constant, which determines the direction of easy magnetization. Since the demagnetized state is not unique, in general, is taken as valid for single crystals to polycrystals, the following approximate relation:

$$\rho_{\text{demag}} = \frac{1}{3} \rho_{||} + \frac{2}{3} \rho_{\perp} = \rho_{av} \quad (2.2.74)$$

Note also that $\rho_{||}$ has generally, but not always, a higher value of ρ_{\perp} . In the following, in order to quantify the effect size to a fixed value of temperature, will be used the following equation for MR as:

$$MR = \frac{\Delta R}{R_0} (H) = \left[\frac{R(H) - R_0}{R_0} \right] \quad (2.2.75)$$

where $R(H)$ is the resistance for a given value of the applied magnetic field, while $R(0)$ indicates the resistance without applied field, which will be measured after careful demagnetization of the sample. The MR ratio values tend to increase with decreasing temperature. Fig. 2.2.10 illustrates the typical trend curves for the longitudinal and transverse magnetoresistive ratio that occur at room temperature in bulk nickel [81]. Moreover, in a cycle of magnetization, when the field is reduced to zero, the resistivity value has higher than that found in this sample without was not magnetization [82] (see Fig.2.2.11).

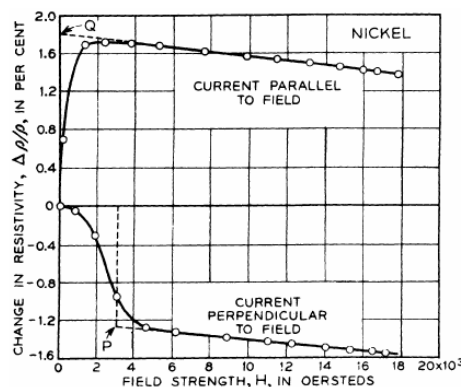


Fig. 2.2.10 Magnetoresistive ratio, longitudinal and transverse of bulk nickel at different magnetic field applied at room temperature.

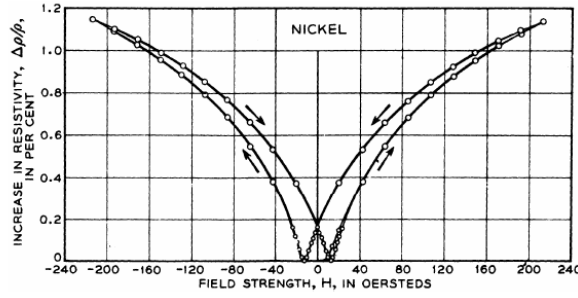


Fig. 2.2.11 Magneto-resistive hysteresis of the relationship with the variation of the current field applied longitudinally in a sample of bulk nickel.

The natural application of the AMR was in magnetic recording as read heads in hard drive due to higher output that those sensors offer as compared to the thin film inductive head [83,84]. The most used material for magnetic recording applications is $\text{Ni}_{80}\text{Fe}_{20}$ Permalloy (Py) because of its softness (low coercivity), high permeability, and low magnetorestriction. A typical AMR ratio for thin Py films (50 nm) is about 2.

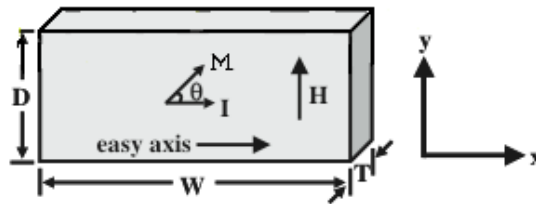


Fig. 2.2.12 Schematic of a single domain AMR sensor.

Assuming that the external magnetic field is along the y-axis and that the whole element is a single-domain particle with a uniaxial anisotropy, the magnetization direction is given:

$$\sin\theta = \frac{H}{2K/\mu_0 M_S} \quad (2.2.76)$$

By separating the magnetocrystalline anisotropy and the shape anisotropy in the constant K , it's possible to write:

$$\sin\theta = \frac{H}{\frac{2Kmc}{\mu_0 M_S} + H_d} = \frac{H}{H_K + H_d} \quad (2.2.77)$$

with H_d demagnetizing field along y-axis. For soft materials like Py ($H_K \ll 1$) results (from Eq. 2.2.73):

$$\rho(H) = \rho_{\parallel} + \Delta\rho \left(\frac{H}{H_d}\right)^2 \quad (2.2.78)$$

The consequence of this equation is that the simple AMR sensor element exhibits a nonlinear response to the external field, which cannot be used as a read sensor for magnetic recording.

The linearity can be achieved if an additional field, larger than that of the external field, is added to make the total effective external field as $H' = H + H_B$ with $H_B \gg H$. In the case of $H_d \ll H$, which is true for magnetic recording, results the sensor responds linearly to the external field:

$$\rho(H) = \rho_{\parallel} + \rho_{\perp} \left(\frac{H_B}{H_d} \right)^2 - \rho_{\perp} \frac{2HH_B}{H_d^2} \quad (2.2.79)$$

H_B is the called *traverse bias field* because it is perpendicular to the easy axis direction of the sensor element. In actual sensor design (in order to maximize the sensitivity) the strength of the bias field is chosen such that the magnetization direction at zero field is 45° away from the easy axis. There are many different ways to form a traverse bias: the *soft adjacent layer* (SAL) bias scheme is the most employed, in which a soft ferromagnetic layer is laminated with the sensing layer via a thin insulating spacer, as shown schematically in Fig. 2.2.13 [85].

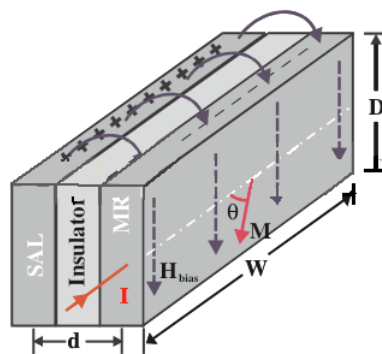


Fig. 2.2.13 Schematic of an AMR sensor using an SAL bias. The sensor consists of an MR element as the active layer and a soft adjacent layer (SAL) for traverse bias separated by an insulating spacer.

The SAL scheme offers many advantages, such as, uniform bias field distribution, adjustable bias field and reduced demagnetizing field. In any case the difficulty to scale AMR sensors down in thickness to follow the reducing of bit and the fast progress made in GMR have determined the short lifetime of the AMR sensors in the history of heads for hard disk. They were gradually replaced by the spin-valve sensor, which was first introduced into commercial devices by IBM in 2000.

2.2.10 Giant MR

Giant MR (GMR) was discovered in 1988 [86] after studying multilayer magnetic nanostructures Fe/Cr, which consisted of a sequence of magnetic layers separated by a nonmagnetic layer. In these structures a large progressive decrease in resistance was observed when the configuration of the magnetization in the adjacent magnetic layers changes from an antiparallel alignment to a parallel one. Fig. 2.2.14 displays the values of the magnetoresistive ratio greater than 45% at 4 K after the application of a magnetic field of 2 T. The saturation field H_S is the field required to overcome the antiferromagnetic coupling (AF) interlayer, i.e. to align the magnetizations of successive layers of Fe.

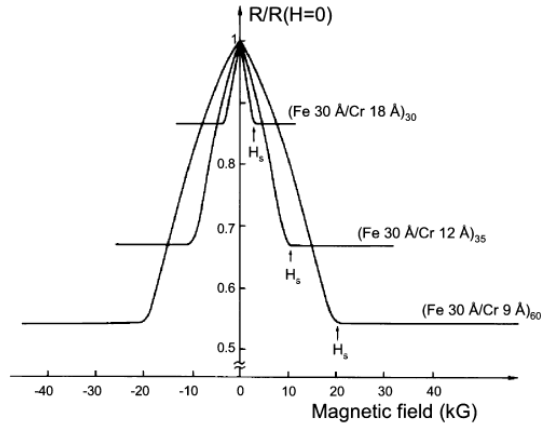


Fig. 2.2.14 Magnetoresistance of Fe/Cr superlattices.

The physical origin of GMR is due to the influence of electron spin on electrical transport properties in ferromagnetic conductors. As originally proposed by Mott [80], the spin splitting of energy bands in the ferromagnetic state leads to specific behaviors of transport. He suggested that the electric current in ferromagnetic metals is divided in two independent conduction channels corresponding to the electrons of spin up and spin down. The conductivity may be significantly different in the two spin channels, as the rate of scattering in the two channels are connected to the corresponding spin-up and spin-down density of states at the Fermi level: in Co, for example, the density states at the Fermi level is ten times higher for spin-down electrons than spin-up electrons, which constitute the majority of electrons [87]. The dependence on the spin of conduction in ferromagnetic metals and alloys was subsequently also demonstrated experimentally [88,89], giving account of the results through the model of so-called "two current". In this model are considered as two independent parallel channels for electric current: up-spin electrons (\uparrow) and spin-down (\downarrow), corresponding to of majority and minority electrons. The conductivity of the ferromagnet is then the sum of two independent contributions, and the resistivity can be expressed as:

$$\rho = \frac{\rho_{\uparrow}\rho_{\downarrow}}{\rho_{\uparrow}+\rho_{\downarrow}} \quad (2.2.80)$$

Assuming that the resistivity of the majority electrons (ρ_{\uparrow}) is very different from the resistivity of the minority electrons (ρ_{\downarrow}), so that the ratio of asymmetry between the two resistivity, $\rho_{\downarrow}/\rho_{\uparrow}$, is very different from 1, it is possible to outline the behavior of giant magnetoresistive material, active in the ferromagnetic/non-magnetic multilayer, through the scattering dependent on the spin, both due to defects and impurities in the magnetic layer, and to the presence of interfaces. In the parallel configuration, when $H > H_s$ and the magnetization of all magnetic layers are parallel to the applied field (section (a) of Fig. 2.2.15), the electrons in the channel of spin-up are the majority electrons in both magnetic layers, contrary to the spin-down electrons constituting the minority.

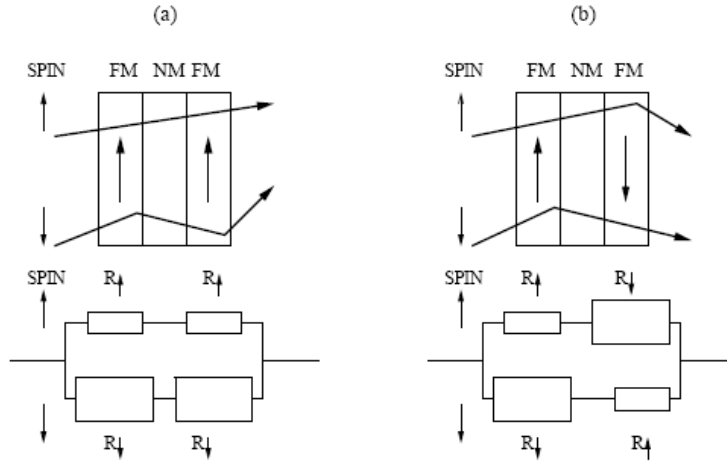


Fig. 2.2.15 Resistor model of GMR.

Hence, the resistance is different for the two channels and in the parallel configuration is:

$$\rho_P = \frac{\rho_{\uparrow}\rho_{\downarrow}}{\rho_{\uparrow}+\rho_{\downarrow}} \quad (2.2.81)$$

In the antiparallel configuration, where the consecutive magnetic layers are coupled antiferromagnetically, the electrons of both channels are either majority or minority, so that the short circuit of one of the channels disappear and the resistance is the same in both channels is equal to:

$$\rho_{AP} = \frac{\rho_{\uparrow}+\rho_{\downarrow}}{2} \quad (2.2.82)$$

and the MR ratio is:

$$MR = \frac{\rho_P - \rho_{AP}}{\rho_{AP}} = - \left(\frac{\rho_{\uparrow} - \rho_{\downarrow}}{\rho_{\uparrow} + \rho_{\downarrow}} \right)^2 \quad (2.2.83)$$

If the diffusion of the spin is strongly asymmetric (i.e. $\rho_{\uparrow} \ll \rho_{\downarrow}$), that is if the electrons scatter with different rate when they penetrate the ferromagnet, in the parallel configuration current is practically short-circuited in the not diffused channel spin and the resistance has a low value ($\rho_P \approx \rho_{\uparrow}$) while in the antiparallel configuration currents are limited by diffusion in both layers and the resistance ($\rho_{AP} \approx \rho_{\downarrow}/4$) is much higher than the parallel configuration. Let's consider a very thin non-magnetic layer between two magnetic layers, and assume that the mean free path of conduction electrons, for both directions of spin, is significantly greater than the thickness of each individual layer, so that it can mediate the scattering over the entire structure. When the ratio between the electronic mean free path and the thickness of the layers becomes less than one, a progressive decoupling of scattering processes in successive layers takes place and the GMR effect gradually tends to zero. Ultimately, the GMR effect depends on the coupling between the ferro or antiferromagnetic layer with $\rho_P < \rho_{AP}$, but is independent of the direction of the field.

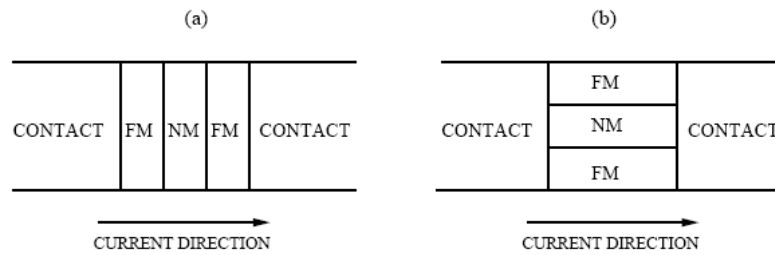


Fig. 2.2.16 CCP(a) and CIP(b) configuration

Two main geometries for GMR can be considered. According to Fig. 2.2.16, in the case (a), the current flows perpendicular to the layers (CPP geometry - Current Perpendicular Plane), while in case (b), the current flows in the plane of the layers (CIP geometry - Current In Plane). Although the theory of the CPP geometry is easier to handle, this geometry is more difficult to achieve experimentally. The resistance presented by a multilayer in the CPP geometry is very low and requires sophisticated experimental techniques for an accurate measurement. However the geometry CPP has an higher magnetoresistive effect not only because of the increased efficiency of interfaces, but also of the spin accumulation due to a change in the resistive contribution of each channel at the interface. In fact, some electrons with majority spin reverses spin direction (*spin flip*). In this process, it can be introduced a characteristic length, called spin diffusion length, depending of each material; this can be larger than the electronic mean free path, and hence allows GMR effect also at higher thickness than layers. The amplitude of the magnetic field needed for the transition from a AF to a ferromagnetically ordered configuration is of course the key feature of these systems. In the case of Fe/Cr multilayer, field switch is close to 2 T, a value too high for any GMR applications (see magnetoresistive heads where the field on the surface of the recording media (disks and tapes) is less than 2 mT). In order to reduce the value of the switching field spin-valve a configuration as sketched in Fig. 2.2.17 can be used, where one of the layers has a fixed direction of magnetization (*pinned layer*) through exchange magnetic interactions by a antiferromagnetic or ferromagnetic layer. On the other side of the structure a magnetically soft layer can direct freely its magnetization under the external applied field. The non-magnetic layer thickness decoupling magnetically the two layers.

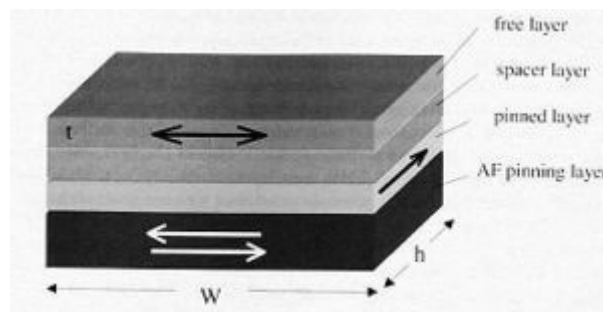


Fig. 2.2.17 Scheme of a typical spin valve

GMR based devices have been used extensively in reading heads of modern hard drives and magnetic sensors. Current perpendicular-to-plane (CPP) GMR spin valve currently is the most employed.

The first GMR structure, consisting of Fe/Cr, Co/Cu, cannot be used for reading in the original form because of their large saturation fields, and the nonlinear response near the zero-field point. A way to reduce the saturation field is to reduce the exchange coupling between the ferromagnetic layers increasing the thickness of the spacer but a weakly coupled multilayer structure does not work properly because of the possible inconsistent movement of all of the magnetic layers under an external field. To overcome this problem the *pseudo-spinvalve* has been developed in which two decoupled layers, one much softer than the other so that the first responds to a small field, while the latter only changes its magnetic at a large field. Different coercive fields can be achieved by using two different materials or the same material but with different thickness [90]. If the soft layer has a very small coercivity, the $MR(H)$ characteristic (Fig. 2.2.18) shows narrow hysteresis and the device can be used as a sensor in the range of field determined by the coercivity of the hard layer. The magnetic stiffness of the hard layer can be improved by using the *exchange bias (EB) effect* [91,92] that occurs in ferromagnet/antiferromagnet (F/AF) systems and consists in an increased of the coercivity and in a shift of the hysteresis loop from the zero field axis, in a direction opposite to that of the cooling field, after the sample is heated up to above the Néel temperature.

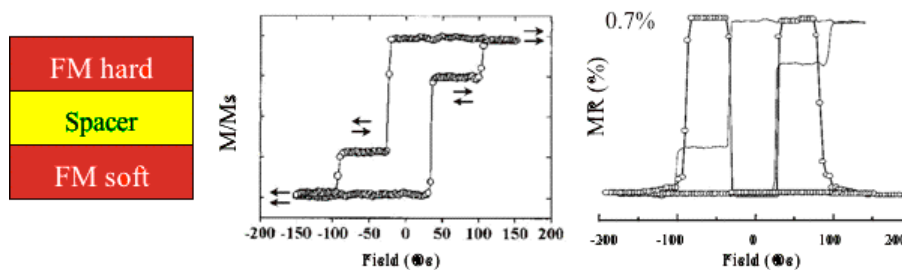


Fig. 2.2.18 $MR(H)$ characteristic of a pseudo-spinvalve.

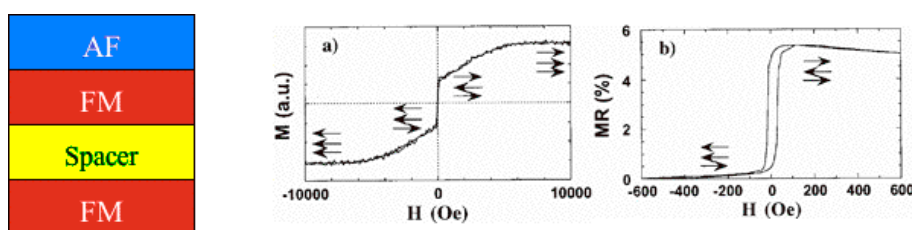


Fig. 2.2.19 $MR(H)$ characteristic of a conventional-spinvalve.

The magnetization of the top layer is “pinned” by the AF-layer, and thus this F-layer is commonly called the *pinned layer*. Moreover, the magnetization of the other F-layer is free to rotate after the application of an external field (*free layer*). In the case of common AF materials (i.e. FeMn or IrMn) the structure is called *conventional spin-valve*. If r AF coupled multilayers are used for the pinning (i.e. Fe/Cr or Co/Cu) the structure is called *synthetic spin-valve*. Typical $M(H)$ and $MR(H)$ loops are shown in Fig. 2.2.19.

2.2.11 Tunnel MR

The Tunneling MagnetoResistance (TMR) appears in heterostructures consisting of ferromagnetic metal electrodes separated by an insulating layer. This insulating magnetically decouples the layers, and breaks the conductive metal channel, thereby enabling only the tunneling of charge carriers. The TMR effect is closely related to the spin asymmetry in the density of states of a ferromagnetic conductor: this reflects on the probability of tunneling through a potential barrier. The TMR is sometimes used in determining the spin polarization at the Fermi level. Already in 1970, Tedrow and Meservey had discovered that the spin direction is conserved in tunneling processes [93]. The first observation and subsequent interpretation of the spin dependent tunneling between two ferromagnetic electrodes was reported in 1975 [94] studying the properties of magnetic tunnel junctions [16]. As for the GMR in multilayers, the resistance of the junction is connected to the orientation of the magnetization of the ferromagnetic electrodes. In fact, at low temperatures (4.2 K) and no bias voltage, the conductance of this system exhibits a variation of 14% between the parallel and antiparallel alignment of magnetization of the electrodes (see Fig. 2.2.20).

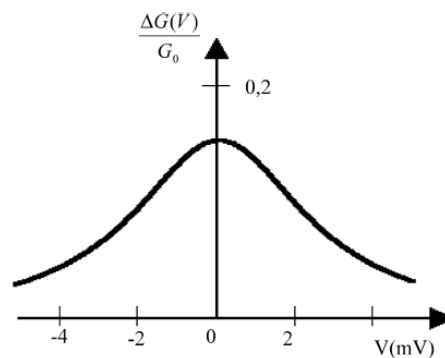


Fig. 2.2.20 Graph showing variation of relative conductivity as a function of voltage observed by Jullie to 4.2 K in structure FeGeCo.

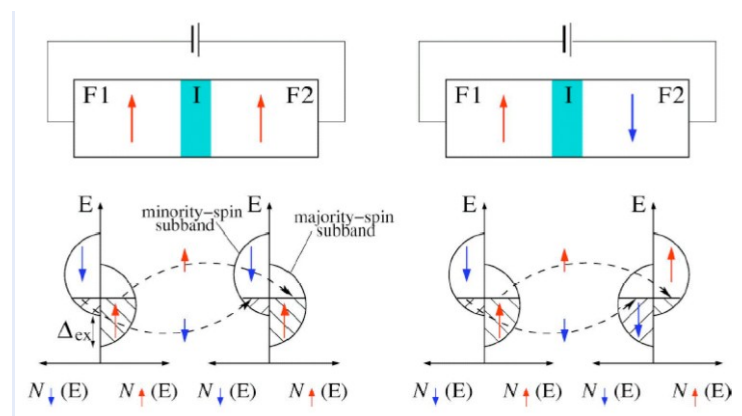


Fig. 2.2.21 Schematic illustration of spin-dependent tunneling across an insulating barrier.

It's possible to describe the TMR in these systems on the basis of the spin polarization function of the electrodes P_i :

$$P_i = \frac{N_{i\uparrow} - N_{i\downarrow}}{N_{i\uparrow} + N_{i\downarrow}} \quad (2.2.84)$$

where $N_{i\uparrow}$ and $N_{i\downarrow}$ are proportional to the density of electronic states at the Fermi level E_f for the two directions of spin in the two ferromagnetic electrodes-. If we consider that the TMR preserves spin and that the tunneling conductance is the sum of two independent conduction channels, one for each direction of the spin is possible to write:

$$TMR = \frac{\Delta\rho}{\rho_{AP}} = \frac{\rho_{AP} - \rho_P}{\rho_{AP}} = \frac{2P_1P_2}{1+P_1P_2} \quad (2.2.85)$$

The measured TMR also decreases with increasing voltage bias, as can be seen in Fig. 2.2.20. The most important factors influencing the value of this magnetoresistive effect are the quality of the barrier, the impurities in the contact ferromagnet/insulator and the distinct values of coercive field in the two electrodes.

2.2.12 Colossal MR

The Colossal MagnetoResistance (CMR) has been evidenced in compounds called perovskites, in the form $A_{1-x}B_xMnO_3$ where atom consists of elements as La, Pr, Nd, Sm, and Ca, Sr, Ba. The perovskite are crystalline ceramic materials whose family also belongs to manganites of lanthanum $LaMnO_3$. They have a cubic structure containing three different ions in the form ABO_3 , where atoms A and B represent ions of valence +3, while the oxygen is ion valence -2. This structure can be thought of as a face-centered cubic lattice with atoms at the vertices and O atoms on the faces. The atom B is in the center of the grid. In the case of $LaMnO_3$ lanthanum ion is A, while the manganese ion B (see Fig. 2.2.22).

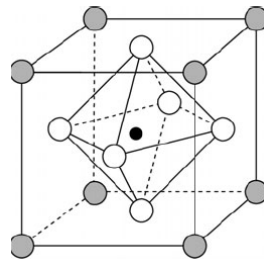


Fig. 2.2.22 Structure of the crystal lattice of $LaMnO_3$: in gray sites of La^{3+} , in white O^{2-} , in black site of Mn^{3+} .

The perovskites are electrical insulating materials: all atomic sites are occupied and strong ionic bonds hinder the movement of electrons through the crystal. However, when the cubic and symmetrical structure of perovskite is distorted, for example by doping with appropriate elements, the crystal may show different conduction properties, behaving, as appropriate, as a conductor, semiconductor or superconductor.

Currently, the interest in the manganites is focused on basic research to understand the physical origin of the colossal magnetoresistance and phase transitions from ferromagnetic to antiferromagnetic in doped manganites $\text{La}_{1-x}\text{D}_x\text{MnO}_3$ type [95]. The applications impacts may be several, mainly in the form of epitaxial thin films, such as electronic devices in microelectronics and opto-electronics, as well as sensors and magnetic heads for hard drives. The magnetic properties and electrical conductivity exhibited by manganites related to the appearance of a mixed valence state of manganese, following the deformation of its atomic orbitals in the crystal lattice, a result of doping with a divalent ion D^{2+} . In the compounds obtained by the complete substitution of trivalent ions La^{3+} with a divalent ion, such as the compound CaMnO_3 , manganese valence is 3+, while in the compound LaMnO_3 has valence 4. In compounds of the type $\text{La}_{1-x}\text{C}_x\text{MnO}_3$, manganese valence state takes an "intermediate" between Mn^{3+} and Mn^{4+} , defined precisely mixed valence [95]. An indirect confirmation that the percentage of dopant element is essential in determining the conduction properties of these compounds comes from several studies carried out on samples of polycrystalline $\text{La}_{1-x}\text{Ca}_x\text{MnO}_3$. These show, for example, a ferromagnetic insulating behavior at low and high values of x , for values around $x \approx 0.33$, the compound behaves instead as a ferromagnetic metal [17]. The magnetic properties of manganites are related to the interaction of exchange between the spins of Mn ions, controlled by the Mn d orbitals overlap with those of oxygen, which can be: $\text{Mn}^{4+}\text{-O-Mn}^{4+}$, $\text{Mn}^{3+}\text{-O-Mn}^{3+}$ or the type $\text{Mn}^{3+}\text{-O-Mn}^{4+}$. The latter case shows a strong ferromagnetic behavior and it's interpreted in terms of mechanism of double exchange (DE - *Double Exchange*) [96]: the manganese ions exchange the valence through a simultaneous jump of e_g electrons of Mn^{3+} to the p orbital of oxygen, and orbital p of oxygen to the empty orbital e_g of Mn^{4+} . The mechanism of double exchange is the basis of electrical conduction in the manganites. In conclusion, in CMR materials the conduction occurs by hopping conduction.

2.2.13 Domain Wall MR

Domain Wall MagnetoResistivity (DWMR) is a physical effect which can be understood by considering the geometrical similarity between a GMR structure and a domain wall (see Fig. 2.2.23). In GMR structures regions of different magnetization are separated by an intermediate thin film of nonmagnetic metal, and this layer is in the form of a thin film of nonmagnetic metal where the spin conservation occurs. By analogy, it is possible to develop a model of domain wall resistance in which the value of the resistance is determined by the degree of spin depolarization of the charge carriers in the twisted magnetic structure formed at the heart of the domain wall [97,98]. This model assumes that an electron moves through a domain wall by precessing about an axis, which is tilted at a fixed angle with respect to the local magnetization direction in the wall. The average angle with local magnetization is:

$$\theta = \frac{h k_F v_F}{E_{ex} w} \quad (2.2.86)$$

where h is the Planck constant, v_F the Fermi velocity, E_{ex} is the exchange length, w domain wall thickness and k_F is the Fermi wavevector.

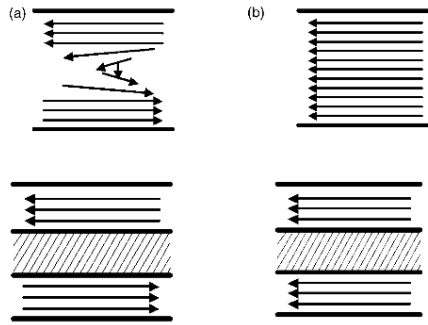


Fig. 2.2.23 Geometrical similarities between (a) a DW and (b) a GMR trilayer.

This is equivalent to its wave function being contaminated by a fraction $\sin(\theta/2)$ of the down-spin wave function. The up spin is then susceptible to additional scattering by an amount equivalent to $\sin^2(\theta/2)$ multiplied by the down-spin scattering rate. The spin-dependent contribution to the domain wall resistivity can be written as:

$$\frac{\Delta\rho_W}{\rho_0} = \left(\frac{\lambda^*}{\lambda} + \frac{\lambda}{\lambda^*} - 2\right) \langle \sin^2\left(\frac{\theta}{2}\right) \rangle \quad (2.2.87)$$

where λ and λ^* are the majority and minority spin mean free paths, ρ_0 and $\Delta\rho_W$ are, respectively, the bulk F resistivity and the resistivity increase due to domain wall contribution. Let's note that that the magnetoresistive contribution falls rapidly while increasing the wall thickness w . For bulk wall thicknesses (several tens of nanometers) this contribution is not detectable (or at least very small). Thus, if we are able to constrain a DW (thanks to the nanotechnology) in a nanosized structure, as discussed in this chapter, we can modulate the w and so the MR. A ballistic magnetoresistance (BMR) was detected in nanocontacts between two ferromagnetic materials, with values of the magnetoresistive ratio at room temperature up to, 200-400% [99,100]. This magnetoresistive effect is related to the spin dependent scattering, which is active at domain walls trapped in the region when this constraint is the order of a few atomic distances. In this case the domain wall width δ_w is not much larger than the Fermi wavelength λ_F , and the electronic transport becomes ballistic rather than diffusive. When the width of constriction becomes comparable to λ_F the conductance in magnetic materials is quantized in units of e^2/h . The BMR decreases very quickly when the size of the contact continuously raised a few hundred atoms.

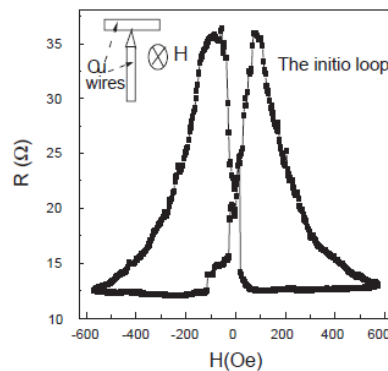


Fig. 2.2.24 BMR curves showing values up to about 400% in Fe nanocontact. Taken from [100]

The rule of a DW into MR is determined by a resistive contribution that rapidly increases with a reduction of the DW width. Thus the possibility to change the width and displacement of DWs makes this magnetoresistive effect suitable for practical applications such as sensing and digital spintronic. A DW can be constrained, either by a geometrical constrain or because it has to pass from a region with low coercivity to a region with high coercivity (a simple micromagnetic simulation based on the LLG equation shows that in Fig. 2.2.25:

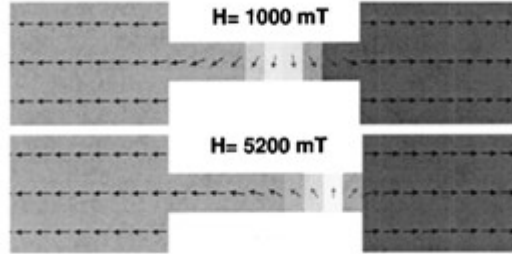


Fig. 2.2.25 LLG micromagnetic simulation for a DW in a nano-channel comprised between two region with different coercivity (light grey correspond to the region with lower coercivity) [101].

When a magnetic field H_a is applied in the film plane so that it exerts a force on the wall, for values of H_a smaller than a certain H_{cr} (coercitive), it is more energetically convenient for the system to reduce the DW width, rather than displace it [101]. On the contrary, when H_a reaches H_{cr} , the wall is displaced. In the range $0 < H_a < H_{cr}$, the resistance changes as a function of the field, and the system works as a field sensor (see Fig.2.2.26).

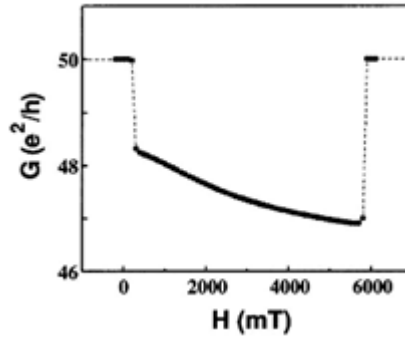


Fig. 2.2.26 Conductance vs applied field.

The force on the wall can be exerted by a current, instead of by an external applied magnetic field. The theoretical description of *current-induced domain wall motion*, or in other words, the interaction of spin polarized charge carriers with the magnetization of the material, is a complicated issue. We will briefly describe the phenomenon here in the framework of the *spin transfer torque* model starting from the LLG equation. Considering the geometrical similarity between a GMR structure and a domain wall, as described in this chapter, the spin transfer of a polarized current on a DW can be simply phenomenologically introduced adding an additional term in the LLG [102]:

$$\frac{dm}{dt} = -\gamma'(\mathbf{m} \times \mathbf{H}_{eff}) - \alpha' \mathbf{m} \times [\mathbf{m} \times (\mathbf{H}_{eff} + b\widehat{\mathbf{m}}_p)] \quad (2.2.88)$$

where b must be a constant depending on current intensity and polarization. In case of a DW in a film, we cannot distinguish between free and pinned layers. The “pinned layer” is just the same layer in which the magnetization changes. It is more appropriate to consider the same magnetization vector \mathbf{m} and its variation in the space. It's possible to write the torque as [103]:

$$\tau = -\frac{1}{M_S^2} \mathbf{M} \times [\mathbf{M} \times (\mathbf{u} \cdot \nabla) \mathbf{M}] \quad (2.2.89)$$

where

$$\mathbf{u} = \frac{g^P \mu_B}{2eM_S} \mathbf{J} \quad (2.2.90)$$

is a velocity vector whose amplitude is a_J/M_S and parallel to the current direction. Li and Zhang [103] have shown that the spin transfer torque on a domain wall has many features in common with that at an interface with the ratio t_f/w of the thickness of the ferromagnetic layer to the width of the domain wall, i.e. the torque is proportional to the volume of the material that experiences spin transfer effects. Using the form of the LLG given by eq. 2.2.48 and adding the additional spin transfer term, we can write the modified LLG, in case of current flowing in the x direction, as:

$$\frac{\partial \mathbf{m}}{\partial t} = -\gamma_0 (\mathbf{m} \times \mathbf{H}_{eff}) - \alpha \mathbf{m} \times \frac{\partial \mathbf{m}}{\partial t} - u \mathbf{m} \times \left(\mathbf{m} \times \frac{\partial \mathbf{m}}{\partial x} \right) \quad (2.2.91)$$

where the last term is the *torque term in the adiabatic limit*. At today the most important application of spin transfer torque is in TMR heads and it is good candidate in MRAM technology; however, the amount of current needed to realign the magnetization is too high for commercial applications [104].

References:

- [33] K. S. Ill'in, I.I.Milostnaya, A.A.Verevkin, G.N.Gol'tsman, E.M.Gershenson, R.Sobolewski, Appl. Phys. Lett. 73,3938,(1998)
- [34] G. N. Gol'tsman et alter, Appl.Phys.Lett. 79,705,(2001)
- [35] A. Verevkin et al.,Appl.Phys.Lett. 80,4687,(2002).
- [36] J. Zhang et alter,Electron.Lett. 39,1086,(2003).
- [37] Goltsman et al., Phys.Stat.Sol.(c), Vol. 2, N.5,1480-1488,(2005).
- [38] K. S. Il'in, I.I.Milostnaya,A.A.Verevkin,G.N.Gol'tsman,E.M.Gershenson and R.Sobolewski, Appl. Phys.Lett. 73,3938,(1998).
- [39] A. Rotwarf and N.B. Taylor, *Phys. Rev. Lett.* **19**, 27 (1967)

- [40] E. N. Grossman, D. G. McDonald, J. E. Sauvageau; "Far-infrared inductive detectors"; *IEEE Trans. Magn.*, vol. 27, no. 1, pp. 2677, 1991.
- [41] N. Bluzer; "Analysis of quantum superconducting kinetic inductance photodetectors"; *J. Appl. Phys.*, vol. 78, no. 1, pp. 7340, 1995.
- [42] F. Hegman, J. Preston, Origin of the fast photoresponse of epitaxial YBCO thin films, *PRB* vol. 48, N. 21, 1993
- [43] G. N. Gol'tsman, O. Okunev, G. Chulkova, A. Lipatov, A. Semenov, K. Smirnov, B. Voronov, A. Dzardanov, C. Williams, R. Sobolewski; "Picosecond superconducting single-photon optical detector"; *Appl. Phys. Lett.*, vol. 79, no. 1, pp. 705, (2001).
- [44] J. P. Maneval et al., *JOS: incorporating Novel Magnetism*, vol. 14, no. 2, (2001)
- [45] W. J. Skocpol, M. R. Beasley, M. Tinkham; "Self-heating hotspots in superconducting thin-film microbridges"; *J. Appl. Phys.*, vol. 45, no. 1, pp. 4054, (1974).
- [46] O. Quaranta, PhD thesis, Development and characterization of innovative Superconductive Nanowire Single Photon Detectors, Univ. degli studi di Salerno, (2008).
- [47] A. D. Semenov, G. N. Gol'tsman, A. A. Korneev; "Quantum detection by current carrying superconducting film"; *Physica C*, vol. 351, no. 1, pp. 349, (2001).
- [48] A. Korneev, V. Matvienko, O. Minaeva, I. Milostnaya, I. Rubtsova, G. Chulkova, K. Smirnov, V. Voronov, G. Gol'tsman, W. Słysz, A. Pearlman, A. Verevkin, R. Sobolewski; "Quantum Efficiency and Noise Equivalent Power of Nanostructured, NbN, Single-Photon Detectors in the Wavelength Range from Visible to Infrared"; *IEEE Trans. Appl. Supercond.* Vol. 15 no. 2 (2005).
- [49] D. Pan et al. *Phys. Rev. B* **78**, 174503 (2008)
- [50] A. A. Golubov, E. P. Houwman, J. G. Gijsbertsen, V. M. Krasnov, M. Yu. Kupriyanov, J. Flokstra, *Phys. Rev. B*, **51**, 1073 (1995.)
- [51] A. F. Andreev, *The thermal conductivity of the intermediate state in superconductors*, *Sov. Phys. JETP* 19 (1964), 1228.
- [52] Ya. V. Fominov et al. *Phys. Rev. B*, **66**, 014507 (2002).
- [53] C. Cirillo et al, *Superconducting proximity effect and interface transparency in Nb/PdNi bilayers* *PRB* **72**, 144511 (2005).
- [54] T. Van Duzer and C. W. Turner, *Superconductive devices and circuits*, Second edition, Prentice Hall PTR, p. 357, (1998).

- [55] A. F. Hebard and A. T. Fiory, "Vortex dynamics in two-dimensional superconductors," *Physica* 109 & 110B, 1637 (1982).
- [56] L.G. Aslamasov, A.I. Larkin, "The influence of fluctuations pairing of electrons on the conductivity of normal metal," *Phys. Lett. A*, vol. 26, 238 (1968).
- [57] J. M. Kosterlitz, D. J. Thouless, "Ordering, metastability, and phase transitions in twodimensional systems", *J. Phys. C*, vol. 6, p. 1181 (1973).
- [58] Z. L. Bereizinskii, *Zh. Eksp. Teor. Fis.*, vol. 61, p. 1144 (1971).
- [59] J. E. Mooij, "Two-dimensional transition in superconducting films and junction arrays," in *Percolation, localization, and superconductivity*, A. M. Goldman and S. A. Wolf, Eds., NATO ASI, series B, vol. 109. New York: Plenum Press, pp. 325-370 (1984).
- [60] A. M. Kadin, K. Epstein, and A. M. Goldman, "Renormalization and the Kosterlitz Thouless transition in a two-dimensional superconductor," *Phys. Rev. B*, vol. 27, pp. 6691-6702 (1983).
- [61] A. M. Kadin, "Duality and fluxonics in superconducting devices," *Journ. Appl. Phys.*, vol. 68, 5741 (1990).
- [62] B. I. Halperin and D. R. Nelson, "Resistive transition in superconducting films," *J. Low Temp. Phys.*, vol. 36, p. 599 (1979).
- [63] K. K. Likharev, "Superconducting weak links", *Rev. Mod. Phys.*, vol. 51, p. 101 (1979).
- [64] M. Bell, A. Sergeev, V. Mitin, J. Bird, A. Verevkin, G. Gol'tsman, "One-dimensional resistive states in quasi-two-dimensional superconductors: experiment and theory," *Phys. Rev.B*, vol. 76, 094521 (2007).
- [65] A. Aharoni, *Introduction to the Theory of Ferromagnetism* (Oxford Science Publications, 1996).
- [66] R. D. Cullity, *Introduction to Magnetic Materials* (Addison-Wesley, Reading, MA, 1972).
- [67] S. Chikazumi, *Physics of ferromagnetism* (Clarendon Press – Oxford, 1997).
- [68] M. T. Johnson, P. J. H. Bloemen, F. J. A. den Broeder, and J. J. de Vries, *Rep. Prog. Phys.* **59**, 1409 (1996).
- [69] W. F. Brown, *J. Phys. Rev.* 60, 139 (1941)
- [70] G. Bertotti, *Hysteresis in magnetism* (Academic-Press, 1998).
- [71] C. Kittel, *Rev. Mod. Phys.* **21**, 541 (1949).
- [72] F. Bloch, *Z. Physik* **74**, 295 (1932).
- [73] L. Néel, *Comptes. Rendus* **241**, 533 (1955).
- [74] R.H. Wade *Proc. Phys. Soc.* 79, (1962)

- [75] D. J. Craig and R. S. Tebble, *Magnetic domains*, Repts. Prog. Phys. 24, 116 (1961).
- [76] R.H. Wade *Proc. Phys. Soc.* 79, (1962)
- [77] P. Bruno, Phys. Rev. Lett. **83**, 2425 (1999).
- [78] Y. Labaye, L. Berger and J. M. D. Coey, J. Appl. Phys. **91**, 5341 (2002).
- [79] A. B. Pippard, *Magnetoresistance in metals*, Cambridge University Press, (1989).
- [80] N. F. Mott, Electrons in transition metals, Adv. Phys., 13 (1964) 325.
- [81] E. Englert, Change of electric resistivity in longitudinal and transverse magnetic fields, Ann. Physik, 14 (1932) 589.
- [82] O. Stierstadt, Change of electric conductance of ferromagnetic materials in longitudinal fields, Physik Z., 31 (1930) 561.
- [83] T. R. McGuire and R. I. Potter, IEEE Trans. Magn. MAG **11**, 1018 (1975).
- [84] R. Hunt, *IEEE Trans. Magn. MAG* **7**, 150 (1971).
- [85] J. C. Mallinson, *Magneto-Resistive Heads: Fundamentals and Applications*, Academic, New York, (1996).
- [86] M.N. Baibich, J.M. Broto, A. Fert, F. Nguyen Van Dau, F. Petroff, P. Eitenne, G. Creuzet, A. Friederich, J. Chazelas, Giant magnetoresistance of (001)Fe/(001)Cr magnetic superlattices, Phys. Rev. Lett., 61 (1988) 2472.
- [87] I. A. Campbell, A. Fert, *Ferromagnetic Materials*, North Holland, (1982).
- [88] A. Fert, I. A. Campbell, Two-current conduction in nickel, Phys. Rev. Lett., 21 (1968) 1190.
- [89] A. Fert, I. A. Campbell, Electrical resistivity of ferromagnetic nickel and iron based alloys, J. Phys. F, 6 (1976) 849.
- [90] J. F. Loffler, J. P. Meier, B. Doudin, J. P. Ansermet, and W. Wagner, *Phys. Rev. B* **57**, 2915(1998).
- [91] J. Nogues and I. K. Schuller, *J. Magn. Magn. Mater.* **192**, 203 (1999).
- [92] A. E. Berkowitz and K. Takano, *J. Magn. Magn. Mater.* **200**, 552 (1999).
- [93] R. Meservey, P. M. Tedrow, P. Fulde, Magnetic field splitting of the quasiparticle states in superconducting aluminum fields, Phys. Rev. Lett., 25 (1970) 1270.
- [94] M. Jullière, Tunneling between ferromagnetic films, Phys. Lett. A, 54 (1975) 225.

- [95] A. M. Haghiri-Gosnet, J. P. Renard, CMR manganites: physics, thin films and devices, *J.Phys.D: Appl.Phys.*, 36 (2003) R127.
- [96] C. Zener, Interaction between the d shells in the transition metals, *Phys. Rev.*, 81 (1951) 440.
- [97] J. F. Gregg, W. Allen, K. Ounadjela, M. Viret, M. Hehn, S. M. Thomson and J. M. D. Coey, *Phys. Rev. Lett.* **77**, 1580 (1996).
- [98] M. Viret, D. Vignoles, D. Cole, J. M. D. Coey, W. Allen, D. S. Daniel and J. F. Gregg, *Phys. Rev. B* **53**, 8464 (1996).
- [99] N. García, M. Muñoz, Y.-W. Zhao, Magnetoresistance in excess of 200% in ballistic Ni nanocontacts at room temperature and 100 Oe, *Phys. Rev. Lett.*, 82 (1999) 2923.
- [100] N. García et al. *Journal of Magnetism and Magnetic Materials* 272–276 (2004) 1722–1729
- [101] J. D. Burton, A. Kashyap, M. Ye. Zhuravlev, R. Skomski, E. Y. Tsympal, and S. S. Jaswal, O. N. Mryasov and R. W. Chantrell, *Appl. Phys. Lett.*, **85**, 251 (2004).
- [102] J. C. Slonczewski, *J. Magn. Magn. Mater.* **159**, L1 (1996).
- [103] Z. Li and S. Zhang, *Phys. Rev. Lett.* **92**, 207203 (2004).
- [104] D.C. Ralph, M.D. Stiles *Spin transfer torques* J.M.M.M. 320 (2008) 1190-1216.

Chapter 3: Devices fabrication and characterization

3.1 Sputter deposition

Sputtering belongs to that class of techniques for preparing thin films and multilayer known as Physical Vapor Deposition techniques (PVD). It allows control over the thickness of individual layers up to fractions of a nanometer, allowing, through its many variants, the deposition of metals and insulators, as well as materials such as ceramic, with high value of melting temperature. While the classic statements are made by evaporation in high vacuum (up to 10^{-6} Torr), since the mean free path of particles evaporated components flow is limited because of low energy that they have, instead sputtering generally carried out at pressures in the order of mTorr. DC sputtering method is simplest to depositing conductive materials. The target, consists of the material to be deposited, is connected to a DC power supply, while the substrate is placed on the front, connected to ground (most frequent solution Fig. 3.1) or powered by a bias current, and can be cooled or heated to specific temperature. After inserting the sputtering gas - usually argon - in the chamber deposition where earlier it had created vacuum, it is applied to target a negative potential difference to generate a plasma, characterized by strong luminescence. The positive ions of plasma bombard the target surface, extracting mainly neutral atoms, which then condense on the substrate. When the voltage is applied to the target, initially only a small current is induced to flow through the system because of the limited number of charge carriers. Increasing potential difference, however, more carriers are created, this partly due to secondary electrons emitted from the target, in part due to the impact ionization process of electrons against atoms of argon. As a result, the current increases and creates a shock in the gas in the deposition chamber.

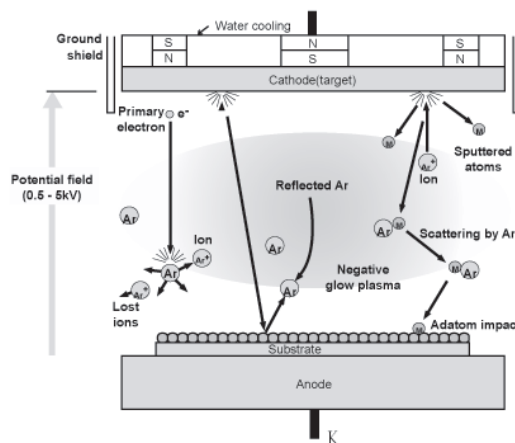


Fig. 3.1 Scheme of the sputtering

This process reaches a steady state when the number of electrons and ions produced is the same, so that the process of creating the plasma can sustain themselves. At this point, the discharge becomes clearly visible as a glow near the target.

The ionization and thus the rate of sputtering, both can be enhanced by increasing the potential difference. Another way to increase the current, i.e. the sputtering rate, fixed a given value of the potential, is to increase the gas pressure of argon in order to be able to ionize more atoms is necessary, however, that the pressure does not increase excessively, since, otherwise, there may be a decrease in the rate due to inelastic slow ions colliding with atoms not ionized. Pressures typical sputtering processes are in the tens or hundreds of mTorr. An additional parameter that should be carefully considered is the separation between the electrodes. Optimal separation provides sufficient space for the secondary electrons can collide with argon atoms and ionize before reaching the anode. While if space is excessive, the ions produced by collisions can lose much of their energy and reach the cathode with sufficient energy to generate additional secondary electrons. Typically, the separation between the electrodes is a few inches. The three previously described variables (potential difference, the gas pressure and distance between electrodes) are connected to each other according to Paschen's law:

$$V_B = \frac{APd}{\ln(Pd)+B} \quad (3.1)$$

where V_B is the potential difference, P is pressure, d is the distance between electrodes and A and B are constants. In the case of DC insulation method can't be used because the target would be quickly and positively charged and positive ions of the plasma would be rejected. In this case, a voltage radio frequency, usually at 13.56 MHz is applied to the target in the variant called RF sputtering. Raise the frequency of the AC signal applied, it must be consider the different mobility of electrons than ions. The difference in mobility between electrons and ions leads to the formation of a negative bias on the target. At this frequency, the ions are relatively immobile. Therefore, if the target is coupled to the power generator via a capacitor in series, application of an RF signal electrons are pushed towards the target during the first half of the cycle. The second half of the cycle can't generate a similar current flow in the opposite direction due to the difference in mobility of charge carriers: the target thus acquires a negative charge. This happens on both electrodes. So if only the target is for sputter, it must consist of insulating material. The use of a magnetic field in a sputtering leads to more efficient use of electrons, so that they can produce more ionization. In a conventional sputtering system, in fact, there is a loss of electrons by recombination on the walls of deposition chamber. To minimize this loss can use a magnetic field in *magnetron* systems electrons are trapped near the target surface, thus enhancing the effect of ionization. In this way, losses are eliminated to the electrons that go to the anode or recombine on the walls of the room. Indeed, the field lines of permanent magnets on the back of the target act to channel the electrical charge and concentrate the plasma near the target, resulting in increasing the rate of sputtering.



Fig. 3.2 Magnetron sputtering (Py target) - University of Naples "Federico II".

3.2 Pulsed Laser Deposition

The removal of material from the surface of a solid due to irradiation by a high-power laser is usually called laser ablation: this technique is called Pulsed Laser Deposition (PLD) when the ejection of macroscopic quantities of material is done through the use of short ($\sim 10^{-13} \div 10^{-8}$ s) and intense ($\sim 10^9 \div 10^{14}$ Wcm⁻²) laser pulses. PLD systems can produce films with quality comparable to that obtained by systems of molecular beam epitaxial growth (MBE - Molecular Beam Epitaxy), but with costs ten times less. Among the great advantages that this technique can count the flexibility is the most important, linked to the energy source that creates the "plume" (*plume*, mixture of atoms, molecules, electrons, ions, and molten globules) that is independent of the deposition system. This decoupling eliminates the limitations that other deposition techniques require due to the use of evaporation sources inside the evaporation environment where the deposition takes place, such as in the case of sputtering or MBE, whose average rates of deposition are also much lower than the laser ablation process (about 10 Å /s for PLD respect 3 Å /s for technology MBE). Fig. 3.3 shows the schematic diagram of a PLD apparatus.

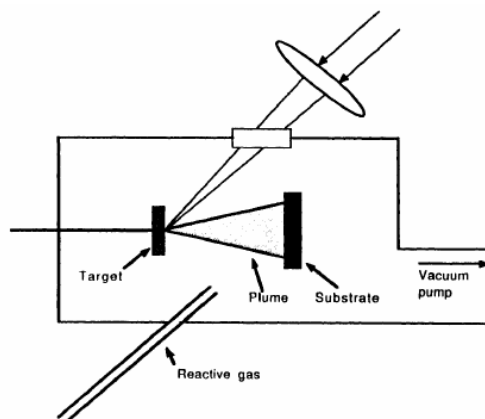


Fig. 3.3 Schematic diagram of a PLD apparatus.

Inside the vacuum chamber in which achieves ablation, an appropriate gas may be placed to improve the quality of films produced or to correct its stochiometry.

The nature of the phenomena induced by laser radiation in transparent solids (insulators or dielectric) and absorbent (metals and semiconductors) is determined, for the most part, the coupling of the laser parameters, pulse width τ_L , the wavelength λ_L and incident energy per unit area (fluence F) as well as the possible presence of a gas chamber and its pressure with the optical, mechanical and thermal properties of the material. To all 'today, there isn't a model that describes the process in its entirety. When the laser radiation is absorbed by the solid surface, the electromagnetic energy is converted first into electronic excitation, resulting in a gas of electrons and/or electron-hole pairs at temperature T_e , which heats the initially colder ions (at temperature T_i) reaching an equilibrium state in $\tau_E \approx 10^{-12} /^{11} s$, and then into heat energy, chemical and even mechanical. If the target is a dielectric, the high intensity laser pulse gives rise to an electromagnetic field within the material, causing them to break (electrical breakdown) and creating a plasma of atoms, molecules, electrons, ions and clusters (micro-particulate). In the case of metal target, the laser radiation is absorbed by free electrons and then transferred to the lattice, causing heating of the region (thickness a few microns) to the evaporation of a thin layer of material, if the pulse energy is high enough. If $\tau_L > \tau_E$, the equilibrium between electrons and phonons is established at a temperature $T_e \approx T$ through processes involving the quasi-equilibrium thermodynamic states. The use of ultrashort laser pulses ($\tau_L \leq 10^{-12} s$), leaving the material in a highly non-equilibrium state after optical energy deposition ($T_e \gg T_i$) [105]. In the "plume" energetic species have a very short collisional mean free path, so as to produce a rapid expansion in the same manner that they constitute a jet by hydrodynamic flow characteristics. The process of vaporization caused by a laser is in fact different from analogue phenomenon caused by a conventional heat source, for the same thermal energy deposited on target. The laser radiation causes a high temperature increase in volumes very small (the size of the laser spot on target for a few microns deep) and this affects both the composition and the angular distribution of the evaporated materials. The plasma generated by PLD expands mainly in the direction orthogonal to the sample, assuming a characteristic ellipsoidal shape (the plume) with non-homogeneous spatial profile (in the form $\cos^n(\theta)$ with $n > 1$, where θ is the angle with the normal to the surface of the solid sample), as shown in Fig. 3.4.

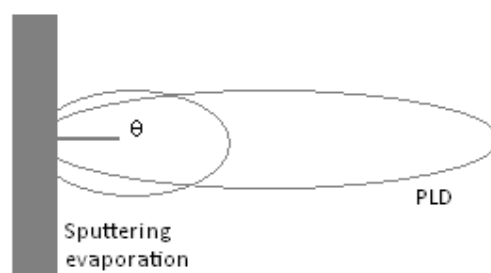


Fig. 3.4 Comparison of spatial profiles related to the technique of sputtering evaporation and PLD.

A good deposition quality requires uniform and homogeneous laser output, especially when dealing with multicomponent targets, with wavelengths between 200 and 400 nm and high energy density (even higher than $1 J/cm^2$). The production of thin films is optimized by the use of targets of high density and homogeneity:

to have an uniform erosion - in order to prevent the occurrence of crater wear and exclude dependencies of the composition of the cloud of ablated material from any irregularities in the sample, the best practice is to rotate them during the deposition. In order to achieve multi-layer structures is generally used a carousel which can be housed more targets and suitably select them. Various types of materials can be employed as substrates such as mica, silicon or glass Corning. It is sometimes required they have to be heating to produce better adhesion or epitaxy, in which case the PLD system must be provided a special holder. In fact, the speed of crystallization of the film is primarily linked to the heat loss of the condensate through the substrate and the heat loss depends to the temperature at which the substrate is maintained. The higher the cooling rate, the lower the rate of crystallization, resulting in an very short average distance of diffusion. When subsequent jet material reaches the substrate, the new rise in temperature causes the evaporation of non-linked more volatile elements. If the substrate temperature is sufficient to allows complete crystallization of the species presented, the subsequent flow of steam leads to evaporation of more volatile species, now incorporated in the crystal structure. This results in a more homogeneous films, relaxed (without internal tensions) and a more correct stochiometry.

3.3 X-ray diffractometry

The X-ray diffraction (XRD) technique is the most important and widely used in solid state chemistry for the identification and characterization of crystalline materials and the determination of their crystal structure [106]. When an X-ray beam hits a set of atoms, there is a phenomenon of diffusion or scattering of electrons by hitted atoms. In particular conditions when they are specific geometric relationships, all the effects of coherent diffusion in certain directions are reinforced while in others directions are annihilated. This phenomenon, called diffraction, is studied both in its geometric terms, both in the intensity it brings. The geometry of the diffraction effects depend on the size of the diffracting lattice and its general characteristics. It is shown that the X-ray diffraction by a crystal lattice can be described as the reflection from the lattice's plans, characterized by Miller indices h, k, l , and the interplanar distance d_{hkl} when the well-known Bragg law is verified:

$$2d_{hkl}\sin\theta = n\lambda \quad (3.2)$$

where θ is the angle of incidence X-rays, n is the order of diffraction and λ the wavelength of radiation used. From this law follows that, known the constants of the unit cell, its orientation to the direction of incidence of X-rays and the wavelength of radiation used, the spatial directions along which are the reflections can be uniquely determined. Any substance micro or nanocrystalline shows a characteristic diffraction specter because the interplanar distances d and the corresponding diffracting intensities depend on the structure and chemical composition of the substance. It follows that the spectrum of X-ray diffraction is indicative of this particular element or compound, either alone or in combination, in the sample.

3.4 Energy Dispersive Spectroscopy

The X-ray signal emitted from the specimen contains characteristic peaks whose energy can be related to an atomic transition and hence to a particular chemical species. Two electron-beam specimen interactions can be considered. There is core scattering, which results in the emission of a continuous background and inner shell ionization, which gives the characteristic peaks. We will just concentrate on the latter. The incident electron has sufficient energy to knock an inner shell electron out to the vacuum. An electron from a higher energy level falls down to the partially filled lower energy level and a photon is emitted. The energy of the photon corresponds to the difference between the two energy levels. Transitions are called as K (*s*-electrons), L (*p*-electrons) or M (*d*-electrons), which is the energy level from which the electron was ejected and they are also introduced with subscripts such as α , β , γ which indicates from which level the electron that fills the hole has come. The X-ray from the most probable transition is designated α . Therefore, a K_α X-ray is formed from a transition from the L shell to the K shell whereas a K_β X-ray results from a transition from the M shell to the K shell. EDS X-ray detector system is based on a silicon based *p-i-n* junction. An incoming X-ray generates a photoelectron, which leads to the generation of a number of electron-hole pairs. The number of pairs generated is proportional to the energy of the X-ray. The signal is amplified and is then sorted according to voltage amplitude by a multichannel analyzer. Several thousand pulses per second can be processed and so a spectrum can be obtained in a short space of time. The current produced by the X-ray is small compared to the conductivity of the silicon and so the junction is reverse biased. The silicon is doped with Li to increase its resistivity and the detector is cooled to keep thermally activated conductivity and electronic noise to a minimum. In order to estimate the amount of an element present in a sample, the number of counts obtained in a fixed time interval, N_{spec} , can be compared with those from a standard of known composition, N_{std} . Therefore, the concentration of the element is given by:

$$C_{spec} = \frac{N_{spec}}{N_{std}} C_{std} = k C_{std} \quad (3.3)$$

However, if the specimen is not a pure element then the situation is more complex. Three correction factors must be applied and we will discuss each one in turn now. The atomic number correction (*Z*) accounts for the differences in the efficiency of X-ray generation. This depends on how far the electrons penetrate before they lose too much energy to excite X-rays and how many electrons are backscattered without exciting X-rays. The absorption correction (*A*) accounts for the differences in the mass absorption coefficients of the elements involved. Finally, the fluorescence correction (*F*) is necessary if element Y emits characteristic X-rays of energies greater than the energy for excitation of characteristic X-rays from element Z. It is a very inefficient process but can be significant if elements have a similar atomic mass. These corrections are known as *ZAF* corrections. To determine these factors, the sample-detector geometry must be known accurately and the sample must be flat. In this case the errors can be as low as $\pm 3\%$. Eq. (3.3) can now be modified to include the *ZAF* corrections:

$$C_{spec} = k k_Z k_A k_F C_{std} \quad (3.4)$$

k_Z , k_A and k_F require some knowledge of the specimen composition so the process is iterative. For the quantitative analysis, standardless analysis was used, which is the simplest correction procedures. There are a few limitations with EDS for measuring thin film. The most important is that the effective probe depth of the incident electrons is about 1 μm . However, the computer program that carries out the analysis assumes that the sample is homogeneous, which is not the case since the thin film is on a substrate. However, if one deposits a thick film (> 100 nm) and uses a low accelerating voltage (for instance 5 keV), all interactions take place within the film.

3.5 Atomic Force Microscopy

Atomic Force Microscopy (AFM) is a form of scanning probe microscopy (SPM) where a small probe scans the sample to obtain information about the sample's surface (fig. 3.5). The information gathered from the probe's interaction with the surface can be simple physical topography or diverse measurements of the material's physical, magnetic, or chemical properties. These data are collected as the probe scans in a raster pattern across the sample to form a map of the measured property relative to the X-Y position [107]. Thus, the AFM microscopic image shows the variation in the measured property, e.g. height or magnetic domains, over the area imaged. The AFM probe has a very sharp tip, often less than 100 \AA diameter, at the end of a small cantilever beam. The probe is attached to a piezoelectric scanner tube. Interatomic forces between the probe tip and the sample surface cause the cantilever to deflect as the sample's surface topography (or other properties) changes. A laser light reflected from the back of the cantilever measures the deflection of the cantilever. This information is feedback to a computer, which generates a map of topography and/or other properties of interest. An important configuration of AFM is Magnetic Force Microscopy (MFM). This mode images local variations in the magnetic forces at the sample's surface. The probe tip is coated with a thin film of ferromagnetic material that will react to the magnetic domains on the sample surface. The magnetic forces between the tip and the sample are measured by monitoring cantilever deflection while the probe is scanned at a constant height above the surface. A map of the forces shows the sample's natural or applied magnetic domain structure.

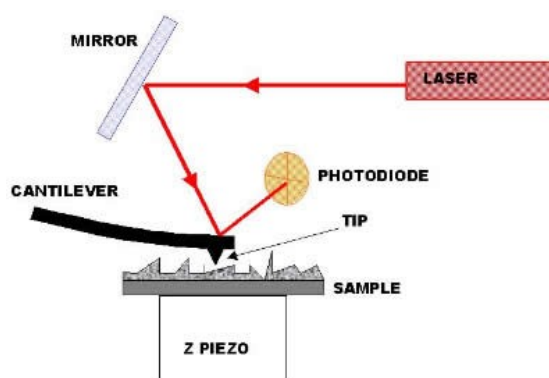


Fig. 3.5 Schematic of AFM setup.

3.6 Vibrating Sample Magnetometer

The part of the study of the magnetic properties in this thesis has done by a vibrating sample magnetometer (VSM), which measures the global magnetic response of the sample under an external applied magnetic field. The VSM [108] is a commonly employed technique in the characterization of all kinds of magnetic samples, ranging from thin films to bulk materials, with sensitivity generally down to the range of 10^{-9} Am^2 (μemu in CGS). The technique is non-destructive, and no sample preparation is needed in general. The schematic of a VSM set-up is shown in fig. 3.6. Sample to be examined is placed in the middle of an applied magnetic field, together with a pair of stationary pick-up coils. By vibrating the sample in a uniform field, the sample is set into relative motion with the pick-up coils and signals (in the form of induced *e.m.f.* according to the Faraday's law) are generated in the pick-up coils due to the presence of the oscillating magnetic flux from the sample. By calibrating the VSM with a known strength of magnetization, absolute values of magnetic moments in the samples along the field direction can be obtained.

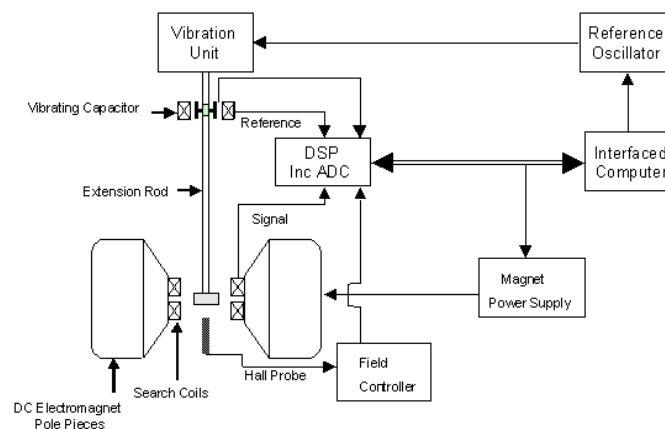


Fig. 3.6 Schematic of VSM setup.

3.7 Characterization: Experimental results

In this section are presented the experimental results of the characterization of the superconductive and magnetic materials employed in the devices developed during the thesis.

3.7.1 Niobium Nitrate

Superconducting devices for SSPD measured in this thesis employed NbN as superconducting materials deposited on MgO (manganite oxide) at the Saitama University (Japan) by means of reactive sputtering. The main deposition conditions are summarized in Tab. 3.1 .

Sputtering Conditions for NbN thin films		
Base Pressure	2×10^{-5}	Pa
Sputtering Gas	Ar(99.999%) N ₂ (99.9999%)	
Ar flow rate	80	SCCM
N ₂ flow rate	1.2~5.1	SCCM
Gas Pressure	0.80~0.93	Pa
Target-Substrate distance	8	cm
Dc power	360	W
Power density	4.59	W/cm ²
Dep. rate	20~40	nm/min
Thickness	2~20	nm

Substrate: MgO(100)
Substrate temperature: ambient temperature

Tab. 3.1

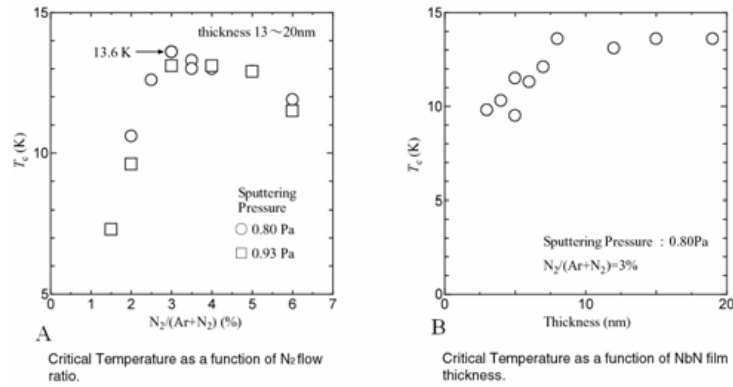


Fig. 3.7 T_c of NbN thin films vs. a) N_2 flow b) thickness.

The NbN critical temperature (T_c) of deposited NbN thin films was found to be very sensitive both to partial N_2 pressure (see fig. 7(a)) and films thickness (see Fig. 3.7(b)). The nitrurization process strictly depends on sputtering gasses pressures, mostly on partial N_2 ratio on Ar+ N_2 mixture. The best quality shows a peak at 13.6K transition temperature for 13-20nm films while less N_2 partial ratio strongly degrade superconductivity properties. It is important to notice the NbN capability to preserve the superconducting state also for thinner structures (around 3 – 4 nm), and this feature makes it a quite unique choice for superconducting materials to be used as photodetectors of single photon, due to the possibility of high density of energy excitation over small structures. Etching of NbN thin films (Japan) was performed by standard RIE procedure assisted using a power of 200W into an evacuation chamber up to 1 pa ($\approx 1.3 \cdot 10^{-5}$ torr) and inert Ar gas flow.

3.7.2 Nickel Copper Alloy

The choice of NiCu as ferromagnetic layer was suggested because it offers a simple capability to tune the magnetic properties by acting on the Ni concentration and a good processability through magnetron sputtering.

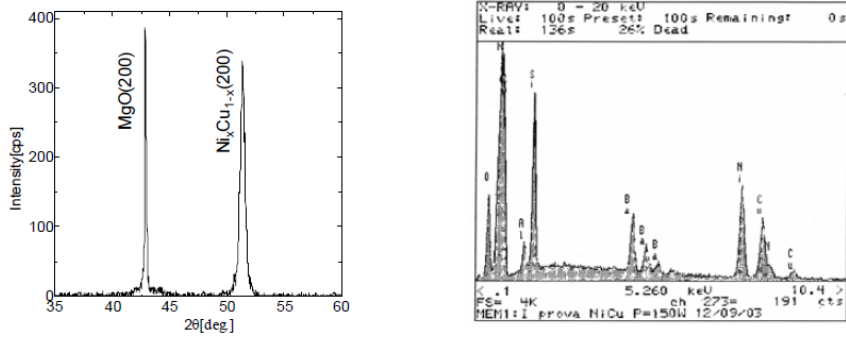


Fig. 3.8 Comparison X-RD analysis Saitama (left)MgO/NiCu and Naples (right)corning/ NiCu.

In Fig. 3.8(left), is shown a XRD $\theta/2\theta$ analysis of a NiCu sputtered sample on MgO at Saitama University (Tab. 3.2): the analysis of the peak position and EDS analysis performed on the same samples, suggested that, in spite of a starting $Ni_{0.5}Cu_{0.5}$ target composition, the stoichiometry is close to $Ni_{0.6}Cu_{0.4}$ while in the case of NiCu samples deposited at University of Naples the composition was close to $Ni_{0.48}Cu_{0.52}$ (Fig. 3.8 right).

Sputtering Conditions for NiCu Films.		
Base pressure	2×10^{-5}	Pa
Sputtering gas	Ar(99.999%)	
Ar flow rate	80	SCCM
Gas pressure	0.93	Pa
Target-substrate distance	8	cm
Dc power	155	W
Power density	1.97	W/cm ²
Substrate Temp.	ambient temperature	
Dep. rate	60	nm/min
Thickness	3~10	nm

Tab. 3.2 : NiCu films on NbN (Saitama Univ.)

3.7.3 NbN/NiCu bilayers

Fig. 3.9 shows a comparison between the R vs. T curves corresponding to several different samples having the same thickness of NbN as base thin film (8 nm). The presence of NiCu produces a decrease of the T_c of deposited bilayers. In this case, we investigated the dependence of the superconducting T_c of the bilayers as a function of the thickness of the magnetic layers. The measurements have been performed dipping slowly the samples in liquid helium (4.2 K).

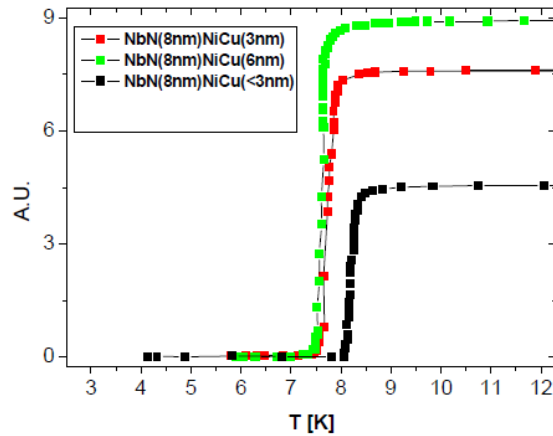


Fig. 3.9 Resistance of NbN/NiCu films versus temperature. Reported graphs refer to three different $\text{Ni}_{0.6}\text{Cu}_{0.4}$ thicknesses, 6nm, 3nm, $\approx 2\text{nm}$.

3.7.4 Permalloy

Starting from target ($\text{Ni}_{80}\text{Fe}_{20}$) thin film of Permalloy has been deposited on Si oxidized (100) (10x10 mm) substrates by magnetron sputtering. During the deposition pressure of Ar gas is around 5 mTorr and the deposition power is set to 200W. The specimens' compositions were verified by EDS end the results are a $\text{Ni}_{84}\text{Fe}_{16}$ alloy. The roughness, measure by AFM, is less than 1 nm. A VSM measurement in plane was performed on a 20 nm thin film (see Fig. 3.10):

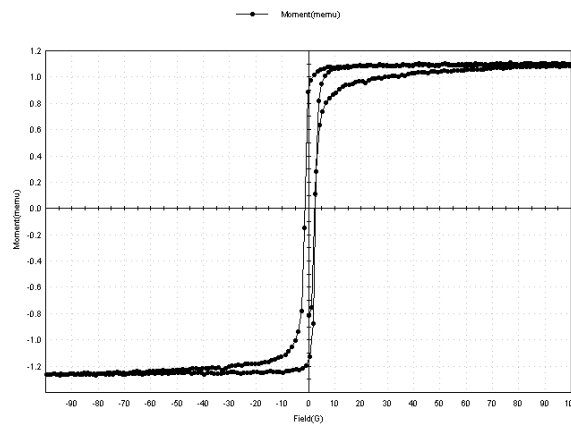


Fig. 3.10 VSM measurement of 20nm thin Py film at room temperature.

From this picture it's possible to obtain that the coercitive field (H_c) for our samples is around 20e (SI 2 mT).

3.8 Devices micro and nano Fabrication

3.8.1 Standard Photolithography

Some deposited films of this thesis were patterned into device structures by using standard photolithographic techniques with ultra-violet (UV) radiation source with resolution of $4\ \mu\text{m}$.

The pattern is transferred from a chromium on fused silica photomask to a polymer film (*resist* Su-8), which allows replication of the pattern in the underlying film. The photomasks can be either positive or negative. In the first case a chemical or physical etching is followed, whereas, in the second case, a lift-off technique is used to achieve the desired structure. Multiple step fabrication processes were carried out by using a *Karl Suss* mask-aligner.

3.8.2 Lift off technique

In the 'lift-off' the pattern is impressed to the photoresist using a negative version of the mask (Fig. 3.11a). After the film is deposited, the material sputtered onto the resist is removed when the resist beneath is dissolved in acetone, leaving the required pattern behind. The rounded resist profile (due to scattering of the radiation, which is greatest near the surface of the photoresist) can be a problem. The film grows up the sides of these rounded resist walls as shown in Fig. 3.12(bottom), forming a continuous layer that peels off when the resist is dissolved.

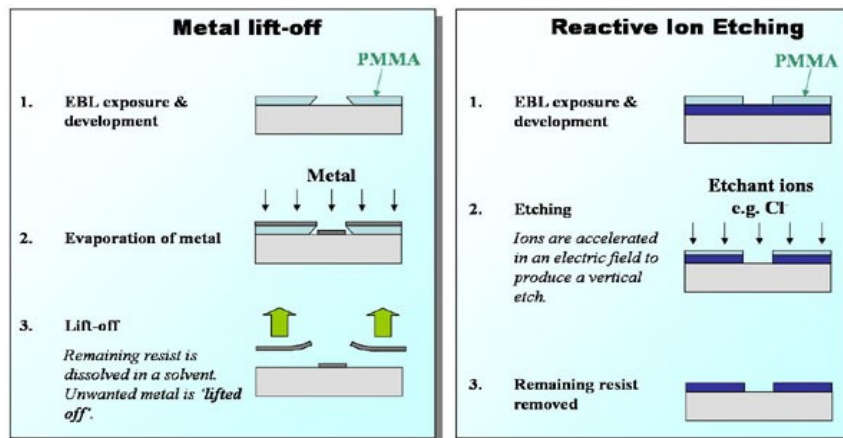


Fig. 3.11 Diagram of a) lift off b) RIE.

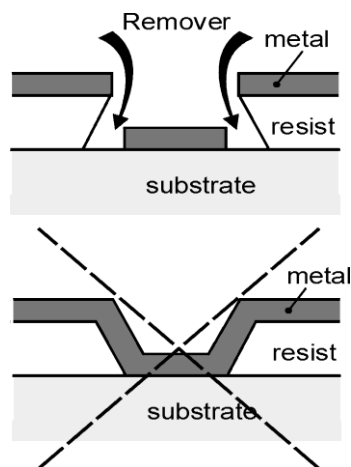


Fig. 3.12 Lift off: undercut (up), rounded resist profile (down).

An easy way to avoid this problem is to use an aspect ratio of resist/metal as large as possible (i.e. 3:1). Another chance is to obtain an undercut resist profile(see Fig. 3.12 up) by using, for example, a double layer resist, an overexposure or overdeveloping process and using low beam energy (in an ebl process see Chapter 1).

3.8.3 Ion Gun

This process is very similar to the sputtering process and, as well as ion-beam sputtering (ion milling) is not a target but the film itself. The sample is posed on negative electrode and it's hit by ions: the motion quantity transferred from ions to superficial atoms of target/sample cause them to be ablated. Typical pressure for this process is 10^{-2} Torr to 10^{-1} Torr; electric field direction is usually orthogonal to target surface thus increasing cutting efficiency and limiting shadows effects, around sample borders, that could (in case of high angle shot) cause resolution problems. Using an ion-gun allows to clean the surface of the film dirty or oxidized during the transition from one deposition system to another and also to define the geometry of a physical device by etching using patterned resist as mask to define the geometry. The etching rates depend on the distance between substrate and source, the cathode current and beam power. A diagram of the principle of operation is shown in Fig. 3.13.

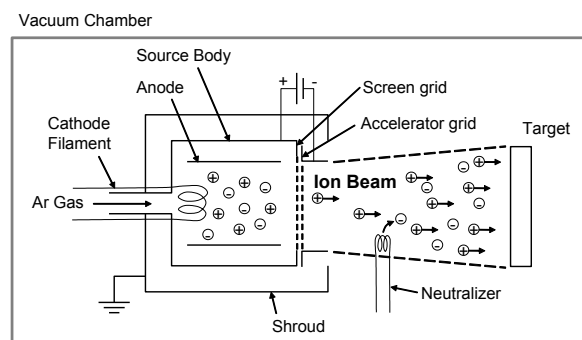


Fig. 3.13 Schematic of ion gun system.



Fig. 3.14 Ion Gun source - University of Naples "Federico II".

3.8.4 Reactive Ion Etching

The reactive ion etching methods has the main vantage of a very high selectivity in terms of material. For the RIE method, instead, the monoatomic noble gas is substituted with a molecular one, so this plasma assisted technique presents a higher ablating speed because the surface is not simply “mechanically” attacked but also “chemically” weakened (see Fig. 3.10b). The anisotropy degree also decreases as ions flux increase. The major advantage of this method is selectivity : using different process gasses it is possible to achieve faster erosions on different materials. This means that one specific gas is used to process one specific material: for example to mill Niobium is used a specific CF_4 and O_2 mixture, where is Flourine that reacts with the target metal. Fig. 3.15 shows a typical RIE system.

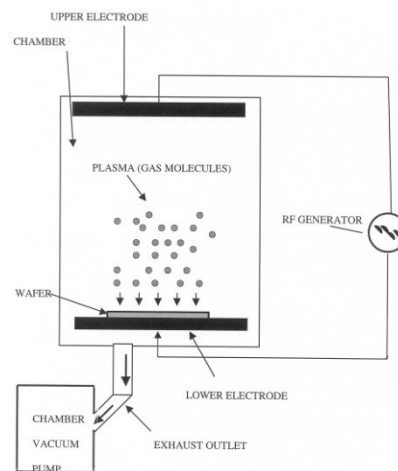


Fig. 3.15 Schematic of a typical RIE system.

3.9 Operative procedures

During this thesis two different technique have been used to obtain the chosen nanostructured pattern. This has been necessary due the different materials employed and the multilayer structures realized in some of the devices. The two different technique are basically differentiated by the removal method of the unwanted resist and material, lift-off of RIE, and consequentially by the employed of two different resist, respectively PMMA or ZEP.

3.9.1 PMMA based lithography

To realized nanowires and nanodots of magnetic materials has been chose the lift off technique because its simplicity process. The first step is to deposit by spin coating a thin layer of PMMA on a SiO_2 (10x10mm). The spin velocity is 3000 rpm x 1 minute and after deposition the PMMA is heated to 170 C° x 30 minutes. The resulting thickness of PMMA is 90nm. In the next step the sample is processed by EBL (acceleration voltage 10keV, aperture $30\ \mu\text{m}$) obtaining a mask profile on the resist fig. the white part is substrate. The metallic layers are deposit using magnetron sputtering for Permalloy or PLD for NiFe and SmCo.

Then the sample is washed with acetone to remove the resist (black part in Fig. 3.16(a)-3.17(a)) obtaining the device (see Fig 3.16(b)-3.17(b)). The details on materials and realized geometric structures will be discussed in the next chapter.

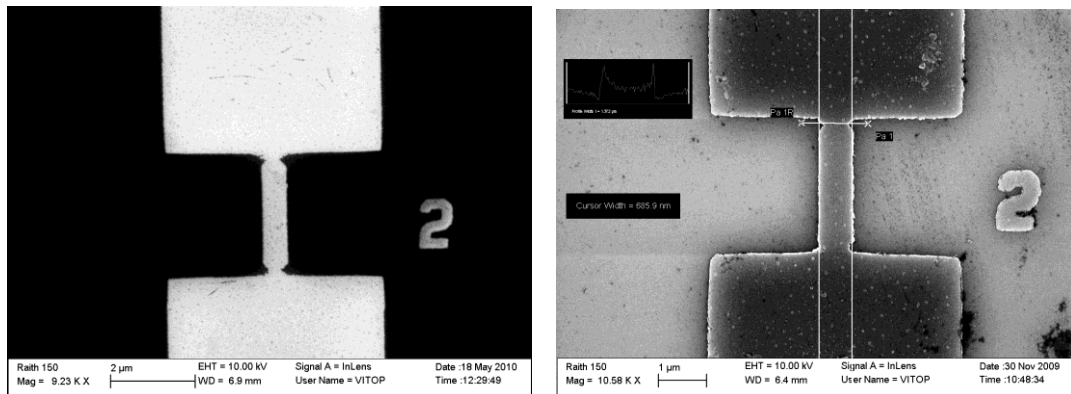


Fig. 3.16 Example of device realized using PMMA: (a) resist mask (b) Py nanowires (sputtering deposition)

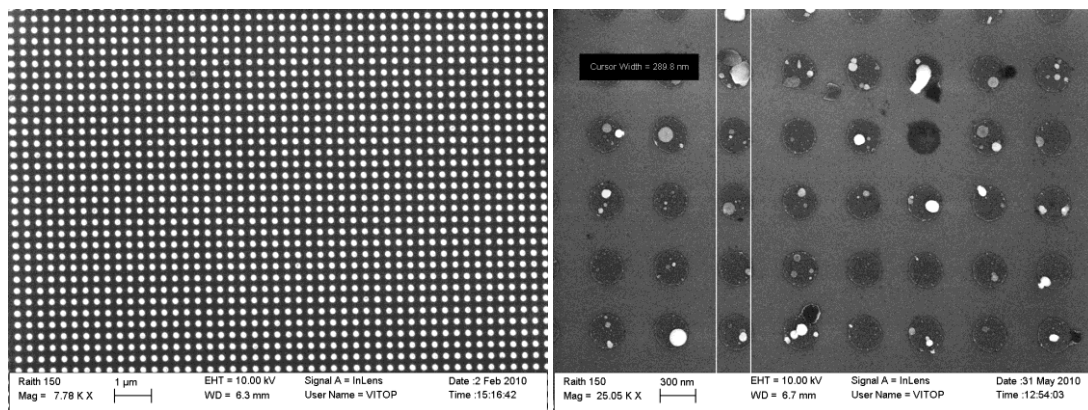


Fig. 3.17 Example of device realized using PMMA: (a) resist mask (b) SmCo nanodots (PLD deposition)

3.9.2 ZEP520 based lithography

The nanowires engineered for SSPD device are constituted by two layers of different materials: Niobium Nitrate (NbN superconductor) and NiCu alloy (magnetic). This bilayers structure is difficult to realize by lift off due to the two different deposition processes. In that case it proceeds depositing by magnetron sputtering NbN on MgO substrate and then NiCu. Over this bylayer is deposit ZEP520 by spin coating (300nm thick) and then the sample is processed by EBL (acceleration voltage 20keV, aperture 10 μm). Once developed the resist, the sample's geometry is definite by RIE that removes the NbN/NiCu not covered by ZEP (see Fig. 3.18). Also in this case the details on materials and realized geometric structures will be discussed in the next chapter.

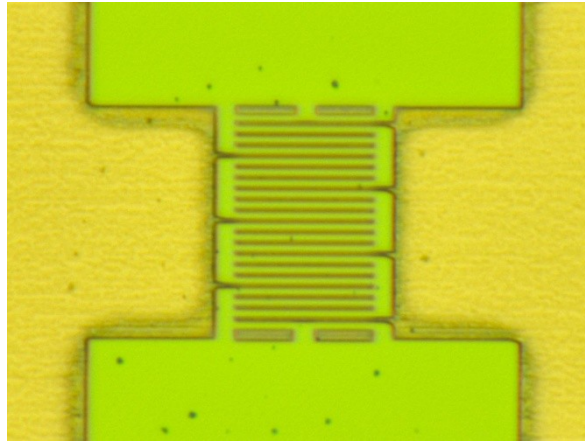


Fig. 3.18 Example of nanowires in meander configuration realized using ZEP.

References

- [105] D. Perez, L. J. Lewis, M. Meunier, Thermodynamic pathways to melting, ablation, and solidification in absorbing solids under pulsed laser irradiation, *Phys Rev. B*, 73 (2006) 134108
- [106] A. R. West, *Solid State Chemistry and its Applications*, John Wiley & Sons (1985).
- [107] G. Binnig, C. F. Quate, Ch. Gerber, *Atomic force microscope*, *Phys. Rev. Lett.*, 56 (1986) 930
- [108] S. Foner, *IEEE Trans. Magn.* 17, 3358 (1981)

Chapter 4: Results and discussions

4.1 NiCu/NbN superconducting nanostripes for optical detection

4.1.1 Motivation

As discussed in Chapter 2, the highest performances SSPDs use ultrathin films of NbN, although other superconducting materials have been proposed [109,110]. One of the most important parameters to be maximized for detector applications is the critical current density J_c of the nanostripe that works as sensing element. This is particularly evident in SSPDs, typically in a form of a meander (up to 0.5 mm length), ultrathin (~ 4 nm thickness) and very narrow (~ 100 – 200 nm) superconducting stripe, in which the detection efficiency is an exponentially increasing function of the bias current I_b , which is limited by J_c [111]. The best ultrathin NbN films deposited at high temperatures resulted in $J_c \sim 6$ – 7 MA/cm² at 4.2 K, which means a maximum possible I_b of about 30 μ A in a meander configuration [112]. In practice, I_b is additionally reduced by the stripe patterning process and substrate roughness. Accordingly it 's very important to investigate all possibilities of modifying superconducting nanostripes in order to enhance the J_c . A possibility is that using hybrid ferromagnet/superconductor (F/S) bilayer, which are also of great interest for several fundamental and applied experiments [113]. The use of a F/S nanostructure with flux pinning centers can lead to increased of J_c , as recently observed in NiCu/Nb bilayers [114].

4.1.2 Fabrication process

During this thesis several nanowire has been realized also in collaboration with the Graduate School of Science and Engineering, "Saitama University" (Japan). A typical patterned configuration is proposed in Fig. 4.1.1.

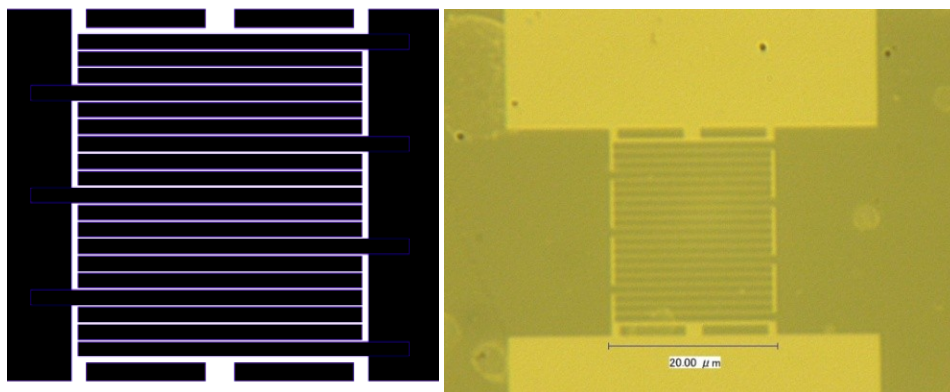


Fig. 4.1.1 Patterned meander structure: it is a configuration of 3 parallel by 6 series stripes. Inner stripes thicknesses can vary from 150 to 500 nm in width. (right) microscopy image, (left) CAD drawing.

The patterned geometries of samples used in photoresponse experiments had a meander shape made of three parallel stripes (block) connected in series of six blocks. Such a configuration has been implemented for to improving the quantum efficiency of resulting photodetectors since the overall area is increased (see meander geometry). Moreover, the parallel configuration has been demonstrated to generate an intrinsic amplitude gain mechanism during the working operation after the phonon absorption [115]. In fact, in a parallel SSPD all wires are biased with a current slightly below their critical current, in the same way as for a single meander SSPD. When the photon absorption induces a transition to the normal state in one nanowire, the current that was flowing in the nanowire is redistributed through the other parallel nanowires and the load. To properly trigger the cascade switch of all the parallel nanowires, it is necessary to confine the currents in the parallel nanowires at this stage. This can be achieved by inserting an inductance in series with the block of parallel nanowires to confine the current during the redistribution. The presence of the in series inductance is important for reliable triggering of the cascade switch mechanism. Meander structures have been patterned at the end of a planar wave-guide of 50Ω characteristic impedance: this feature is very important to achieve an optimal coupling between the detectors and the readout cable since the front end electronics operates at high frequencies (up to 2 GHz). NbN thin films (8 nm) were deposited at room temperature on MgO (100) substrates by dc-magnetron sputtering (see Chapter 3) [116], and exhibited a critical temperature $T_c=9.8$ K and a residual resistivity ratio $\rho_{300\text{ K}}/\rho_{20\text{ K}}=0.98$. For F/S structures, a $\text{Ni}_{0.6}\text{Cu}_{0.4}$ overlayer was *in situ* deposited by dc-magnetron sputtering at an Ar gas flow of $80 \text{ cm}^3/\text{min}$ (Ar pressure of 7 mTorr), and a dc power of 155 W. The final NiCu (3nm)/NbN (8 nm) bilayers exhibited $T_c=7.8$ K, with no further T_c degradation observed for structures with NiCu even as thick as 6 or 10 nm (see Chapter 3 Fig. XXX). As deposited ultrathin films were patterned by EBL (10kV on ZEP resist) and RIE etching (CF_4+Ar) into meander-type structures with linewidths ranging from $w=150$ to 500 nm. A common ground plate and contacting pads were realized by sputtering NiCu by a proper mask on the last part of the lines where easy bonding by aluminum wires was archived. A second step of photoresist spinning and normal photolithographic procedure (exposition at UV lamps through a Cr mask) is used to define NiCu bulk contacts by lift-off procedure.

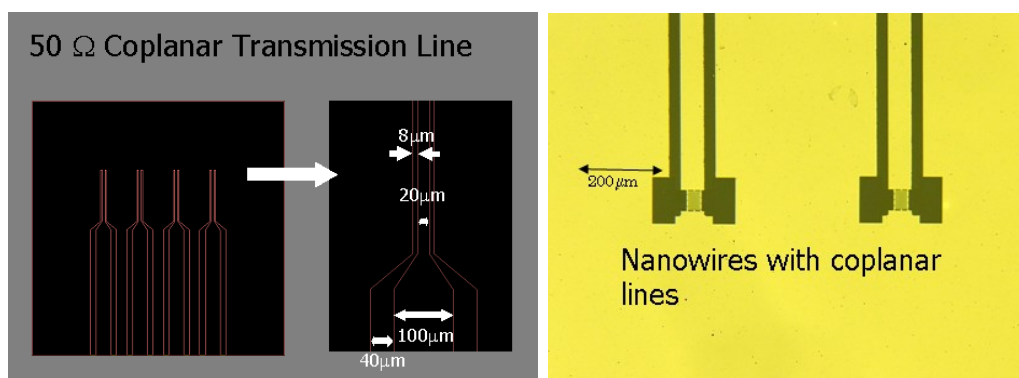


Fig. 4.1.2 a) Particular of CAD design of main patterns and meander disposition on the sample b) Microscopy image of the meander structure.

4.1.3 Experimental

All the measurements have been performed in a cryo-system based by a the cold finger cooled in a He-flow cryostat. The high vacuum ($P \approx 10^{-6}$ torr) request to cool the system war reached by diffusive pump. Then, the liquid Helium is transferred to the cryostat through a transfer tube, insulated at $P < 10^{-5}$ Torr respect the environment. The flow is controlled by a spin-valve and by a rotary-pump. Temperature is measured by a proper electronics able to directly power an heater connected to the cold finger, where a thermometer is positioned to feedback the loop control. Moreover, the feedback line is connected also to a step motor control of the spin valve. The working scheme is shown in Fig. 4.1.3(a).

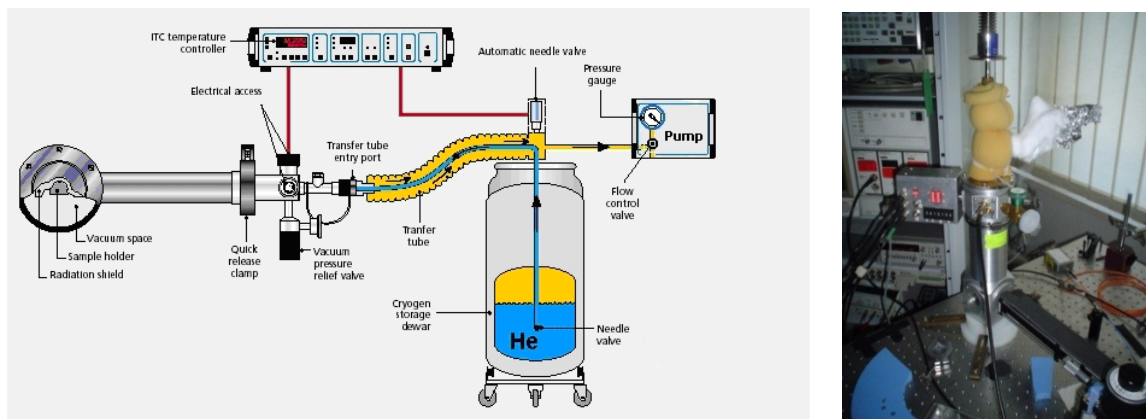


Fig. 4.1.3 a) Scheme of experimental setup for cryogenic measurements b) Cryostat at ICB-CNR.

The experimental setup for time-resolved photoresponse measurements includes two different laser-diode able to generated a train of 10 ns long, 10 MHz repetition rate, 850 or 1550 nm wavelength and fluence $\Phi = 1 \times 10^{-10}$ J/cm² or $\Phi = 3 \times 10^{-8}$ J/cm² respectively. Our samples were placed inside the optical, continues-flow He cryostat and our read out setup consisted of two cascaded *rf* amplifiers and a digital oscilloscope (LeCroy) with the overall time-resolution of 355 ps. A diagram of experimental setup is sketched in Fig. 4.1.4:

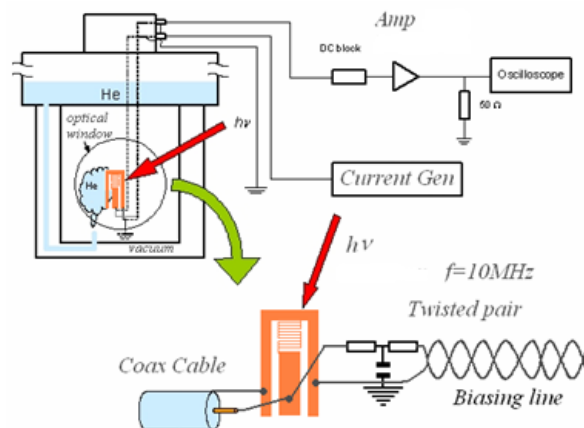


Fig. 4.1.4 Photoimpedance measurement setup.

Fig. 4.1.5 shows the current voltage I - V characteristics, measured at 4.7 K, of two segmented-meander devices with $w=150$ nm: the first refers to a pure, 8 nm thick NbN film and the second to the NiCu (3 nm)/NbN(8 nm) bilayer. We note that the presence of the NiCu overlayer results in a significantly larger value of the critical current I_c of the second device, and the values as obtained from Fig. 4.1.5 are $I_c^{\text{NbN}}=8.0$ μA and $I_c^{\text{NiCu/NbN}}=72$ μA , respectively. The I_c^{NbN} is strongly affected by the fluctuation phenomena and the 8.0 μA value is a conservative, upper-limit estimation, whereas observation of the phase-slip-center structure on the NiCu/NbN I - V characteristics indicates a fully proximitized F/S bilayer [117]. The relative J_c -enhancement Δj_c , defined as:

$$\Delta j_c = \frac{(j_c^{\text{NiCu/NbN}} - j_c^{\text{NbN}})}{j_c^{\text{NbN}}} \quad (4.1.1)$$

was found 5.5 at $T/T_c=0.6$, and $J_c^{\text{NiCu/NbN}}=4.4$ MA/cm^2 . The normal-state resistances for the NbN and NiCu/NbN meanders were 91 k Ω and 59 k Ω , respectively.

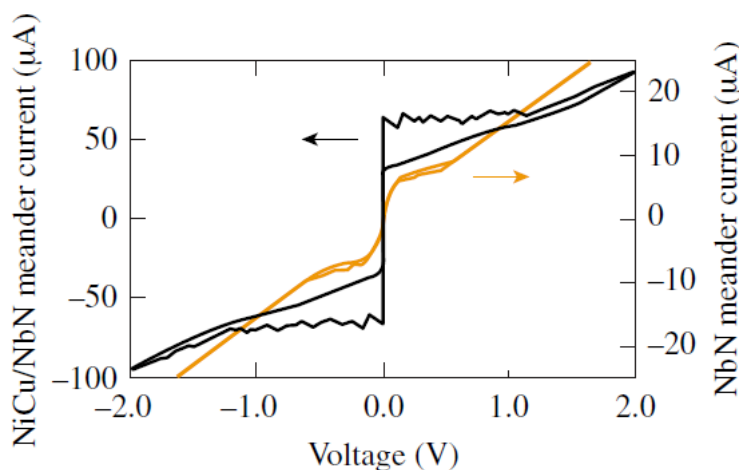


Fig. 4.1.5 Current-voltage characteristics of NiCu(3 nm)/NbN(8 nm) (closed circles) and NbN(8 nm) (closed squares) nanostructures measured ($w=150$) at 4.7 K. Note that the current vertical scales are different.

Several NiCu/NbN meanders were tested and the a J_c -enhancement was also confirmed. All measurements, at $T =4.2$ K with $T/T_c=0.54$, are showed in Fig. 4.1.6. We observe that J_c^{NbN} increases with the stripe width increase in an identical way of others older samples realized and tested at the “Saitama University” [116]. It is important to note that the $J_c^{\text{NiCu/NbN}}$ functional dependence as shown in Fig. 4.1.6 is roughly the same as that of J_c^{NbN} but simply shifted upwards in the direction of higher J_c values. This strongly indicates that the J_c degradation for our narrowest NbN and NiCu/NbN nanostructures must be directly related to our meander patterning process, and the J_c -enhancement due to the presence of the NiCu layer on top of NbN is, up to the lowest approximation, independent of the nanostructure width. Simultaneously, the Δj_c factor itself is a strong function of nanowire width, because the J_c increase is normalized to very different base values of J_c^{NbN} . As a result, the J_c -enhancement is the most pronounced for our narrowest, 150 nm wide, nanostructures with $\Delta j_c=7.1$ at $T/T_c=0.54$.

The latter carries important practical implication for optical detectors based on superconducting nanostructured meanders.

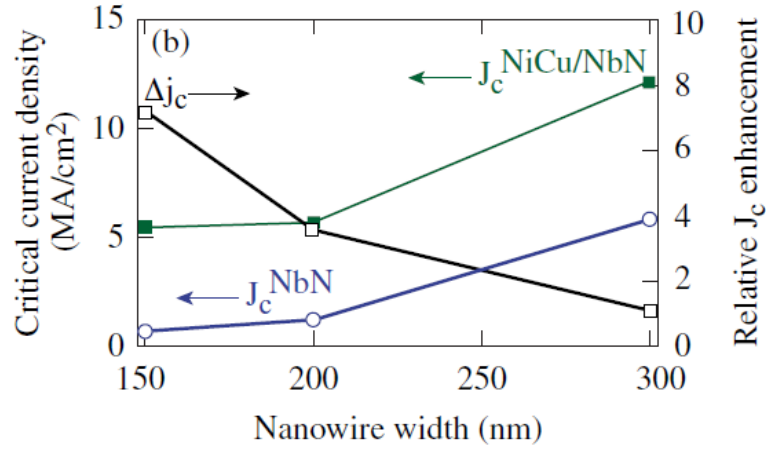


Fig. 4.1.6 Critical current dependence on the nominal nanostripe width for both the pure NbN(8 nm) and NiCu(3 nm)/NbN(8 nm) segmented meanders. Temperature was 4.2 K.

Tested superconducting stripes are in the two-dimensional (2D) limit since their thickness $d=11$ nm is comparable to the coherence length ξ , moreover the “Likharev’s limit” (see Chapter 2.1) for penetration of magnetic vortices is satisfied, and, simultaneously, w ’s are much narrower than the effective magnetic penetration depth $\lambda_{\text{eff}}=\lambda^2/d$. The 2D regime, as a first approximation, guarantees for a homogeneous distribution of the supercurrent over the cross-section of nanostripes. According to the three- J_c model developed by Il’in [118] and Engel [119], we should be in the limit: $J_c^{\text{pen}} < J_c^{\text{pin}} < J_c^{\text{G-L}}$, here J_c^{pen} is the current density that causes a self-field at the stripe edge large enough for penetration of vortices, J_c^{pin} is the depinning critical current density, at which the Lorentz force acting on vortices exceeds the pinning force, and $J_c^{\text{G-L}}$ the Ginzburg–Landau depairing critical current density, respectively. In our superconducting F/S nanostripes, the diffusion of F atoms into the F/S interface region, and thus the high concentration of pinning centers, increase the vortex pinning, as well as the presence of magnetic domain walls in the NiCu layer [120]. Thus, the experimentally observed, enhanced J_c values in NiCu/ NbN nanostripes are actually limited by the enhanced J_c^{pin} . It’s possible to confirm that the NiCu overlayer is responsible for the increase in the concentration and strength of the pinning centers in the NbN base layer (or, rather, in proximitized NiCu/NbN bilayer) [121]. The idea is to look for the increase in the polarizability ϵ_{BKT} of the vortices and to measure the temperature dependence of the resistance $R(T)$ of tested meander devices close to the superconducting transition region. The experimental results of a 300 nm width meander are shown in Fig. 4.1.7.

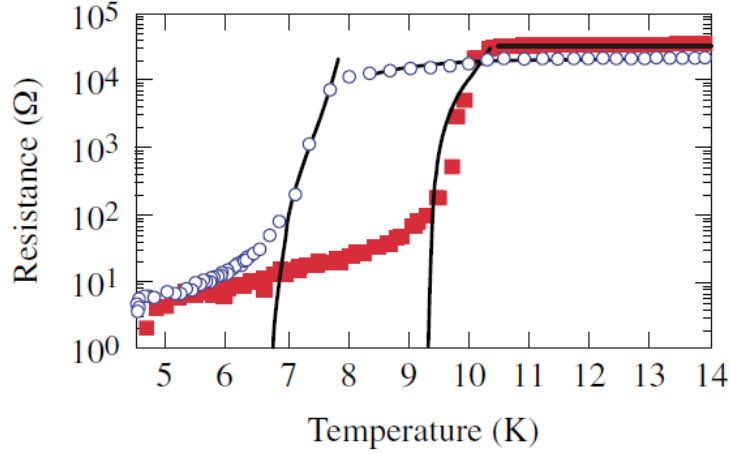


Fig. 4.1.7 Resistance vs temperature characteristics of our NiCu(3 nm)/NbN(8 nm) (open circles) and NbN(8 nm) (closed squares) nanostructures. The solid lines are the result of the fitting procedure [122] used to extract T_{BKT} .

We note that both $R(T)$ dependences are typical of 2D superconducting stripes, where BKT transition can be addressed (see Chapter 2). We have extracted the characteristic temperature T_{BKT} of such a phase transition by fitting: T_{BKT} reduces from 9.5 K in the case of sole pure NbN to 6.5 K for NiCu/NbN bilayer. Since the measured critical temperature T_{C} of the bilayer is also reduced with respect to pure NbN, we evaluated independently for both samples the following ratio [121]:

$$\frac{T_{\text{BKT}}}{T_{\text{C}}(0)} = \frac{1}{1 + 0.173 \frac{\epsilon_{\text{BKT}}}{\pi} R_{\text{SN}} \frac{2e^2}{h}} \quad (4.1.2)$$

where R_{SN} is the sheet resistance and is equal to 220 Ω/square and 340 Ω/square for our NiCu/NbN samples, respectively. From Fig. 4.1.7, we obtained the following values for the $T_{\text{BKT}}/T_{\text{C}}$ ratios: 0.83 and 0.97, for NiCu/NbN and NbN nanostructures, respectively. The presence of the NiCu overlayer on the 300 nm wide ultrathin NbN stripe increases BKT up to a factor of 10. For the 200 nm wide meander, the calculated BKT-enhancement was 11. Such large increase in BKT confirms the very active role of vortex pinning forces in our NiCu/NbN nanostructures, which brings to the significant increase of $J_{\text{C}}^{\text{pin}}$ observed in these structures.

4.1.4 Time-resolved photoresponse measurements

We have also performed time-resolved photoresponse measurements. Fig. 4.1.8 shows the photoimpedance on a NbN(8 nm)/NiCu(3 nm) meander structure with a linewidth of 150nm. The effect of both wavelengths (850 nm and 1550 nm) and duty pulses is shown.

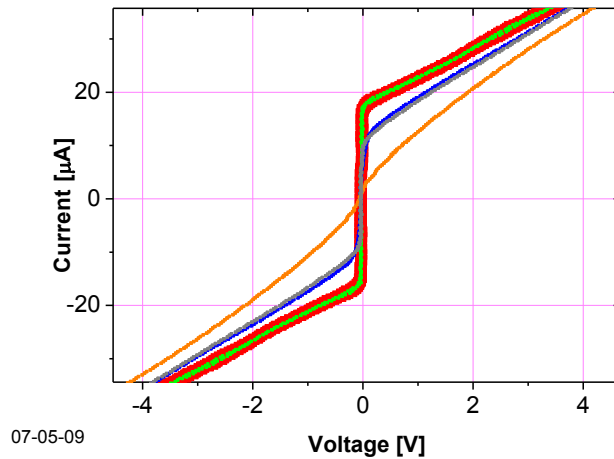


Fig. 4.1.8 Laser effects on IV curves of a meander shaped device NbN(8 nm)/ Ni_{0.60}Cu_{0.40}(3 nm) based, bridge line width 150 nm, 6 series by 3 parallel bridges at 4.7K; device's $I_c=17.5 \mu\text{A}$; $R_{nn}=24.7\text{K}\Omega$; red curve is without laser ; green is with diode generated laser by carrier wavelength $\lambda_{\text{LASER}}=850 \text{ nm}$; blue continuous laser $\lambda_{\text{LASER}}=1550 \text{ nm}$; orange laser pulsed 20 ns duration laser $\lambda_{\text{LASER}}=1550 \text{ nm}$; grey laser pulsed 6.5ns duration $\lambda_{\text{LASER}}=1550 \text{ nm}$.

The $\lambda=850\text{nm}$ laser irradiation didn't affect the IV curves seriously, while the infrared laser ($\lambda=1550\text{nm}$) modified the curve shapes, producing lower critical currents. The incident power has been calculated to be below $1 \text{ nJ}/\text{cm}^2$. In Table 4.1.1 the filling factors [123,124] of measured devices corresponding to line widths ranging from 150 nm to 500 nm are summarized.

Line Width	Area	Filling Factor
150 nm	$3 \mu\text{m}^2$	0.18
200 nm	$4 \mu\text{m}^2$	0.23
300 nm	$6 \mu\text{m}^2$	0.27
400 nm	$8 \mu\text{m}^2$	0.41
500 nm	$10 \mu\text{m}^2$	0.5

Tab. 4.1.1 Filling factors of measured meander devices with a total area of $20 \times 20 \mu\text{m}^2$ and lateral connections with area $6 \times (20/3) \mu\text{m} \times 500\text{nm} = 20 \mu\text{m}^2$

The previous table has been inserted to evidence a dependence of measured photoresponses in low filling factor devices and EM coupling (e.g. 150 nm), from the fluence of the lasers but not from the wavelength. In the following experimental results concerning the photoresponse of fabricated superconducting detectors are presented even if single photon counting regime has been not archived. Fig. 4.1.9 shows the resulting transients obtained when NbN and NiCu/NbN detectors were current-biased at $I_b/I_c^{\text{NbN}}=0.84$ and $I_b/I_c^{\text{NiCu/NbN}}=0.60$, respectively. The inset in Fig. 4.1.9 shows the same photoresponse transients normalized but on an zoomed time scale.

It's possible to note that both signals are identical and limited by our 10 ns long optical excitation pulses (except for a substantially larger noise level of the NbN-detector transient). We didn't observe any broadening of the NiCu/NbN detector transient, which should indicate an increased λ_{eff} in the F/S bilayer. Based on the temporal shapes of our signals, we can conclude that the photoresponse follows the equilibrium inductive kinetic effect [125] and thus, the amplitudes of the transients should scale with the nanostripe J_C , as V_{kin} voltage is directly proportional to I_b . As confirmation, we observed that the V_{kin} ratio taken directly from the data in Fig. 4.1.9 is equal to 6.1. Since the difference in the biasing conditions between the NbN and NiCu/NbN photodetectors was intended to compensate the slight difference in thicknesses (11 nm versus 8 nm) of the nanostripes, we observe that (within the experimental error) the $V_{\text{kin}}^{\text{NiCu/NbN}}/V_{\text{kin}}^{\text{NbN}}$ ratio is exactly equal to the $J_C^{\text{NiCu/NbN}}/J_C^{\text{NbN}}$ ratio.

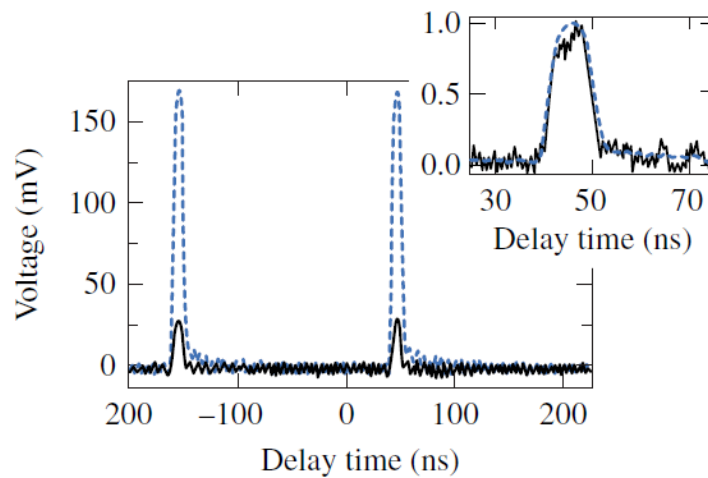


Fig. 4.1.9 Photoresponse transients of NiCu(3 nm)/NbN(8 nm) (dashed line) and NbN(8 nm) (solid line) segmented-meander detectors collected at 4.7 K. The inset shows the normalized pulses, confirming that the time-domain photoresponse dynamics was the same in both cases.

4.2 Permalloy planar spin-valves

4.2.1 Motivation

The effect of DWs on the transport properties of ferromagnet nanostructures is a topic of great interest. Moreover systems in which the magnetic configuration is defined by domains separated by DWs are promising for digital applications [126,127,128]. In ferromagnetic nanostructures an experimental goal is to use magnetoresistance to investigate DW nucleation and dynamics. Novel GMR geometries including nanocontacts can be grouped in two main families. In the first, two sharpened wires were brought into contact. A magnetic field is applied along the common axis of the two wires by two separate coils which are able to produce different fields in different directions in one of the two wires. The resistance increases when the field applied to the two wires has the opposite direction, presumably trapping a domain wall at the nanocontact region. The second family consists of a sharpened wire touching the surface of another wire perpendicular to it.

In this case an increased resistance is observed when the magnetic field is applied along the axis of the first wire causing the magnetization of the two wires to be perpendicular to each other due to shape anisotropy. In this case a domain wall is also presumed to be formed in the nanocontact region. Such experiments demonstrate the possibility the conductance changes might be due to effects related to the formation of domain walls at geometrically reduced zones. From a theoretical point of view, it has been demonstrated that the anisotropy of the contact can pin the domain wall in the contact [77] also in a quite reduced size of the nanocontact. This is important because the electrons traveling through a wide domain wall in which neighboring atomic moments are nearly parallel experience very weak scattering, while electrons passing through a narrow, abrupt wall cannot adjust to the sharp change of magnetization, and experience increased reflection. It is, however, very difficult to obtain analytical results for realistic nanocontacts because of the difficulty of taking into account the crucial aspects of the electronic structure in the vicinity of the nanocontact. It is important to notice that the interest for studying the interplay between electron transport properties and a magnetic object such as the magnetization or the DW is interest also for other reasons which lie in the influence by quantum fluctuation on the the magnetization or the motion of a DW In a mesoscopic system. In this Chapter several configurations are proposed for studying the formation and the control of domain walls presumably formed at realized nanoconstrictions down to 70nm widths.

4.2.2 Fabrication process

Magnetic nanostructures has been fabricated on oxidized Si (100) substrates, after an EBL patterning of desired geometries. The EBL patterns were drawn on a 90 nm PMMA resist film; an example of PMMA mask is shown in Fig. 4.2.1. After the development, thin films of Py, 50 or 20 nm were deposited by magnetron sputtering without any heating of the substrate (see Fig. 4.2.2). After the deposition liftoff process in an acetone bath was used to remove photoresist.

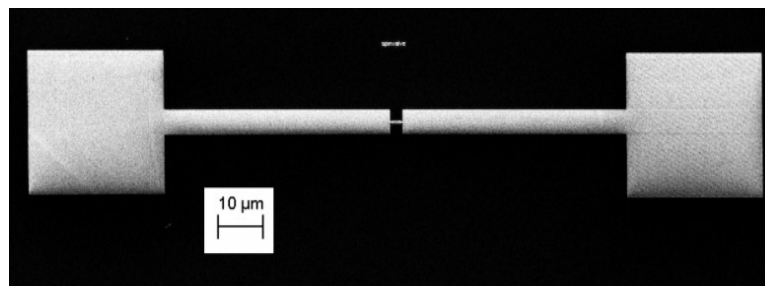


Fig. 4.2.1 SEM image of PMMA mask for a nanostructured magnetic nanowire.

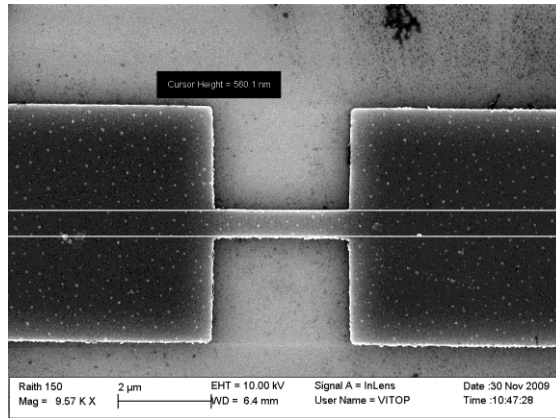


Fig. 4.2.2 ZSEM images of Py nanowire 3 μm long and 500 nm wide.

Different geometries have been realized in order to test the MR response after the nucleation of DWs trapped in geometrically controlled constrictions, and their switching due to external magnetic field and injection current.

4.2.3 Experimental

MR measurement basically detect the changes of the device resistance after the application of an external magnetic field (H_o), which can varies both in intensity and direction. H_o was provided by a pair of Helmholtz coils driven by a Sourcemeater (Keithley 2425) up to 3 A corresponding in a maximum applied field of about 0.1 T. The device resistance was measured by a Multimeter (Keithley 2400) in a 4 point configuration, while all instruments were controlled by a Lab View software. Samples were mounted on a copper holder which allows a good temperature stabilization in low temperature measurements (down to liquid Helium 4.2 K). A schematize of the experimental setup is shown in Fig. 4.2.3.

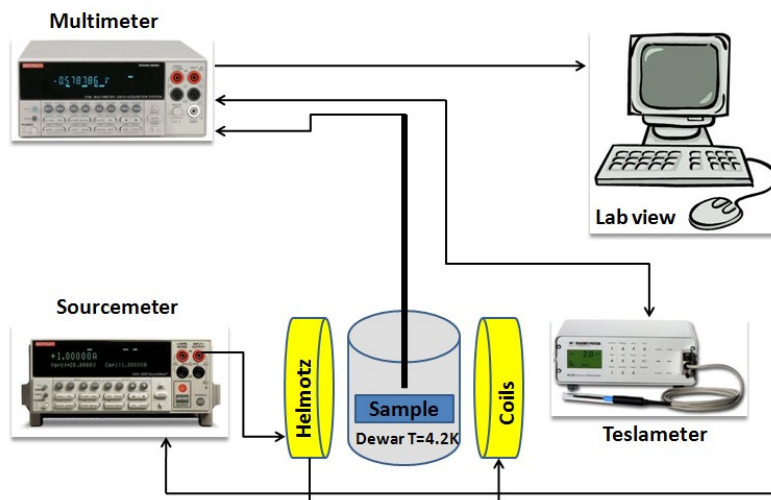


Fig. 4.2.3 Scheme of experimental setup.

The $R(H_a)$ curve for a 20 nm, not patterned, Py thin film was measured as a test case. Measurements were performed in two different configurations: in the first case (see Fig. 4.2.4(a)) the magnetic field was applied parallel to the bias current ($I_b=100 \mu\text{A}$), while in the second perpendicularly (see Fig. 4.2.4(b)). The AMR effect clearly rules the observed phenomenology, leading to a $\Delta R/R_{||}=0.30 \%$ and $\Delta R/R_{\perp}=0.33\%$ for parallel and perpendicular configuration respectively.

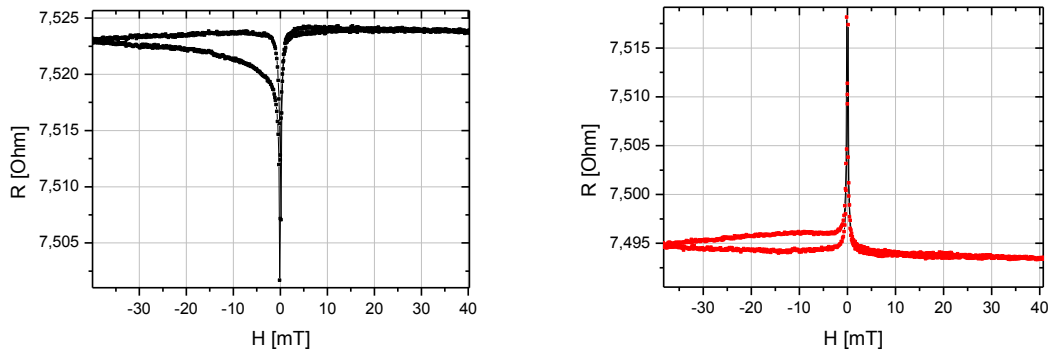


Fig. 4.2.4 a) MR measurement for $I_b \parallel H$ | b) MR measurement for $I_b \perp H$

4.2.4 MR measurements

The geometric configuration of the first series of samples is shown in Fig. 4.2.1. On the PMMA mask 90nm thin was deposited 50 nm thin Py.

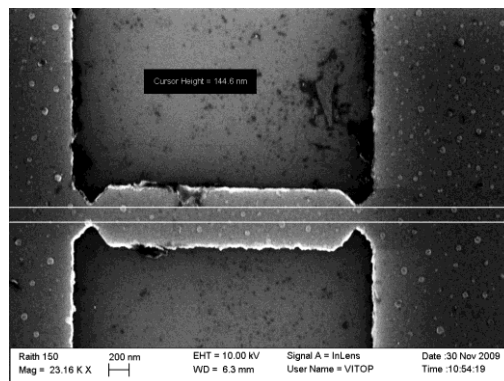


Fig. 4.2.5 SEM images of Py nanowire 3 μm long and 500 nm wide with two 150 nm constrictions.

We realized two different in-line 3 μm long nanowire (ILN) characterized by 500 nm width and, in for the latter configuration, 150 nm wide constrictions (see Fig. 4.2.2 and Fig. 4.2.5 respectively). A MR measurement for an ILN without the constrictions, at $T=300 \text{ K}$, is shown in Fig. 4.2.6.

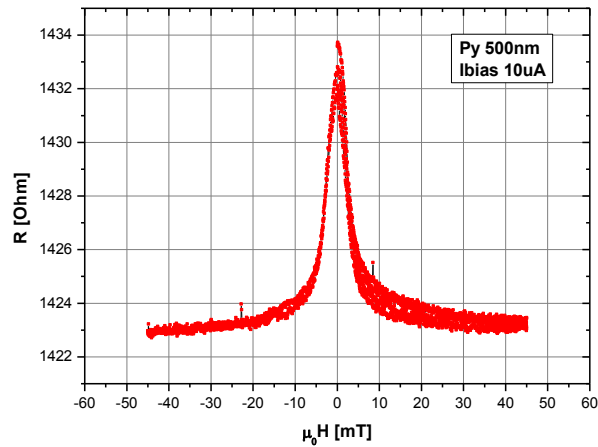


Fig. 4.2.6 MR measurement of Py nanowire 500nm wide.

The bias current was $I_b=10 \mu\text{A}$ and it was applied in the same direction of the applied magnetic field (H_a). The shape anisotropy forces vector magnetization \mathbf{M} to lay in the film plane along the wire direction. The parabolic behavior can be explained according to Eq. 2.2.73 in terms of AMR effect: in the limit of $H_a \ll H_d$ is possible to rewrite Eq. 2.2.78 as:

$$\rho(H) = \rho_{\perp} + \Delta\rho \left[1 - \left(\frac{H_a}{H_d} \right)^2 \right] \quad (4.2.1)$$

The R vs. H shows clearly a parabolic behavior on field range in agreement with the previous limit. The MR ratio was measured to be 0.77%. Sample containing two constrictions were measured under the same experimental conditions. A comparison between the two configurations is shown in Fig. 4.2.7:

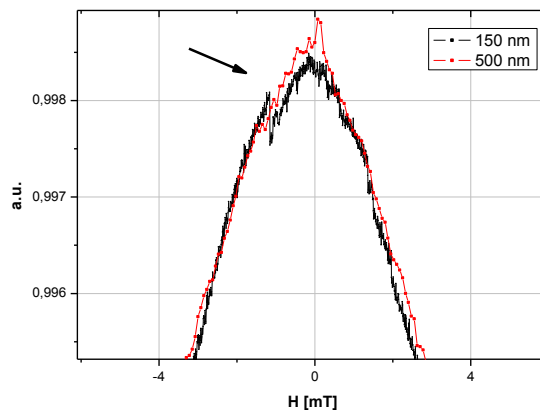


Fig. 4.2.7 Comparison between the two nanowires configurations. Note the measures were normalized to max value.

The two devices showed the same background parabolic behavior except for a some resistance steps occurring in the device with nanoconstrictions when the magnetic field is decreased from the positive saturation until a negative value of about 3 mT.

A possible explanation can be the following: when $H_a \rightarrow 0$ T from positive values, due to the presence of nanoconstrictions along the nanowire, the vector magnetization \mathbf{M} cannot continuously align with the field direction, and hence one or more domains (and consequently DWs) should be formed. Accordingly, the overall resistance in 150 nm device is slightly larger than the 500 nm (no constrictions) sample, and features resembling steps are clearly observable. When H_a increases in the opposite negative direction, \mathbf{M} starts to rotate, forming a misorientation angle with the bias current I_b , and an AMR behavior is observed as expected. Nevertheless, in the case of Py, $\rho_{\parallel} > \rho_{\perp}$, and thus from eq. 4.2.1 a negative contribution to the MR is expected when $H_a \sim -1.1$ mT, \mathbf{M} is aligned completely to the applied field, and the clear observed sharp step should correspond to an expulsion of domain wall(s) which were previously formed. In other words, the rotation of \mathbf{M} is not gradual, since the shape anisotropy of the device now localizes and pins the domain walls, resulting in an abrupt change of resistance when they are annihilated, and \mathbf{M} realigns with the driven field. The MR ratio, as evaluated according to eq. 2.2.74 in Chapt. 2, was found to be $\sim 0.04\%$. MR measurements on sample containing two 150nm constrictions have been performed at different angles between the bias current and applied magnetic field. Results are summarized in Fig. 4.2.8. The recorded behavior confirms the AMR nature of the MR background in our experimental results.

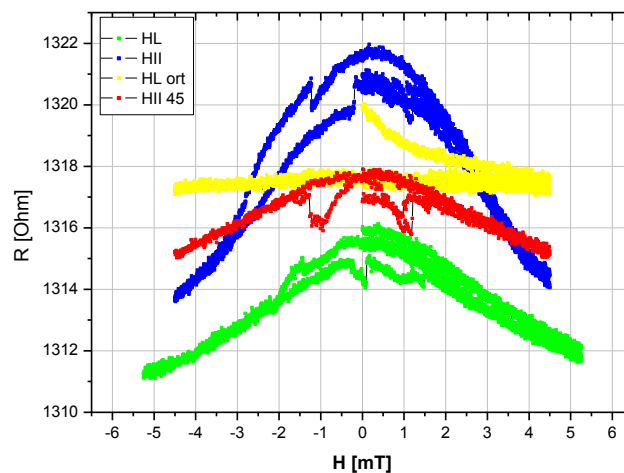


Fig. 4.2.8 Confront of MR: nanowires 3 μm long and 500 nm wide with two 150 nm wide constrictions, at different H_a direction.

When H_a is perpendicular to I_b , the MR jumps became quite smaller (see green curve in Fig. 4.2.8): \mathbf{M} cannot rotate and follow the field's direction due to shape anisotropy, and it remains aligned with the initial nanowire direction producing no significant changes in magnetoresistance. We cannot exclude the presence of DWs influencing the observed MR response, but such a hypothesis should be confirmed by some MFM or other imaging techniques, which were unavailable during this thesis. The yellow curve represents the MR when H_a was applied orthogonally to the film plane. It can be noticed how, neglecting the initial behavior due to the residual \mathbf{M} , no MR was observed.

This is probably the effect of a Néel wall configuration although a C-Bloch wall configuration for such thickness of Py is possible (see chap. 2). Devices characterized by smaller widths of nanoconstrictions were realized down to 70nm: smaller is the size of the constriction, higher confined is the pinning of the domain wall, and larger is the expected MR change (see Chapt. 2). Moreover, the Py thickness was also reduced down to 20 nm for enhancing the role of surface energy in pinning DWs, that we believe to be of Néel type according to Fig. 2.2.6. A photograph and a SEM picture of the new geometrical configuration are proposed in Fig. 4.2.9. In the following such a configuration will be named “right contacts nanowires” (RCN).

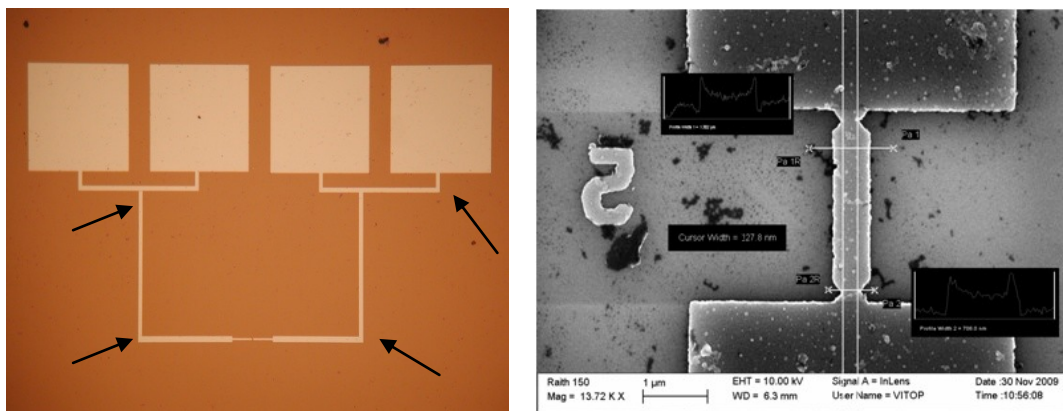


Fig. 4.2.9 Images of: a) device pattern 20 nm thin b) (SEM) zoomed nanowire 3 μm long and 500 nm wide with two 100 nm wide constrictions.

The MR measurement when the external magnetic field H_o is applied parallel to the nanowires is shown in Fig. 4.2.10(a), while Fig. 4.2.10(b) shows a magnification of the field region around $H_a=0$.

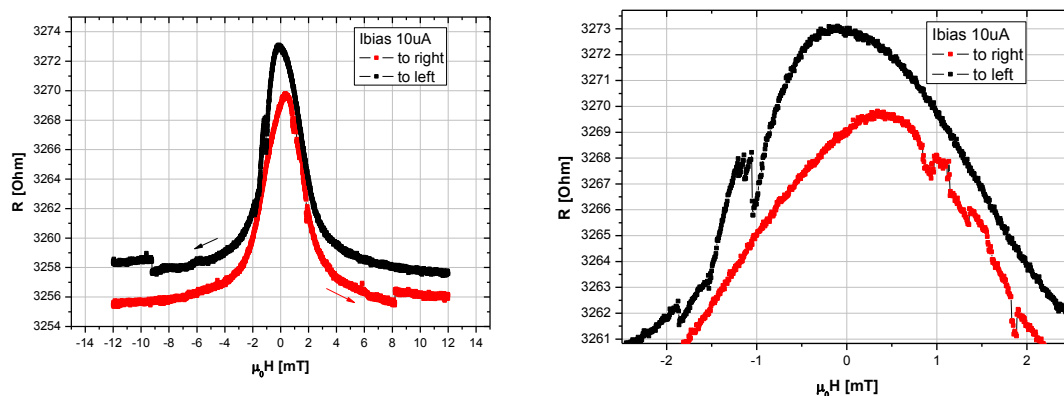


Fig. 4.2.10 a) MR measurements of 3 μm long and 500 nm wide nanowires with 2 100 nm wide constrictions (Py 20nm thin) at room temperature. $I_b=10 \mu\text{A}$ b) a particular around $H_a=0$.

When H_o is reduced from the negative saturation value (i.e. -12 mT, red curve), a series of negative jumps were detected at H_o close to +1mT.

The jumps in this region are probably due to the reorientation of \mathbf{M} inside the connection arms at the corners (see arrows in Fig. 4.2.9(a)): in fact, low activation magnetic fields values (i.e. 1-2 mT) are not compatible with steps expected in nanoconstrictions after the realized size reduction both in widths and thickness. Measurements performed both with the applied magnetic field parallel and perpendicular to the nanowire direction don't show significant differences, as a consequence of balanced contribution to AMR resulting both from parallel and perpendicular parts of the nanowire contacts with respect to applied field [129]. Results are summarized in Fig. 4.2.11 where the red and black curves are referred to magnetic field parallel and perpendicular direction with respect nanowires.

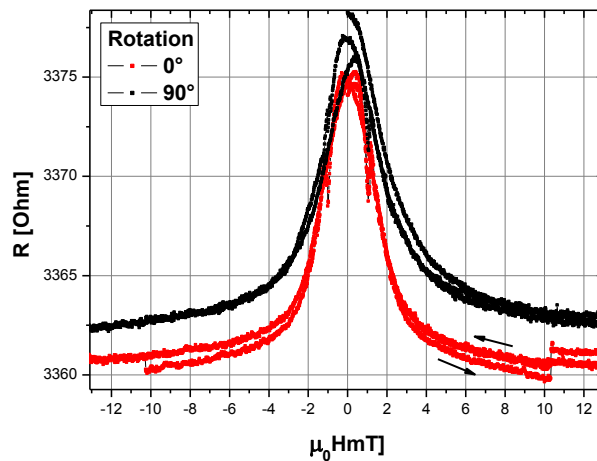


Fig. 4.2.11 Confront of MR of at different H_a direction.

When H_a is increased up to 10 mT, a pronounced positive jump is observed, and the corresponding MR ratio is 0.027%. This jump should correspond to the annihilation of a DW (or DWs) localized at the nanoconstrictions. We believe that the DW was nucleated during the sign crossover of the applied magnetic field H_a : \mathbf{M} persists in the opposite direction (with respect to H_a) due to a strong shape anisotropy, and only a slight rotation of \mathbf{M} takes place to form a small angle with I_b until $H_a = 10\text{mT}$ is achieved where \mathbf{M} realigns with the applied field. The measured MR positive jump resulted in a negative AMR effect within the domain constrained into the nanowire. Such a domain annihilated at $H_a=10\text{ mT}$, and consequently MR returned to a background parabolic behavior as in uniformly magnetized film (see Fig. 4.2.12). Unfortunately, we didn't fabricate a sample without nanoconstrictions with the same aforementioned geometry. Nevertheless, by comparing normalized MR measurements of Fig. 4.2.10(a) it appears that the background AMR behavior lies at larger values with respect the situation in the presence of DWs as shoed in Fig. 4.2.13.

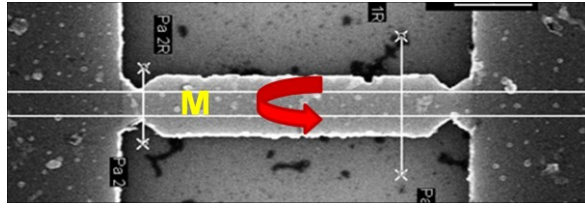


Fig. 4.2.12 Schematic of M realignment.

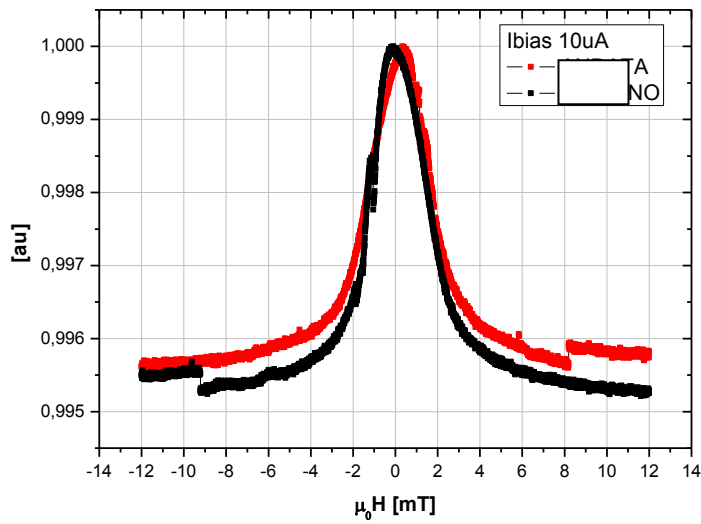


Fig. 4.2.13 Normalized MR measurements (RCN sample) of 3 μm long and 500 nm wide nanowires with 2 100 nm wide constrictions.

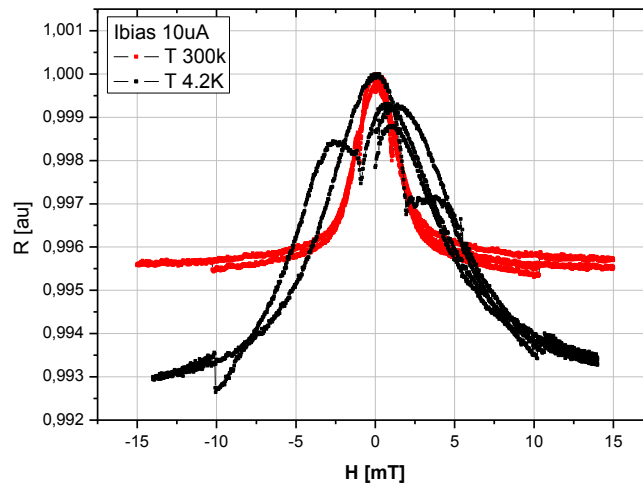


Fig. 4.2.14 Change in MR (RCN) at low temperature.

MR measurements have been performed also at low temperatures (down to $T=4.2$ K).

By looking at experimental results presented in Fig. 4.2.14, the “switching field” at $H_0=10$ mT still persists without an appreciable change, while the parabolic results changed. The MR ratio was found to be larger of about a factor 2. This result is not in agreement with similar results found in literature [130]. Fig. 4.2.15 shows the temperature dependence of DWs for a Py based zigzag wire.

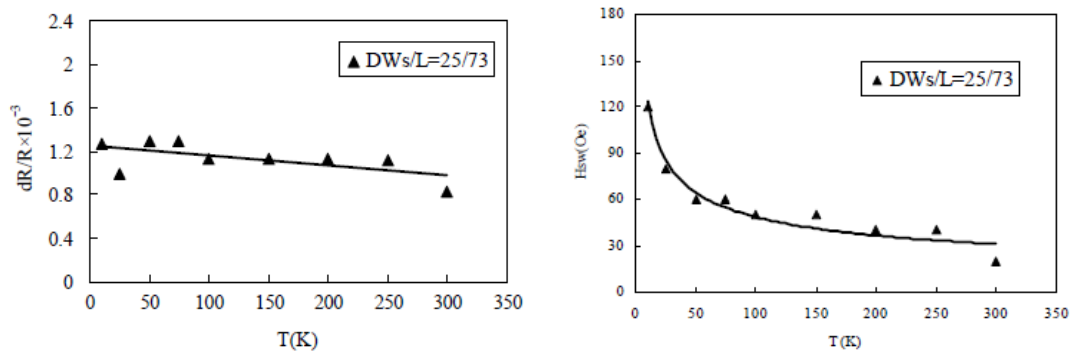


Fig . 4.2.15 Py based “zigzag” wire a)Temperature dependence of the normalized domain wall MR in the zigzag wire b) Temperature dependence of switching field. Taken from [130].

The DWs contribution to MR shouldn’t change in intensity but only in the switching field value: we expect that the lower the temperature the higher the field. We realized an innovative configuration consisting of arrays of smaller nanowires and nanoconstrictions as shown in Fig. 4.2.16(a) (Array of Parallel Nanowires). In particular, N parallel nanocontacts are connected by to Py 20nm islands-type rectangular $100 \times 200 \mu\text{m}^2$ thin films. Each nanocontact was realized by connecting a square $500 \times 500 \text{nm}^2$ Py island by two nanoconstrictions 70 nm wide. We fabricated and tested several samples, and in the following we present MR experiments on N=10, 5, 3, and 1 respectively. In Fig. 4.2.16(b) a SEM picture of a single nanoconstriction is shown.

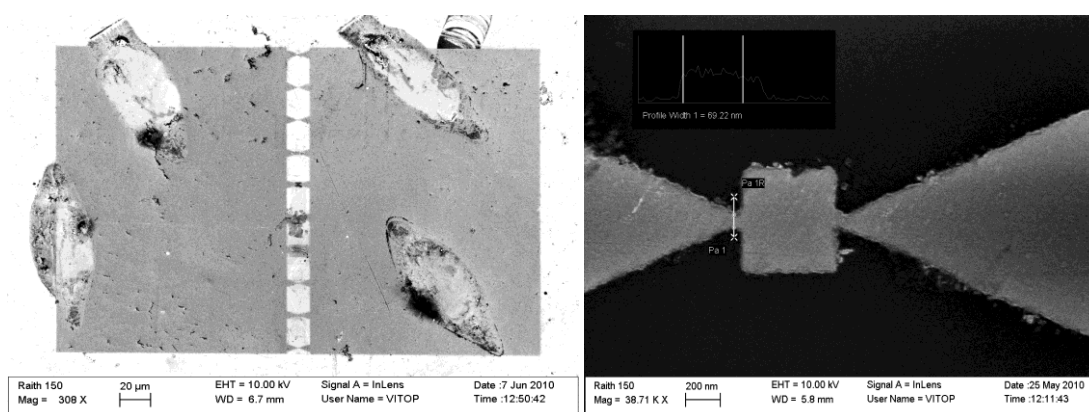


Fig. 4.2.16 SEM images of APN: a) sample configuration b) zoomed nanowire.

Fig. 4.2.17(a) shows the MR measurements for a N=10 APN sample at different angle between applied magnetic field H_0 and the bias current I_b .

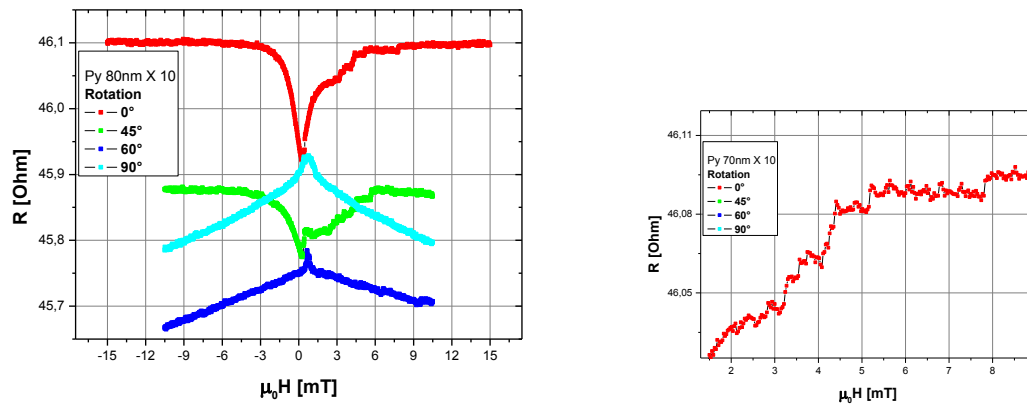


Fig. 4.2.17 a) Confront of MR of at different H_a direction for APN, $N=10$ at room temperature b) a zoomed particular at 0° .

The AMR effect due to the Py macro-pads seems to rule the MR response: in the case of a bias current parallel to the applied magnetic field (see red curve in Fig. 4.2.17(a)), starting from the negative saturation and at $H_a > 0$ a series of resistance jumps into the MR curve are clearly visible. The number of observed jumps is 10, i.e. the number of parallel connected nanowires, even if some of them don't appear in a clear way. The average MR ratio as calculated taking into account the well recognized steps is about 0.022%. Again, the physical mechanism beyond the observed behavior is to be related to the formation of DWs in the nanoconstrictions, and the rotation of \mathbf{M} when the threshold field is achieved for each nanocontact. The presence of different switching fields was probably due to small differences in realized patterns caused by the lithography process. In order to better evidence the rule of single connections we measured samples with $N=3$ and $N=1$ APN. In Fig. 4.2.18 the MR curve for $N=3$ nanowires is shown: the external magnetic field has been initially applied at large negative values and parallel to I_b .

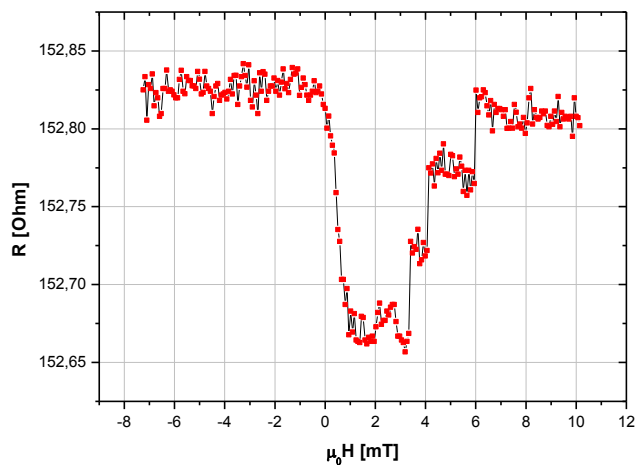


Fig. 4.2.18 MR measurements APN, $N=3$ at room temperature.

A number of steps now exactly equal to the N parallel connections is clearly observed, and a MR ratio of 0.030% has been measured. The situation is quite interesting for the case N=1 single nanowire as shown in Fig. 4.2.19. It's important to notice that realized devices showed highly reliable magneto-resistance steps.

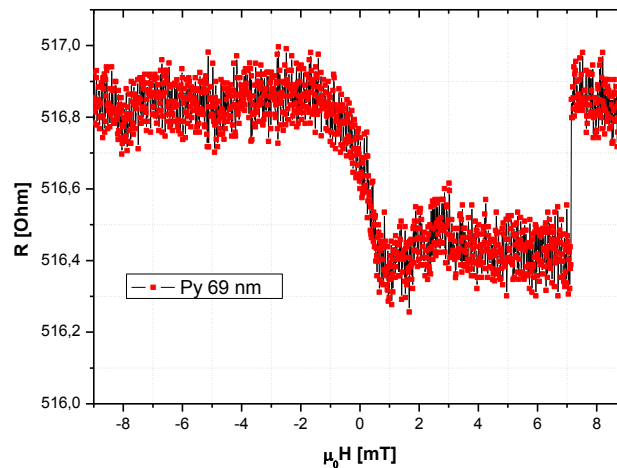


Fig. 4.2.19 MR measurements for a single nanowire at room temperature.

The negative drop in MR at $H_a \leq 0$ can be ascribed to the AMR effect which originated in the macro-contact according to Py behavior as in Fig. 4.2.4(a). The presence of trapped DWs located across the nanoconstriction produces a frozen MR at $H_a > 0$, and until $H_a = 7$ mT. At this value of the external applied field a clear switching is recorded, and the corresponding MR ratio is about 0.1 %. This result is in agreement with others in literature, for example see ref. [131,132], where the presence of DWs, trapped in nanoconstrictions, is also confirmed by MFM images. As a further confirmation about the nucleation of a DW in the N=1 nanostructure, the results in Fig. 4.2.20 show that the frozen DW state still persists after a new negative H_a biasing without crossing the threshold switching field at $H_a > 0$.

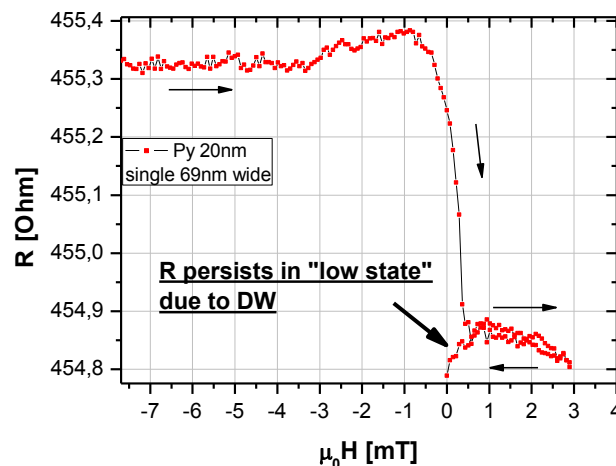


Fig. 4.2.20 MR measurements for a single nanowire at room temperature in a particular range.

The single nanowire configuration realized a sort of CIP spin-valve, and the external magnetic field controls the two state resistance. Moreover, the role of DW in the MR is still an open question and different models predict different DW behaviors [133,134]; anyway the DW thickness seems to be not thin enough to give a large MR effect.

Photo-response experiments on magnetic nanowires: preliminary results

The understanding of the effect of different scattering sources on DW resistivity, and the possibility of controlling the MR characteristics through an external source (e.g. optical radiation) have been the object of several studies in literature [see for example 135,136]. The approaches are quite different ranging from the spin dependent impurity description, as proposed by Levy et al. [137], as a source for mixing the spin channels, to the spin orbit interaction enhanced after the absorption: all the efforts have been devoted to explain the decreasing of relaxation rates of electrons in DW, and consequently the increase of the DW resistance. To what concerns the role of the effect of the Zeeman interaction on the magnitude and sign of the DW resistivity, the situation is still under debate, and both increasing and decreasing resistance of the DW can be predicted in the presence of an applied magnetic field [138,139]. The investigation of the adiabatic torque, which accounts for transport processes in which the conduction spin follows the local spatial magnetization variation by remaining in either the majority or minority state, has been well investigated by a number of different transport theories. In contrast, the non-adiabatic limit, which could be achieved in low dimension nanoconstrictions, remains the subject of much debate. In addition, the interaction of the DW with an external optical radiation has not been extensively investigated: it's reasonable to argue that the presence of a magnetic field from the absorbed incident photon and the width of the junction can contribute effectively to momentum transfer, spin mistracking or spin-flip scattering. It is predicted that large nonadiabatic effects should appear in narrow domain walls because of large magnetization gradients, whereby the wall width becomes comparable to important transport scales such as the spin-diffusion length, which is of the order of a few nanometres in ferromagnetic transition metals. The presence of a non-adiabatic term is of fundamental importance, because its existence implies that current-driven wall motion is possible for any finite current in a perfect system, even in the absence of an applied magnetic field. The use of lasers for manipulating and controlling the magnetization represented the basis of a new field in modern magnetism [140,141]. In particular, Bigot et al. have shown the existence of a coherent coupling between a femtosecond laser pulse and the magnetization of thin magnetic films (e.g. Ni). All the recent findings may provide new prospects for applications of ultrafast opto-magnetic phenomena in magnetic storage and information processing technology. Accordingly, the study of the effect of laser irradiation on novel magnetic systems can contribute to a better understanding and controlling of device performances. Recently, Majidi et al., proposed an investigation of the resistance of a nanojunction after the absorption of a polarized photon [142] using a semi-classical approach. The nanojunction has been described by a Néel type DW (see Fig. 4.2.21), between two ferromagnetic electrodes with opposite direction of magnetization. The DW is located within the ferromagnetic nanowire connecting the two electrodes.

The approach considers a photon which propagates along the nanowire axis (a sort of waveguide): such a situation doesn't corresponds to our standard experiments where the light is incident perpendicular to the sample plane, when the irradiation is realized by an optical fiber or a direct illumination. Nevertheless, the approach is among few we find in literature where the coupling of laser radiation with the ferromagnetic matter, and in particular the DW presence. The geometrical configuration in Ref. [142] is the one proposed in Fig. 4.2.21.

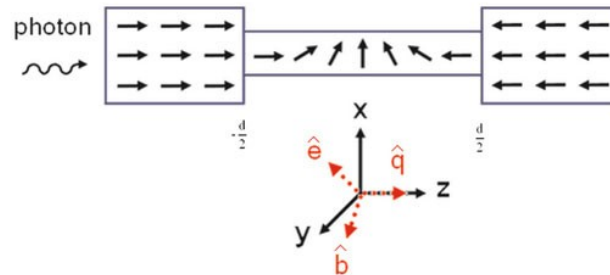


Fig. 4.2.21. A Neel-type DW between two ferromagnetic electrodes.

Although the used approach is independent on the direction of magnetization in the ferromagnetic regions, but only on functional form of the DW, regarding the shape anisotropy the magnetization of the system is considered to be along the wire axis. The magnetization is continuously rotated over the DW width, d , and it is transverse to the wire direction, z -axis, at the center of the wall. For this linear DW, the rotation angle can be described as $\vartheta(z) = (\pi/d)z + (\pi/2)$, which indicates the angle between the local direction of the magnetization and z -axis. Among the numerical results contained in Ref. [142], it is interesting recall the MR dependence as a function of the DW width as shown in Fig. 4.2.22 at different photon x-linearly polarized wavelengths: smaller the DW width larger the expected MR response at different photon energies.

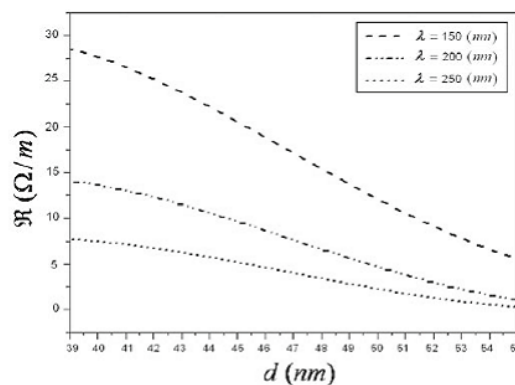


Fig. 4.2.22 the DW resistance per unit length vs. DW width for different values of x-linear polarized photon wavelengths.

Very preliminary photo-response experiments have been performed on a N=1 single nanowire at room temperature in the APN configuration as previously discussed. The experimental apparatus has been already described in Chapter 4.1. The incident average beam power was measured to be about 1 mW. The sample was mounted inside a cryostat but measurements were done at room temperature. The normalized MR curves as a function of the applied magnetic field without (red curve) and with (black curve) laser irradiation are showed in Fig. 4.2.23.

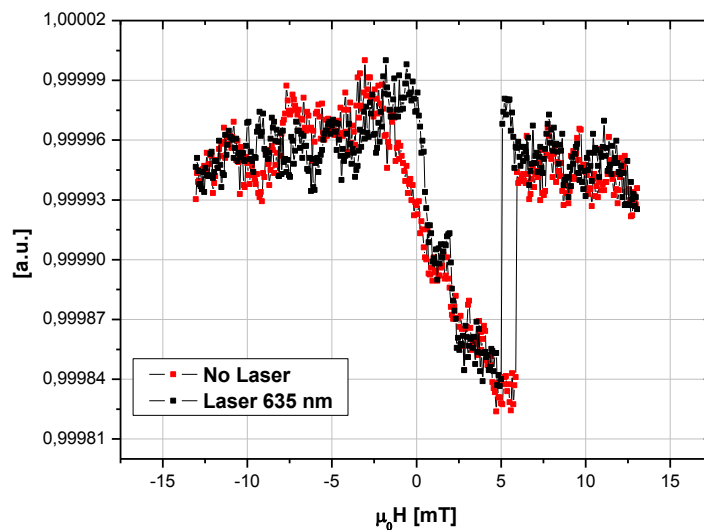


Fig. 4.2.23 Normalized MR vs applied magnetic field parallel to the nanowires without (red) and with (black) laser irradiation 1mW 800nm (T=300K).

In this experiment the laser beam is incident perpendicularly to the device plane, and hence the magnetic field is in the plane of the Neel type DW created inside the nanostructure, with components both parallel and perpendicular to the current flow inside the nanojunctions. We believe that the effect due to the magnetic field of the laser radiation is negligible, and covered by the dc field externally applied. Nevertheless, the heating effect arising from the irradiation can be effective inside the nanoconstriction regions. The MR curve shows two distinct features: the increase of the depinning DW magnetic field, and the decrease of the AMR contribution close to $H_0 \leq 0$. It is clear that an increase of the sample temperature can influence the DW motion, above all if the temperature is approaching the Curie temperature where the magnetization saturation is expected to be reduced. According to Ref. [143], the final temperature of the current heated nanowire for current-induced DW motion strongly depends on the substrate and thermal resistance which develops at the surroundings of the device. Nevertheless, our observation are not in complete agreement with a simple temperature increase of the device. In fact, the reduction of AMR contribution after the laser irradiation can be explained according to an increase of the thermal fluctuations which destroy the magnetic order generated by the external field [144]. However, the increase in temperature as expected by the laser irradiation, produces an increase in the DW pinning field of about 1 mT. Such a result is in agreement with experimental results in Ref. [145] where authors demonstrated the

preference of DW to remain at the laser spot with interesting potentials in terms application as a flexible way of controlling DWs.

Unfortunately, we didn't complete all experiments as requested by this interesting phenomenology within the PhD thesis deadline. Further measurements are under developing, which will clarify better the non-equilibrium physical situation when laser radiation and DW limited conduction take place simultaneously.

References

- [109] A. D. Semenov, G. N. Gol'tsman, and R. Sobolewski, *Supercond. Sci. Technol.* **15**, R1 (2002), and references therein.
- [110] H. Shibata, T. Maruyama, T. Akazaki, H. Takesue, T. Honjo, and Y. Tokura, *Physica C* **468**, 1992 (2008).
- [111] A. Verevkin, J. Zhang, R. Sobolewski, A. Lipatov, O. Okunev, G. Chulkova, A. Korneev, K. Smirnov, G. N. Gol'tsman, and A. Semenov, *Appl. Phys. Lett.* **80**, 4687 (2002).
- [112] R. Sobolewski, A. Verevkin, G. N. Gol'tsman, A. Lipatov, and K. Wilsher, *IEEE Trans. Appl. Supercond.* **13**, 1151_2003_.
- [113] A. I. Buzdin, *Rev. Mod. Phys.* **77**, 935 (2005), and references therein.
- [114] D. Pan, G. P. Pepe, V. Pagliarulo, C. De Lisio, L. Parlato, M. Khafizov, I. Komissarov, and R. Sobolewski, *Phys. Rev. B* **78**, 174503 (2008).
- [115] M. Erjanec et al. *Supercond. Sci. Technol.* **22** (2009) 055006
- [116] H. Myoren, Y. Mada, Y. Matsui, T. Taino, and S. Takada, *J. Phys.: Conf. Ser.* **97**, 012329 (2008).
- [117] H. Liu, Z. Ye, W. Wu, and K. D. D. Rathnayaka, *J. Appl. Phys.* **105**, 07E305 (2009).
- [118] K. Il'in, M. Siegel, A. Engel, H. Bartolf, A. Schilling, A. Semenov, and H.-W. Huebers, *J. Low Temp. Phys.* **151**, 585 (2008).
- [119] A. Engel, H. Bartolf, A. Schilling, K. Il'in, M. Siegel, A. Semenov, and H.-W. Huebers, *J. Phys.: Conf. Ser.* **97**, 012152 (2008).
- [120] T. Taneda, G. P. Pepe, L. Parlato, A. A. Golubov, and R. Sobolewski, *Phys. Rev. B* **75**, 174507 (2007).
- [121] A. Buzdin and D. Feinberg, *Physica C* **256**, 303 (1996).
- [122] H. Bartolf, A. Engel, A. Schilling, K. Il'in, M. Siegel, H.-W. Hübers, and A. Semenov, *Phys. Rev. B* **81**, 024502 (2010).

- [123] A.Verevkin,A.Pearlman,...,N.Gol'tsman and R.Sobolewski,Ultrafast superconducting single-photon detectors for near-infrared-wavelength quantum communications, *J.Modern Optics*, vol.**51**,pp.1447-1458, (2004)
- [124] G.N.Gol'tsman,A.Korneev,...,A.Verevkin and R.Sobolewski, *Physica Status Solidi C, Conf.*, vol. **2**, no.5, pp. 1480-1488, (2005)
- [125] F. A. Hegmann and J. S. Preston, *Phys. Rev. B* **48**, 16023 (1993).
- [126] D. A. Allwood, *et al.* *Magnetic Domain-Wall Logic Science* **309**, 1688 (2005);
- [127] M. Hayashi et al. *Science* Vol. 320 no. 5873 pp. 209-211 (2008)
- [128] S.D. Bader and S.S.P. Parkin *Spintronics Annu. Rev. Condens. Matter Phys.* (2010).
- [129] T. Taniyama et al. *Resistivity due to Domain Walls in Co Zigzag Wires* 82,13 *Phys. Rev. Lett.* (1999)
- [130] J.L. Tsai et al. *Journal of Magnetism and Magnetic Materials* 239 (2002) 246–248
- [131] M. Tsoi et al. *Appl. Phys. Lett.* 83, 13 (2003)
- [132] H. T. Zeng et al. *Appl. Phys. Lett.* 94, 103113 (2009)
- [133] G. Tarata et al. *Phys. Rev. Lett.* 78,3773 (1997)
- [134] J. Velez and W. H. Butler *Phys. Rev. B* 69, 094425 (2004)
- [135] G.S.D. Beach, M. Tsoi, J.L. Erskine, *J. Magn. Magn. Mater.* **320**, 1272 (2008)
- [136] S.S.P. Parkin, M. Hayashi, L. Tomas, *Science* **320**, 190 (2008)
- [137] 15. P.M. Levy, S. Zhang, *Phys. Rev. Lett.* **79**, 5110 (1997)
- [138] A. Phirouznia, M.M. Tehranchi, M. Ghanaatshoar, *Eur.Phys. J. B* **54**, 103 (2006)
- [139] J.D. Burton, A. Kashyap, M.Y. Zhuravlev, R. Skomski, E.Y. Tsymbal, S.S. Jaswal, O.N. Mryasov, R.W. Chantrell, *Appl. Phys. Lett.* **85**, 251 (2004)
- [140] A.V. Kimel, A. Kirilyuk, T. Rasing, *Laser Photon. Rev.***1**, 275 (2007);
- [141] J-Y. Bigot, M. Vomir, E. Beaurepaire, *Nat. Phys.* **5**, 515 (2009)
- [142] R. Majidi, M.M. Tehranchi, A. Phirouznia, and K. Ghafoori Tabrizi, *Eur. Phys. J. B* **76**, 475–480 (2010)
- [143] C-Y You and S-S Ha, *APL* 91,022507 (2007)
- [144]G. Vertesy et al., *J. Appl. Phys.* 93, 4040 (2003)
- [145] J.H. Franken et al., *Appl. Phys. Lett.* 95, 212502 (2009)

Conclusions

In this thesis novel, high-end superconducting and spintronic devices have been fabricated and characterized. In summary, the proposed work has been focused on the realization of nanowires, and more generally nanostructures, using the Electron Beam Lithography. Such a technology offers a powerful solution for nanofabrication able to conjugate spatial resolution, operation flexibility, and costs.

Two main research fields has been explored: superconductive nanowires for advanced optical detection and nanostructures for magneto-resistance based devices.

In the first, i.e. superconductive nanowires, thin film bilayers formed by a superconductor (i.e. NbN) in close contact with a weak ferromagnetic overlayer (i.e. NiCu), have been deposited and characterized down to low temperatures. The nanowires have been patterned by EBL in novel meander-like configurations which combine series and parallel connections: in particular, six blocks of three parallel nanowires (widths <500nm, length 20 μ m, thickness 8nm) connected in series. The choice of this complex geometry has been suggested by the possibility to have large detection area, intrinsic amplification mechanisms of the photo-response voltage signal, and a inner control of the device inductance. The characterization of fabricated devices has been performed in terms of transport and photo-response properties down to low temperatures (i.e. 4.2 K). NbN-based proximitized nanowires showed an enhancement of the critical currents up to a factor 6, and a consequent amplification of the pulse amplitude of the photoresponse signals in the presence of laser pulses (10 ns 1550 nm laser diode pulses) with respect the pure NbN. All these features have been explained in terms of increased pinning centers density inside the S layer after the interdiffusion of N-atoms/clusters at the interface: this effect results in larger pinning forces on vortices, and hence higher critical currents, which reflects on larger kinetic inductance based photoresponse signals. The analysis of the resistance $R(T)$ vs. temperature T curves of nanowires supports the hypothesis of an increase of vortex lattice polarizability in such proximitized structures up to a factor 10 with respect to sole NbN as measured with the same geometry.

Some interesting perspectives can be:

- measurements of transport properties in the presence of large perpendicular magnetic fields;
- Improvement of single-photon experiments and quantum efficiency measurements;
- Investigation about the role of vortices in terms of signal mechanism generation and dark counts effects;

The nanotechnology in the magnetic research field has been applied to the study of the magnetoresistance in Permalloy nano-constrictions patterned by EBL. Planar spin-valve devices were structured in order to investigate the effect of a constrained DW, pinned at the nano-constrictions, on MR measurements. Three different configurations have been realized and tested by applying an external magnetic field at different intensities and directions. In the first, contact lines are “in-line” (ILN) with the nanowire axis, in the second the contact lines form a 90°

angle with the nanowire axis (RCN), while in the third parallel nanowires (N=10,3,1) (APN) (without connection arms) have been tested. In particular, the characterization was focused to optimize the geometrical configuration to isolate/optimize the DW contribution on the overall measured MR. In the N=1 APN configuration we realized a sort of planar spin-valve, where the external magnetic field controls a two-state resistance.

Some interesting perspectives can be:

- measurements of MR in the presence of larger bias currents for studying the possibility to control the displacement of DWs pinned at the nanoconstrictions;
- reduced nanopatterning for fabricating smaller nanoconstrictions, obtaining smaller nanocontacts and nonadiabatic regime in spin torque experiments;
- to have thinner DWs.
- Nonequilibrium experiments on DW motion in controlled nanoconstrictions after irradiation by fast laser pulses.

As a future planning of this research activity we'd like to mention the possibility of combining superconducting nanowire photon detectors to magnetic nanowires directly coupled to them. One possibility is to use hybrid nanostructures made by superconductor/ferromagnet very thin films (<10nm) and patterned in the APN configuration. The idea is to use the F layer for generating a DW localized in the nano-constrictions, and then detect the effects on MR through the modification of the non-equilibrium distribution function in the S nanowire (e.g. kinetic inductance) due to the inverse proximity effect. Such a configuration should potentially offer the possibility to have a high efficiency detection which is also in principle sensitive to photon polarization.

Publications:

Part of this thesis has been published:

N. Marrocco, G. P. Pepe, A. Capretti, L. Parlato, V. Pagliarulo, G. Peluso, A. Barone, R. Cristiano, M. Ejrnaes, A. Casaburi, N. Kashiwazaki, T. Taino, H. Myoren, and Roman Sobolewski, ***Strong critical current density enhancement in NiCu/NbN superconducting nanostripes for optical detection*** Appl. Phys. Lett 97, 092504 (2010)

Others publications during this three are listed:

D. Pan, G.P. Pepe, V. Pagliarulo, C. De Lisio, L. Parlato, M. Khafizov, I. Komissarov and R. Sobolewski, ***Layered ferromagnet/superconductor heterostructures: Nonequilibrium quasiparticle dynamics and photodetector applications***, Phys. Rev. B 78, 174503 (2008)

A. Peluso, V. Pagliarulo, G. Carotenuto, G. P. Pepe, D. Davino, C. Visone, A. Longo, and F. Capezzuto ***SYNTHESIS AND CHARACTERIZATION OF POLYMER EMBEDDED IRON OXIDE NANOCOMPOSITES*** MICROWAVE AND OPTICAL TECHNOLOGY LETTERS / Vol. 51, No. 11, November 2009

G.P. Pepe, L. Parlato, N. Marrocco, V. Pagliarulo, G. Peluso, A. Barone, F. Tafuri, U. Scotti di Uccio, F. Miletto, M. Radovic a, D. Pan, Roman Sobolewski ***Novel superconducting proximized heterostructures for ultrafast photodetection*** Cryogenics Vol. 49, 11 660-664 (2009)

G. Pepe, D. Pan, V. Pagliarulo, L. Parlato, N. Marrocco, C. De Lisio, G. Peluso, A. Barone, U. Scotti di Uccio, A. Casaburi, F. Tafuri, M. Khafizov, T. Taneda, and Roman Sobolewski ***Ultrafast Photoresponse of Superconductor/Ferromagnet Nano-Layered Hybrids*** IEEE TRANS. ON APPLIED SUPERCONDUCTIVITY, VOL. 19, NO. 3, JUNE 2009

R. Scaldaferrri, G. Salzillo, G.P. Pepe, M. Barra, A. Cassinese, V. Pagliarulo, A. Borriello and L. Fusco ***Influence of fillers concentration on electrical properties of polystyrene matrix doped by gold nanoparticles and 8HQ*** Eur. Phys. J. B (2009)

V. Iannotti, S. Amoruso, G. Ausanio, C. Campana, E. Esposito, C. Hison, V. Pagliarulo, G. Pepe, L. Lanotte ***Magnetic, Elastomagnetic and Elastoresistive Behaviour of Nanoparticles-Assembled Films Produced by fs-PLD*** FNMA'10 Magnetic (proceeding ISBN 978-83-930549-1-6)